



Universidad de Navarra

Facultad de Ciencias

**CHARACTERIZATION OF THERMOCONVECTIVE INSTABILITIES
IN SPATIALLY EXTENDED SYSTEMS**

Montserrat Ana Miranda Galcerán



Universidad de Navarra
School of Science

CHARACTERIZATION OF THERMOCONVECTIVE INSTABILITIES IN SPATIALLY EXTENDED SYSTEMS

Submitted by **Montserrat Ana Miranda Galcerán** in partial fulfillment of the requirements for the Doctoral Degree of the University of Navarra

This dissertation has been written under my supervision at the Department of Physics and Applied Mathematics, and I approve its submission to the Defense Committee.

Signed on June 16, 2009

Dr. Javier Burguete Mas

Declaración:

Por la presente yo, **Da. Montserrat Ana Miranda Galcerán**, declaro que esta tesis es fruto de mi propio trabajo y que en mi conocimiento, no contiene ni material previamente publicado o escrito por otra persona, ni material que sustancialmente haya formado parte de los requerimientos para obtener cualquier otro título en cualquier centro de educación superior, excepto en los lugares del texto en los que se ha hecho referencia explícita a la fuente de la información.

(I hereby declare that this submission is my own work and that, to the best of my knowledge and belief, it contains no material previously published or written by another person nor material which to a substantial extent has been accepted for the award of any other degree of the university or other institute of higher learning, except where due acknowledgment has been made in the text.)

De igual manera, autorizo al Departamento de Física y Matemática Aplicada de la Universidad de Navarra, la distribución de esta tesis y, si procede, de la "fe de erratas" correspondiente por cualquier medio, sin perjuicio de los derechos de propiedad intelectual que me corresponden.

Signed on June 16, 2009

Montserrat Ana Miranda Galcerán

ISBN 978-84-692-4266-7

© Montserrat Ana Miranda Galcerán

Derechos de edición, divulgación y publicación:

© Departamento de Física y Matemática Aplicada, Universidad de Navarra

To Wens, Joel and Robert

Acknowledgements

I am indebted to my thesis advisor, Dr. Javier Burguete, for his generous advise, great confidence and infinite patience. Delivering ideas with my thesis advisor about experimental results and the nature of our system has been a constant challenge for me. I am respectfully thankful to researchers from whom I learnt key paths when my research was confusing: Pierre Collet, Lionel Gil, Héctor Mancini, Wenceslao González-Viñas and Roland Ribotta.

I am thankful to the welcome of the group of condensed matter physics during my stage in the research center of CEA, Saclay (France), particularly to Arnaud Chiffaudel, François Daviaud and Nicolas Garnier.

I am happy to have shared good moments with my research fellows at the department: Roberto Arévalo, Iván Martínez-Forero, Maximiliano Giuliani, Diana González, Tomás González, Álvaro Janda, Cristian Mankoc, Martín Pastor, Moorthi Pichumani, Alberto de la Torre and Gerard Vidal.

I am particularly thankful to the professors of the Department of Physics and Applied Mathematics, for their humanity: Sergio Ardanza, Javier Burguete, María Jesús Chasco, Jorge Elorza, Angel Garcimartín, Wenceslao González-Viñas, Héctor Mancini, Diego Maza, Carmen Palacios, Antonio Pelaez, Iker Zuriguel. Specially thanks to professor Jean Bragard for borrowing and keeping books he had specially ordered to the library. To other members of the department Pedro Elizalde and Pilar Ayúcar.

To the University of Navarra and the School of Science for their support at every stage of my research.

To the “Asociación de Amigos de la Universidad de Navarra” for their economical support. Also to projects from MEC: HF20001-008, BFM2002-02011, FIS2007-66004-C02-01, FIS2008-01126 and from PIUNA.

Thanks a lot to Wens, Joel and Robert for sharing with me enthusiasm and adventure, you deserve a prize: “Choose a star, the one you like most, it’s for you”.

Any irregularity or unevenness in the product is not always a manufacturing defect but an assurance that this is a genuine hand made product. It creates a beauty unmatched by any mass produced material.

Craft Resource Center *Calcutta (2009)*

I am an old man now, and when I die and go to Heaven there are two matters on which I hope for enlightenment. One is quantum electrodynamics and the other is turbulent motion in fluids. And about the former I am really rather optimistic.

Sir Horace Lamb, *At a meeting of the British Association in London (1932)*

Contents

Preface	XIII
Glossary	XVII
1. Introduction	1
1.1. Symmetry breaking instabilities	2
1.2. Nonlinear dynamics and instabilities	3
1.2.1. Absolute and convective instabilities	4
1.2.2. First and second order instabilities	5
1.2.3. Fronts in bistable regimes	6
1.3. An open fluid layer under free convection	8
1.3.1. Bénard-Marangoni convection	11
1.3.2. Instability mechanisms of hydrothermal waves	11
1.4. Similar dynamics in other experimental systems	13
1.5. Phase synchronization phenomena	14
1.5.1. Weak coupling in an ensemble of synchronized oscillators	16
2. Laboratory techniques and signal processing in the 1D-cell experiment	19
2.1. The rectangular cell	19
2.2. The fluid	21
2.3. The thermal field	22
2.3.1. The control parameters	23
2.4. Shadowgraphy technique	24
2.4.1. The calibration process	26
2.5. Data analysis I: A global view of the convective field	26
2.5.1. Bidimensional complex demodulation technique	27
2.5.2. A practical application to a pattern without fronts	30
2.5.3. Extracting subcritical parameters from bistable patterns	30
2.5.4. A practical application to a pattern with fronts	31
2.6. Data analysis II: A network of convective coupled oscillators	33
2.6.1. Tracking the oscillators trajectories	33
3. Characterization of instabilities in an extended 1D convective system	39
3.1. Introduction	40
3.2. An extended 1D convective system	40

3.3.	The Fourier spectra of asymptotic patterns	42
3.4.	Dynamics of the convective cells: breaking the symmetries	43
3.5.	The stability diagram	45
3.6.	Dynamics in intermediate layers: Subcritical bifurcation to traveling waves and further	47
3.7.	Dynamics in shallow layers: Overview of a clustering process	51
3.7.1.	Irregular clusters in the mixed pattern	53
3.7.2.	Supercritical bifurcation to stationary clusters	57
3.8.	Bistability and 1D-fronts	60
3.8.1.	Transient regimes in bistable systems	62
3.9.	Discussion and conclusions	66
4.	Spatiotemporal phase synchronization from nonlocal coupling	71
4.1.	Focus on phase synchronization in the spatiotemporal beating regime	72
4.1.1.	Antiphase cross-correlation matrix	73
4.2.	A global bifurcation	78
4.3.	A discrete order parameter	82
4.4.	Topology from the rewiring connections	83
4.4.1.	Modelling a time-varying topology	87
4.5.	Discussion and conclusions	87
5.	Thermocapillary instabilities in a cylindrical cell	89
5.1.	Introduction	90
5.1.1.	Hydrothermal waves in a cylindrical cell	90
5.2.	Experimental setup	91
5.2.1.	The fluid	93
5.3.	Experimental techniques and data analysis	94
5.4.	The stability diagram	94
5.4.1.	Secondary instability to the ALT pattern	102
5.5.	Discussion and conclusions	105
	Conclusions and Outlook	107
	Bibliography	113
	Summary	123
	Resumen	124

Preface

Many systems in nature are **spatially extended**, this means that any structure or *pattern* that emerges inside them is characterized by finite spatial scales much smaller than the system size. The time evolution or *dynamics* of these systems may also sustain finite temporal scales or frequencies. Some systems exhibit spatiotemporal modulated patterns or *lattice patterns* which fit a wave description in terms of an amplitude and a phase that involves the wave number and frequency. Lattice patterns surround our daily lives: ripples over the sand, waves over the oceans, morphogenesis of flowers [see Fig. 1(a)] and shells, crystal growth of snow flakes. In order to understand the genesis of patterns physicists stand close to the onset of the *instability* which gives rise to a new stable pattern. Depending on the microscopic physics, most patterns break some symmetries of the system at the onset of an instability, as Curie [1] observed long time ago. These are called **symmetry breaking instabilities**.

Before going onward, we will fix ideas looking at the sky. During the day, we easily encounter beautiful modulated high clouds in the sky [see Fig. 1(b)] which are not influenced by any boundary. These modulated clouds appear from a Kelvin-Helmholtz instability which is developed between shearing horizontal layers. During a clear night, our eyes reach the far-away bright stars which are born in the infinite firmament. The genesis of a star comes from the magnetorotational instability which pulls inward the outer-rotating galactic dust (Keplerian disc) under magnetic fields. These are extended and complex systems which are also dissipative because they spend energy at the expense of an increase of the entropy in the universe.

The aforementioned examples involve a high degree of complexity, thus many independent dynamical variables are involved. These systems are defined as *complex* and can give rise either to perfectly ordered patterns or to highly disordered ones. Disorder, or **spatiotemporal chaos** in the broad sense, is characterized by uncorrelated spatiotemporal scales like in turbulent patterns around a waterfall. Sometimes, complex and extended systems exhibit fronts which connect two different coherent patterns, these fronts may drift in time or remain stationary; fronts are always present in growth phenomena.

The purpose of the present thesis is to understand pattern-forming phenomena in spatially extended systems from a basic stable pattern, which might be a homogeneous pattern or a cellular lattice (stationary cells). To attain this objective, we will analyze different experimental convective setups. The systems are driven out of thermal equilibrium successively towards weak turbulent regimes. If we control the temperature applied to the system with enough accuracy, we are able to stop close to each new instability the system goes through in order to discover its nature.

Our experiment like any natural (real) system is not thermally isolated, consequently there is



(a)



(b)

Figure 1: In nature: (a) a magnolia flower chose a sort of thermo-hydrodynamical instability in cylindrical geometry (courtesy of Taliesin Smith); (b) coherent patterns in the sky are sometimes the result of shear instabilities;

a continuous heat interchange with its surrounding until the unachievable thermal equilibrium. The system is said to be constantly “out-of-equilibrium” and it is known as a *dissipative system*. Natural phenomena are dissipative and thus, the entropy irreversibly increases ¹. In this way, it is very difficult to think of a confined system which is able to sustain fronts after an infinite time.

Dissipative phenomena are very well represented in a physicists’ laboratory in the form of thermoconvective systems, for example a fluid layer subjected to a temperature difference. The first research on pattern-formation, which appeared in a thermoconvective experiment, was developed in 1900 by Bénard [2], who studied the instability mechanisms of the so-called **Bénard-Marangoni convection**. A stable pattern of hexagons emerges in an open fluid layer, which is contained in a cylindrical cell, when it is heated from below. Since then, convective instabilities in confined and extended systems have produced many interesting results on pattern-formation. However, only a few number of experiments have been focussed on the characterization of the nature of convective instabilities. In 1986, Pomeau [3] stressed the importance of performing new 1D experimental work with the aim of developing new concepts and ideas in those **bistable systems** where fronts are present between two different coherent patterns (or phases). Bistable systems undergo the classical [4] **subcritical instability** where *phase locking phenomena* spontaneously appear.

Our experiment is a spatially extended fluid layer (opened to the atmosphere), which is contained in a rectangular cell, under a localized and central heating along the largest direction. The major effort is focussed on understanding subcritical instabilities from a basic cellular pattern. It is a 1D-array of 75-coupled convective oscillators which may become entrained because of nonlinear coupling (interactions). **Entrainment or synchronization** of a sub-ensemble of oscillators give rise to the formation of **clusters** of synchronized oscillators. In 1967 phase synchronization phenomena were smartly introduced by Winfree [5] inspired on many different kinds of physiological rhythms which “reflect mutual synchronization of myriads of individual oscillatory

¹Onsager was awarded the Nobel prize in 1968, and Prigogine in 1977 for the foundation of thermodynamics of irreversible processes.

processes”.

Complex systems where each independent dynamical variable is taken as an oscillatory unit are found in every branch of science: in physics we study arrays of semiconductor lasers or superconductor arrays of Josephson junctions, in chemistry the Belousov-Zhabotinsky reaction, in biology the growth of bacteria colonies, in neurobiology the growth of multicellular tissues and the beating of cardiomyocytes, in neurology the synchronization of neurons in clustering processes and in ecology the formation, behavior and migration of communities of individuals.

One of the novelties of the present work is the change of view from the classical study of a **global convective system** to a new conception of patterns which appear as permanent states originated from synchronization processes of a **discrete convective system**. We consider an individual convective cell which belongs to the “stationary state” (cellular pattern) to be a potential oscillator at rest. But as we increase the temperature injected to these oscillators, a nonlinear weak coupling between oscillators is revealed. At this precise time, convective cells might be entrained to oscillate chaotically, or to convert into *self-sustained oscillators* (the kind of a van der Pol oscillator), which are also called *limit-cycle oscillators*. Our research is mainly focussed on two different phase synchronization phenomena: (i) from stationary units to irregular clusters of limit-cycle oscillators (from stationary cellular pattern to spatiotemporal chaos); and (ii) from limit-cycle oscillators defined by one frequency to limit-cycle oscillators defined by two similar frequencies (frequency splitting). We show that in weak turbulent regimes, this last condition is the necessary one to develop the cluster phase with larger temporal scales.

We ought to emphasize that clusters in our system are not only time dependent, they are also coherent patterns in space. This coherence breaks out from an original spatiotemporal chaotic regime because of a spatial and a temporal frequency splitting that we show from the analysis of the global convective system. This kind of coherent patterns has been theoretically approached in 1989 by Hohenberg and Shraiman [6] using a phase equation (generalized Kuramoto-Sivashinsky equation). There is still a lot of research to be done, experimentally and theoretically, aiming at the understanding of coherent phenomena in natural systems. There are recent efforts behind this purpose in the field of *complex networks* using numerical simulations [7–9].

We hope to contribute to fundamental physics: (i) trying to understand subcritical instabilities towards weak turbulence in extended systems (a 1D-array of 75-convective oscillators); (ii) developing new signal processing methods from two points of view: (ii.a) the study of amplitudes from a “continuous signal”; and (ii.b) the study of phases from a “discretized signal”. Besides, we encounter pattern-forming universality when we explore the dynamics of a convective layer in a cylindrical cell imposing a radial temperature gradient between an inner core and the outer wall.

Because similarity and symmetry breaking transitions afford the opportunity to derive universal laws, according to our work, an interesting application in the laboratory could be to characterize the magnetorotational instability in a metal fluid. Thus, this thesis (characterization of instabilities without external fields in the frame of nonlinear hydrodynamics) might be the starting point to study, for example, how an external helicoidal magnetic field is able to inhibit classical hydrodynamic instabilities of the oscillatory type. The analytic tools developed to understand spatiotemporal phase synchronization might be applied into other complex, extended and dissipative systems in chemistry, biology and neurology.

This work is structured according to the following: in Chapter 1 (the introduction) we give a general overview on nonlinear phenomena and instabilities, we present the basic hydrodynamical

equations for a fluid layer under convection and we deal with phase synchronization phenomena. Chapter 2 covers the experimental setup of the 1D-cell and the developed analytical methods on amplitudes and phases. Chapter 3 focuses on the 1D-cell, it shows general results over the whole stability diagram and particularly over clustering processes in shallow waters, bistability and fronts (published in Ref. [10, 11]). Chapter 4 is devoted to the study of synchronization transitions in the 1D-system using a phase mismatch model applied to each oscillator from the definition of an antiphase matrix, we also deal with topological properties (Ref. [12]). Chapter 5 presents experimental results on a 2D-thermoconvective system with cylindrical geometry where high depths have been explored, particularly, we have characterized instabilities when the central plot is heated; traveling waves, hydrothermal waves and flower-like patterns are found. Finally, in Chapter 6 we expose the conclusions and future perspectives of this work.

Glossary

Glossary of abbreviations and symbols	
HL	Heating line
BM	Bénard-Marangoni
RB	Rayleigh-Bénard
ΔT_v	Vertical temperature difference
ΔT_h	Horizontal temperature difference
ΔT_r	Radial temperature difference
1D-FFT	1D-Fast Fourier Transform
2D-FFT	2D-Fast Fourier Transform
L_x	Heater length
L_y	1D-cell width
T_h	Temperature at the heater
T_c	Temperature at the refrigerating walls
T_r	Room temperature
HW	Hydrothermal waves
HWW	Hydrothermal wake-waves
PC	Primary convection (homogeneous flow)
ST	Stationary waves (cellular pattern)
TW	Traveling waves
ALT	Alternating waves
ST/ALT	Mixed pattern
STC	Spatiotemporal chaos
ST/ZZ	Spatiotemporal beating regime (zig-zag pattern)
ST/DW	Temporal beating regime
CR	Corrotational rolls
BF	Basic Flow (homogeneous flow)
FL	Flower-like pattern
L_c	Coherence length (subcritical length)
ξ	Correlation length (attenuation length)
C_{ij}	Phase cross-correlation vector
\mathcal{A}_{ij}	Antiphase matrix
$Z(\omega)$	Order parameter in a phase synchronization transition
$L_{ij}(t)$	Link matrix
KM	Kuramoto model
CI	Couillet and Ioss theory
$\langle A, B \rangle$	Cross-correlation function
$\langle A, A \rangle$	Self-correlation function
$\langle A \rangle$	Average value
A^*	Complex conjugate matrix
A^\dagger	Transposed matrix

Chapter 1

Introduction

In the present work we try to characterize the instabilities developed in two different thermoconvective systems which consist of a fluid layer confined: (i) in a rectangular cell under a quasi-1D heating; and (ii) in a cylindrical cell, with an inner core, under lateral heating. Instabilities are recognized by an observable change in the dynamics displayed at the asymptotic regimes (we wait for the system to achieve a “stable” spatiotemporal pattern for long times). This change is also defined as a **bifurcation**. These systems are driven through the threshold of an instability by changing well-regulated parameters which are termed **control parameters**. The nature of a particular transition can be described choosing the proper magnitudes that allow us to quantify this change; these magnitudes are termed **order parameters**. Varying one control parameter at a time by finite steps, we explore the *phase space* or **stability diagram** where each type of asymptotic regime (or *phase*) defines a region. Instabilities between two regimes usually break some symmetries of the system imposing new spatial or temporal periodicities. These new symmetries perform a new pattern. In particular, our systems exhibit **lattice patterns** which might be defined as those yielding discrete symmetries. Lattice patterns observed in our systems have many features in common with patterns that appear in other different experimental and natural systems.

Main results are devoted to the quasi-1D thermoconvective system which, under certain constraints (concerning the depth of the fluid layer), consists of an array of nonlinear coupled convective oscillators which at the lowest energy stage corresponds to a stationary periodic 1D-pattern. These oscillators are ascending convective flows (hotspots) that exhibit a different spatiotemporal dynamics depending on the control parameters. As we increase the temperature, the system goes through a cascade of bifurcations towards weak turbulent regimes. In bistable regimes two different patterns (oscillatory or stationary) may coexist connected by 1D-fronts. Oscillatory domains correspond to sub-ensembles of *phase synchronized* oscillators which are defined as clusters of synchronization. These 1D-patterns are characterized by the presence of stationary and irregular clusters exhibiting different oscillatory dynamics. As we inject more energy (increasing temperature) the system undergoes a clustering process. These clustering processes are enclosed in the field of extended, dissipative and complex systems involving many degrees of freedom. The number of degrees of freedom corresponds to the number of intensive parameters capable of independent variation [13]. Pattern formation in an extended and periodic system involves couplings between different degrees of freedom and hence, we must tackle with nonlinear dynamics

of critical phenomena.

Experimental study of instabilities in this thesis is handled in two different ways: firstly a global study from the *amplitude dynamics* of the fundamental modes, and secondly a discrete study from the *phase dynamics* of each individual oscillator.

Firstly, we are going to present the most general and relevant aspects of instabilities in order to settle the basis of critical phenomena for a dissipative and extended system. Then, we will review the hydrodynamics of an open convective fluid layer, and the particular instability mechanisms which take part in the Bénard-Marangoni convection and in the hydrothermal waves that appear in the cylindrical cell experiment. A review of previous experiments with similar dynamics like ours is presented. Finally, we approach the understanding of phase synchronization transitions of an ensemble of limit-cycle oscillators under weak coupling.

1.1. Symmetry breaking instabilities

Beyond microscopic dynamics, most dissipative systems display lattice patterns with discrete symmetries above a homogeneous state in the macroscopic scales, for example a striped pattern (2D or 3D). Lattice patterns are said to be generated by symmetry breaking instabilities. Consider a variable, in a 1D-system of size L , with a spatial modulation $\lambda_o = \frac{2\pi}{k_o}$, thus it can be described by a periodic function $u(x, t)$ in the domain $x \in \mathcal{D}(-\frac{L}{2}, \frac{L}{2})$. A priori, this 1D-system is supposed to be extended if the characteristic correlation length of the system ξ verifies $\Gamma = \frac{L}{\xi} \gg 1$. This means that the spatial coherence of the system is much smaller than the spatial size. If we suppose that, in the case of a 1D-modulated pattern, ξ is of the order of λ_o , then the ratio verifying $\Gamma = \frac{L}{\lambda_o} \gg 1$ is commonly defined as the physical aspect ratio. Under this condition the 1D-dynamics is not affected by boundary conditions at the walls (provided that the correlation length is small enough). This modulation is defined as a pattern.

Nearby the threshold of an instability, the 1D-dynamics can be described by a simplified equation describing the slow modulations of the pattern from a linearly stable pattern (*original pattern*) towards an unstable one (*new pattern*). Consider that $u(x, t)$ is a slowly varying field and that its equation has a linear part (\mathcal{L}), and a nonlinear one (\mathcal{N}):

$$\mathcal{L}(\partial_t, \partial_x, \varepsilon)u + \mathcal{N}(u, \varepsilon) = 0$$

where ε is the control parameter and the system becomes unstable at the critical value ε_c . The nonlinear part can be written as a N th-degree Taylor polynomial like:

$$\mathcal{N}(u, \varepsilon) = \mathcal{N}_2[u, u; \varepsilon] + \mathcal{N}_3[u, u, u; \varepsilon] + \dots$$

Under finite changes of the control parameter and close to the threshold (from below), nonlinearities are capable of destabilizing a new pattern globally or locally. Nonlinearities may cause the new pattern to become stable avoiding linear unstable variables to diverge, or simply they may cause the attenuation of the new pattern returning to the previous one. The dynamical response of the system depends on the “energy functional” which can only be determined in the case of **variational, potential or Lyapunov** systems as:

$$\frac{\partial \varphi}{\partial t} = -\frac{\delta \mathcal{F}}{\delta \varphi} \tag{1.1}$$

where φ is an order parameter and \mathcal{F} is a Lyapunov functional. Dissipative systems are usually non-variational. However, under certain restrictions a Lyapunov functional can be obtained for a dissipative system [14, 15] when it shows relaxational dynamics (these systems achieve asymptotic regimes for sufficiently long times). Two minima in Eq. 1.1, or a double well-potential, drive the system to bistable patterns where two different patterns are solutions of the system for the same control parameter values.

Homogeneous patterns accomplish the continuous spatial translation symmetries while *stationary* patterns accomplish the continuous temporal translation symmetry. Time reversal symmetry is not accomplished by dissipative systems. Some discrete symmetries are (for finite and fixed τ and λ):

- (i) Temporal translation symmetry: $u_\tau(x, t) \equiv u(x, t + \tau) = u(x, t)$
- (ii) Spatial reflection symmetry or parity symmetry: $u_-(x, t) \equiv u(-x, t) = u(x, t)$
- (iii) Spatial translation symmetry: $u_\lambda(x, t) \equiv u(x + \lambda, t) = u(x, t)$

1.2. Nonlinear dynamics and instabilities

We are going to introduce some successful nonlinear models, like the complex Ginzburg-Landau equation, that are capable of describing critical phenomena and pattern formation. Afterwards, we classify instabilities according to their nature at the threshold: convective and absolute, first and second order. Regarding bistable regimes, which appear through first order instabilities, we will focus on the dynamics of fronts.

In hydrodynamics, a lattice pattern appears from spatiotemporal modulated flow lines (streamlines) which can be easily described, for weakly nonlinear regimes, in terms of **fundamental modes**. In a 1D-system we describe an oscillatory field:

$$\Psi(x, t) = \sum_{j=1}^n M_j(k_j, \omega_j) = \sum_{j=1}^n A_j(X, T) e^{i(k_j x + \omega_j t)}$$

where, for the j -th fundamental mode $M_j(k_j, \omega_j)$ ($j = 1, \dots, n$), k_j is its wave number and ω_j is its frequency. Thus, the phase of the j -th mode is $\phi_j = (k_j x + \omega_j t)$ and the corresponding phase velocity is $v_\phi = \omega_j/k_j$. The envelope of each mode or amplitude $A_j(X, T)$ is a slowly varying function with spatiotemporal scales X and T much longer than x and t , respectively.

A bifurcation takes place when the new pattern is described by a new fundamental mode or by a quantitative change in the modulus of the amplitude of a preexisting mode. These are called **critical modes**. The bifurcation is the result of the competition between fundamental modes which comes from nonlinear interactions. Regarding the stability diagram where lines (or surfaces) distinguish different regimes, we may come across singularities where two (or more) patterns may become unstable towards the same final pattern; from critical phenomena we adopt the concept of a codimension-2 (or 3, ...) point.

At the threshold ¹ of an instability, the envelope $A_j(X, T)$ of a critical mode is expected to fulfil a normal form equation. The third order complex Ginzburg-Landau equation is an example

¹The linear stability analysis provides the amplitude equations only near the threshold, far from the threshold they are no longer valid and the dynamics remains characterized only by the phase equations.

of such normal form, and describes a **primary bifurcation** from a homogeneous pattern towards a propagative pattern or traveling wave [$\Psi_v(x, t) = A_v(X, T) e^{i(k_v x + \omega_v t)}$]:

$$\partial_t A + v_g \partial_x A = \varepsilon A + (1 + ic_1) \partial_{xx} A - (1 - ic_3) |A|^2 A$$

where ε is the control parameter. The advection of a pattern, represented by the modulus A , is enclosed in the ∂_x -term where v_g is the group velocity ($v_g = \partial\omega/\partial k$); the diffusivity coefficient is enclosed in the real ∂_{xx} -term. Positive growth rate linear solutions of the form $e^{\sigma t}$ are saturated by the nonlinear term in $|A|^2 A$.

When the original pattern (departure pattern) is a stationary cellular pattern [$\Psi_s(x, t) = A_s(X, T) e^{i(k_s x)}$] the system is said to undergo a **secondary bifurcation**. Experimentally, many 1D-systems undergo several secondary instabilities before achieving weak turbulent regimes, for example: convection in a fluid layer under 1D-heating, the Taylor-Dean system, experiments in directional solidification and viscous fingering (a review of references will be given in a later section). At the threshold of such secondary instabilities, nonlinearities may also involve interactions between the amplitude of the wave envelope and the phase of the cellular pattern. Theoretically, these models are based on symmetry arguments describing patterns close to the threshold (Coullet [16] and Goldstein [17]). Far from the threshold, fruitful attempts carried by Gil [18, 19] have reproduced localized drifting domains, amplitude holes and spatiotemporal intermittency regimes. Nevertheless, a third order complex Ginzburg-Landau equation for the amplitude has also produced localized solutions [20] and, by adding a quintic stabilizing term, successful results have been obtained on describing modulated fronts [21, 22].

Far from the threshold, the stabilized Kuramoto-Sivashinsky equation is quite suitable to describe interfacial growing fronts, spatiotemporal intermittency and turbulent patches in open flows:

$$\phi_t = -\alpha\phi - \partial_{xx}\phi - \partial_{xxxx}\phi + \phi_x^2$$

where ϕ is a dimensionless function. Simulations by Misbah [23] and Brunet [24] have reproduced various experimental observations in hydrodynamics and crystal growth for stable and bistable regimes.

1.2.1. Absolute and convective instabilities

In the laboratory frame of reference, according to the group velocity ($v_g = \partial\omega/\partial k \neq 0$) generated by a small perturbation, instabilities can be classified into (see Fig. 1.1):

- **Convective**, when a small and localized perturbation grows while it moves away from the initial position at the same time that it drifts. In an extended system, if this perturbation does not trigger a global instability the new unstable domain is drifted with $v_g \neq 0$ until it fades out.
- **Absolute**, when a small and localized perturbation grows and propagates in all directions for a sufficiently long period of time. In an extended system, if this perturbation triggers a global instability the new unstable domain spreads over the whole system size.

Instabilities towards propagative patterns are intrinsically convective at the threshold and absolute far from the threshold for $v_g = 0$.

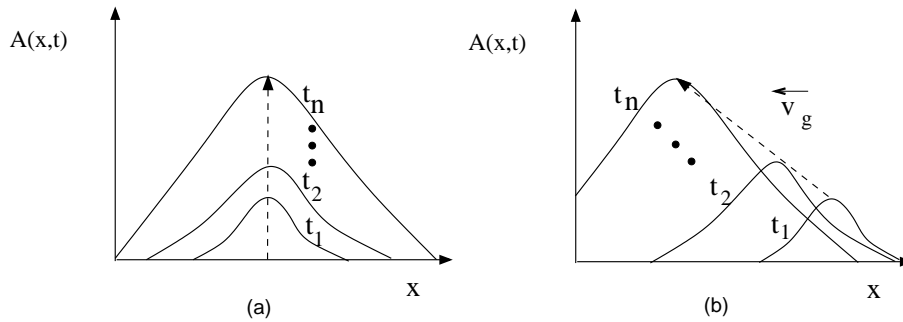


Figure 1.1: Sketch of the propagation of an absolute (a) and convective (b) instability in a 1D-system. $A(x, t)$ represents the amplitude of the perturbation and the arrow shows the direction of propagation while v_g is the group velocity.

1.2.2. First and second order instabilities

Instabilities might be classified attending to the finite jump, or any other peculiar behavior, of the order parameter of the system. Natural processes are dissipative, and therefore they are characterized by an irreversible thermodynamic inertia towards an “stable state”. Taking advantage of our cellular pattern of macroscopic convective cells, after an irreversible process (out-of-equilibrium transition), the interaction between convective cells yields a “stable pattern” in the asymptotic regime.

Once a “stable pattern” has been defined for a dissipative system, our purpose is to focus on equilibrium thermodynamics of critical phenomena. Then, we neglect microscopic phenomena on the following. Depending on the behavior of the order parameter when, under finite small changes of the control parameter, the system approaches a critical point, we can distinguish two different kinds of instabilities using the Ehrenfest classification [4] (see sketch in Fig. 1.2): *first order instabilities* when a discontinuity of the order parameter is produced, they are also known as **subcritical bifurcations**; and *second order instabilities* when the order parameter gently saturates as we go through the critical point, thus it is a continuous transition also known as a **supercritical bifurcation**.

Taking as the departure point a second order instability where the order parameter is φ , the correlation length of the system (ξ) is given by the order of the fluctuations of the order parameter $\delta\varphi$ which provides the interaction range between convective cells. From the “Ornstein-Zernike form” (1917) [25, 26] we define that the correlation of these fluctuations fulfill:

$$\langle \delta\varphi \rangle \sim \frac{e^{-x/\xi}}{x}$$

At the critical point ε_c the characteristic spatial (ξ) and temporal (τ) scales diverge [26, 27]. This means that, whereas the order parameter evolves continuously (i.e $\varphi \sim \sqrt{\varepsilon - \varepsilon_c}$), fluctuations are of the order of the system size because $\langle \delta\varphi \rangle \sim 1/x$ (long-range interactions), and the time that the system needs to bifurcate is longer as the system gets closer to ε_c (critical slowing down). Experimentally this kind of instabilities have been quantified in convective systems [28, 29], in nematic-smectic-A liquid crystals [30], in the Taylor-Dean experiment [31].

Discontinuities of the order parameter in first order instabilities produce hysteresis phenomena, therefore if we explore the system onwards (direct bifurcation) from the critical point ε_c , and over

the interval $\varepsilon_c < \varepsilon \leq 0$, the system exhibits coexistence between two stable patterns, this is the cause for bistable regimes to exist. From $\varepsilon \geq 0$ onwards [see Fig. 1.2(b)] the lower branch becomes unstable and the system exhibits a unique pattern. When the system is driven backwards (indirect bifurcation) it finally leaves the stable branch at ε_c , therefore it may show bistability in the same interval of coexistence $\varepsilon_c < \varepsilon \leq 0$. Bistability in the direct and indirect bifurcations is differently revealed because of hysteresis, we say that a stable pattern (or state) depends on the history. We are able to characterize the weak or stronger character of a first order instability according to the size of the finite jump of the order parameter.

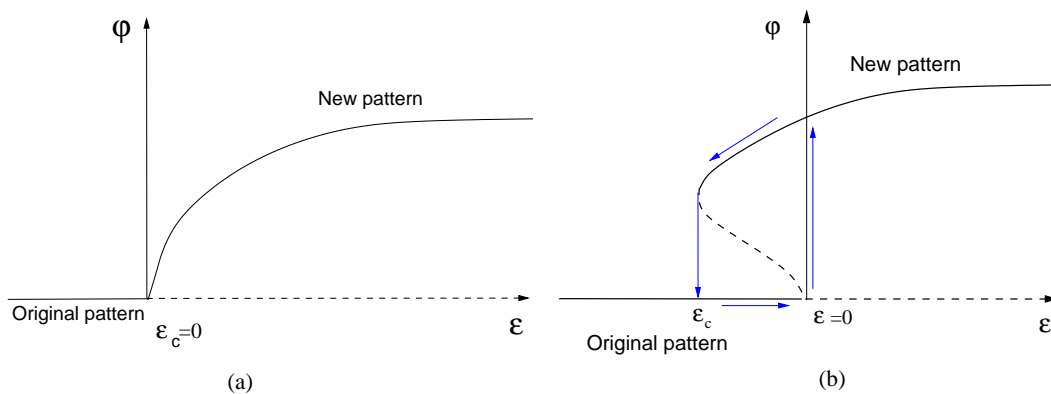


Figure 1.2: Bifurcation diagrams of (a) a supercritical bifurcation and (b) a subcritical bifurcation, arrows follow the hysteresis cycle. Solid branches represent stable patterns and dashed branches represent unstable patterns.

1.2.3. Fronts in bistable regimes

If the dynamics of a system could be described by a generalized potential [a variational system with a Lyapunov functional $\mathcal{F}(\varphi; \varepsilon)$] then, for a bistable regime where two different patterns coexist, the globally stable pattern (or phase) would correspond to a global minimum of the potential and the other metastable pattern would correspond to a local minimum [see Fig. 1.3(a,c)].

Both patterns are connected by a boundary front whose dynamics (interfacial dynamics) depends on the local mechanisms that couple the front. The front, as a coherent structure which belongs to large scales, will be coupled to the small spatiotemporal scale fluctuations which are represented by the characteristic modulation of the patterns at the interface. Depending on the control parameter ε and according to the aforementioned coupling, a propagation of the front may be possible or not.

We find fronts in many experiments which exhibit bistability like in convection of binary fluids [32, 33], in Faraday waves [34], in liquid crystals [35] and in catalytic reactions [36]. A similar front dynamics linked to subcriticality has already been modeled for binary fluids [37]; in this case, fronts connect a homogeneous and a traveling wave pattern.

The coupling mechanisms at the front were introduced heuristically by Pomeau [3] in the framework of the Landau theory [38] and metastability in reaction-diffusion equations. Most of the relevant mathematical treatment was developed by Fisher [39] for biological systems. The Fisher model is the simplest one from a reaction-diffusion equation with one reagent where φ is

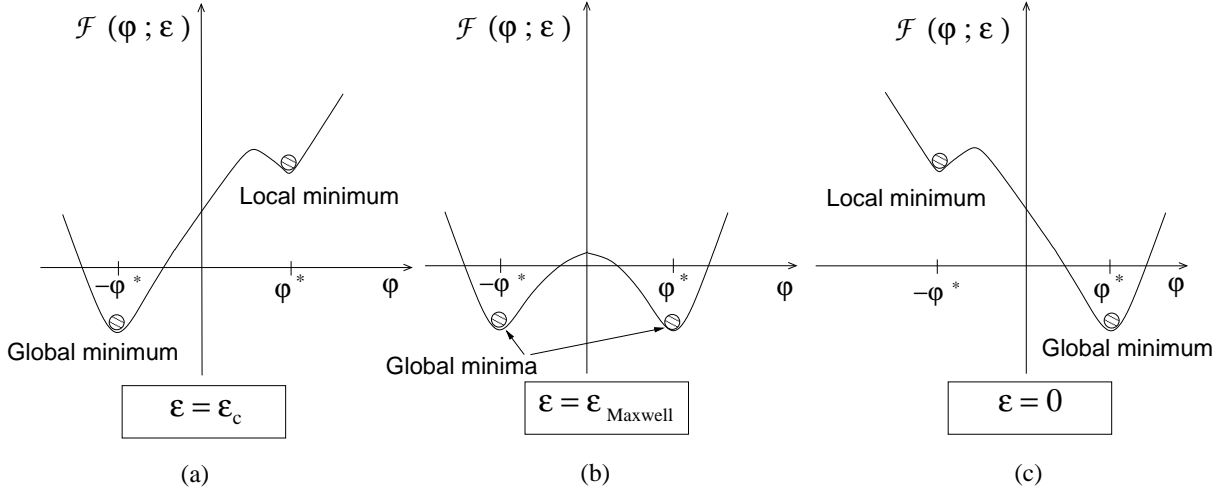


Figure 1.3: Lyapunov functional $\mathcal{F}(\varphi; \varepsilon)$ corresponding to a subcritical bifurcation, $\pm\varphi^*$ are scalar functions which represent two different pattern solutions of the potential at different values of the control parameter ε . At (a) $\varepsilon = \varepsilon_c$; (b) $\varepsilon = \varepsilon_{Maxwell}$, where $\varepsilon_{Maxwell}$ is the Maxwell point; (c) $\varepsilon = 0$.

a scalar function and ε is the control parameter:

$$\frac{\partial \varphi}{\partial t} = -\frac{\delta \mathcal{F}(\varphi; \varepsilon)}{\delta \varphi} = f_\varepsilon(\varphi) + D\partial_x^2 \varphi$$

therefore the velocity of propagation depends on the control parameter. Stationary fronts accomplish:

$$D\partial_x^2 \varphi + f_\varepsilon(\varphi) = 0$$

The Maxwell rule states that at one point, the Maxwell point $\varepsilon = \varepsilon_{Maxwell}$, two locally stable patterns ($-\varphi^*$ and φ^*) are connected by a stationary front (with a velocity of propagation $v_p = 0$):

$$\int_{-\varphi^*}^{\varphi^*} f_{\varepsilon_{Maxwell}}(\varphi) d\varphi = 0$$

If we suppose two different patterns at $-\varphi^*$ and φ^* respectively, depending on the control parameter (ε), the potential can be fitted to different polynomial curves (see Fig. 1.3). In Fig. 1.3(b), at the Maxwell point the two minima of the potential fulfill: $\mathcal{F}(-\varphi^*; \varepsilon_{Maxwell}) = \mathcal{F}(\varphi^*; \varepsilon_{Maxwell})$, thus the potential curve has two global minima (double-well potential) and the correspondent stable patterns coexist in neutral stability. In the corresponding subcritical bifurcation diagram we can represent the control parameter $\varepsilon = \varepsilon_{Maxwell}$, or in certain systems (like our 1D-cell) a finite interval $-\varepsilon_{Maxwell} \leq \varepsilon \leq \varepsilon_{Maxwell}$ for which $v_p = 0$ (see Refs. [35, 40–43]).

When $\varepsilon_c < \varepsilon < 0$ [see Fig. 1.3(a,c)] one of the global minima (depending on whether the system bifurcates directly or indirectly) converts into a local minimum. In this case, the front connects a stable pattern with a metastable pattern. From this situation onward, as we modify ε the front moves forward until the new stable pattern invades the whole system. Finally, for $\varepsilon > 0$ there is no front. To each potential functional $\mathcal{F}(\varphi; \varepsilon)$, depending on ε , it corresponds a different propagation velocity v_p .

Depending on the stability of patterns connected by fronts we can distinguish between: (i) fronts between two stable patterns (i.e. Küpers-Lorz instability [44]); (ii) fronts between a stable and an unstable pattern (i.e. first-order Fréedericksz transition in liquid crystals [40]).

Fronts that connect a homogeneous pattern with a lattice pattern are pinned (or locked) [45]. In reaction-diffusion systems like in catalytic reactions under a quasi-1D heating where there are two extremely different diffusion coefficients theoretical models try to reproduce stationary fronts in an interval of the control parameter [46, 47] where the velocity of propagation depends on the smallest diffusion coefficient.

According to the propagation velocity of the front, we use the following classification of fronts [39, 42, 48, 49]:

- **Normal fronts** between two stable patterns (neutral stability). If we suppose a variational system we can assign an energy to each pattern (E_1 and E_2). The propagation velocity v_p is proportional to the energy difference between both patterns (i.e. $v_p \approx \text{Const.}(E_2 - E_1)\varepsilon$) and it is not subjected to the history of the system. At the Maxwell point ($v_p = 0$) $E_1 = E_2$ for $\varepsilon > \varepsilon_{\text{Maxwell}}$ the front invades the pattern with the less favorable energy state with $v_p \neq 0$.
- **Fisher-Kolmogorov-Petrovsky-Piskunov fronts (FKPP)** between a stable and an unstable pattern. These fronts are characteristic of non-variational systems (with non-relaxational dynamics). The propagation velocity v_p can be measured in transient regimes and depends on the initial conditions. In the asymptotic state, the propagation velocity is always minimum (Maxwell point). But, differently to the normal fronts the behavior of velocity at the threshold is nonlinear (see Fig. 1.4). These fronts have been studied in liquid crystals [35, 40, 43]. In transients, when we place our system (the 1D-cell) below and close to the critical point, we are dealing with this kind of fronts. These fronts provide interesting features of the dynamics such as the *convective vs absolute* character of an instability.

Bistability can also be understood as the coexistence between patches with irregular fronts displaying the new pattern and the original one. These irregular fronts are well-defined fluctuating fronts and even they may fade away or collapse. This kind of bistable regimes are referred in this work as *mixed patterns* which are present in weak transitions to chaos. These mixed patterns have been usually identified as spatiotemporal intermittency regimes, for example the Rayleigh-Bénard convection in an annular gap [50] and in the Faraday experiment [34]. A similar behavior is found in experiments with open shear flows where the basic state (original pattern) is always stable, such as plane Couette [51], circular Couette and Poiseuille [52]. These instabilities have in common a “subcritical branch” sent to infinity [49].

1.3. An open fluid layer under free convection

A free convection experiment (under the gravity field $g\hat{z}$) consists of a fluid layer of depth d , subjected to a vertical temperature difference ΔT , which above the conductive regime becomes unstable when the viscous friction and heat diffusivity between fluid volumes are overcome. We may define the following characteristic time scales:

- The time scale of the *vorticity diffusion* (or viscous relaxation): $\tau_\nu = \frac{d^2}{\nu}$, where ν is the kinematic viscosity. τ_ν measures the time along which a perturbation of the velocity field is

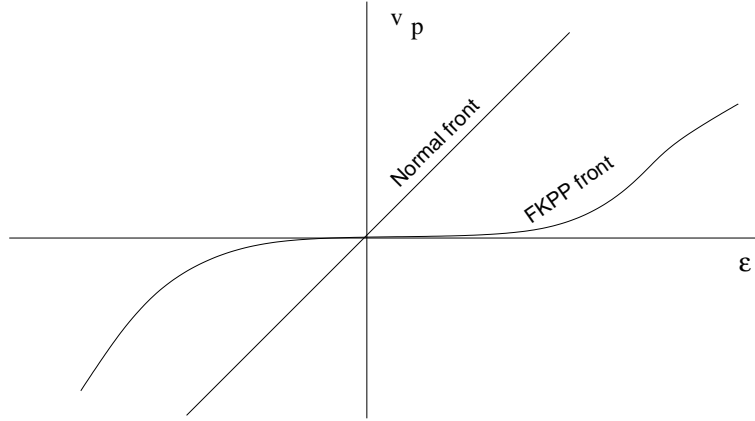


Figure 1.4: Sketch of the propagation velocity of a front $v_p(\varepsilon)$ which is a linear function in a normal front and nonlinear in a FKPP front.

damped.

- The time scale of *thermal diffusion*: $\tau_\kappa = \frac{d^2}{\kappa}$, where $\kappa = \frac{\lambda}{\rho c_p}$ is the thermal diffusivity, λ is the thermal conductivity and ρ is the fluid density. τ_κ is the time along which the heat coming from molecular vibrations is diffused.
- The time scale caused by the *Archimedean effect*: $\tau_g = \left(\frac{d}{g\alpha\Delta T}\right)^{1/2}$, where α is the volume expansion coefficient. τ_g is the time along which a fluid volume, which is not in equilibrium with its environment, moves upwards (or downwards by continuity) under a vertical temperature gradient.
- The time scale caused by the *Marangoni effect*: $\tau_\sigma = \left(\frac{\rho d^3}{\frac{d\sigma}{dT}\Delta T}\right)^{1/2}$, where σ is the surface tension $\sigma(T) = \sigma_o - \gamma(T - T_o)$ (generally $\gamma > 0$). τ_σ is the time along which an interfacial fluid element, which is not in equilibrium with its environment, moves over the surface under the traction produced by surface tension gradients.

From the dimensional analysis (Pi-theorem of Buckingham [53]), similarity allows us to combine different independent parameters which represent different physical mechanisms taking part in thermoconvective processes, to form the following dimensionless numbers:

- The **Marangoni number**: $M = \frac{\frac{d\sigma}{dT}\Delta T d}{\rho\nu\kappa} = \frac{\tau_\nu\tau_\kappa}{(\tau_\sigma)^2}$. It provides information about the compensation between pulling forces at the interface due to gradients of surface tension and dissipative phenomena in the fluid bulk.
- The **Rayleigh number**: $R = \frac{g\alpha\Delta T d^3}{\nu\kappa} = \frac{\tau_\nu\tau_\kappa}{(\tau_g)^2}$. It contrasts the buoyancy forces due to Archimedean effects with regard of dissipative phenomena. If we compare the dimensionless numbers above ($\frac{M}{R}$), convection is termed Bénard-Marangoni if $\frac{M}{R} \geq 1$. Marangoni convection corresponds to systems where the gravitatory effects can be neglected, otherwise if they are mainly responsible for the convection, it is termed Rayleigh-Bénard convection.
- The **dynamical Bond number**: $B_{OD} = \frac{R}{M}$. It compares the gravity effect that settles a planar air-fluid interface in front of surface tension responsible for the formation of menisci.

- The **Prandtl number**: $Pr = \frac{\nu}{\kappa} = \frac{\tau_\kappa}{\tau_\nu}$. It provides information about the competition between thermal and viscous diffusivities. Thus, for high values of Pr the temperature field guides the fluid dynamics, while for low values of Pr the vorticity field guides the fluid dynamics.
- The **Grashof number**: $Gr = \frac{g\alpha\Delta T d^3}{\nu^2} = \frac{Ra}{Pr}$. It compares the relative importance of buoyancy in front of viscous forces in such a way that the larger it is the stronger the convective current is.
- The **Biot number**: $Bi = \frac{hd}{\kappa}$, where h is the unit thermal interfacial conductance. It studies the heat flux at the air-fluid interface when the fluid layer is cooled by the air currents. Numerical simulations usually work with very small Biot numbers ($Bi \approx 0$), thus it is supposed that the layer is not cooled at the interface.

A fluid layer under convection evolves according to the following equations:

- (a) The Navier-Stokes equation. By breaking the BBGKY (Bogoliubov-Born-Green-Kirkwood-Yvon) hierarchy [54] conveniently, from the microscopic equations is possible to obtain a description of the dynamics in terms of the macroscopic variables. This is the case for the macroscopic Navier-Stokes equation which describes the movement of a Newtonian ² fluid element with velocity $\vec{v}(\vec{x}, t)$:

$$\left[\frac{\partial \vec{v}}{\partial t} + (\vec{v} \cdot \vec{\nabla}) \vec{v} \right] = \vec{g} - \frac{\vec{\nabla} p}{\rho} + \nu \nabla^2 \vec{v}$$

In our experimental conditions, we can apply to this equation the Oberbeck-Boussinesq approximation which considers that, under small variations of the temperature field, all the fluid properties remain constant except for the pressure term where density is temperature-dependent: $\rho = \rho_o(1 - \alpha\Delta T)$.

- (b) The continuity equation for an incompressible fluid is (mass conservation law): $\text{div } \vec{v} = 0$.
- (c) The heat conduction equation: $\partial_t T + \vec{v} \cdot \vec{\nabla} T = \kappa \Delta T$.

Boundary conditions for a flat fluid layer opened to the atmosphere can be classified into:

- (i) Mechanical conditions. Considering a rigid boundary at the fluid-solid interface and a free boundary at the air-fluid interface. On rigid boundaries with stick conditions $\vec{v} = (v_x, v_y, v_z) = (0, 0, 0)$, then from the continuity equation $\frac{\partial v_z}{\partial z} = 0$. At free boundaries without convection there are no tangential stresses $\frac{\partial v_x}{\partial z} = \frac{\partial v_y}{\partial z}$, then from the continuity equation $\frac{\partial^2 v_z}{\partial z^2} = 0$. The normal component of the vorticity ($\vec{\nabla} \times \vec{v}$) at the interface is $\zeta = \frac{\partial v_y}{\partial x} - \frac{\partial v_x}{\partial y}$, which for a rigid boundary $\zeta = 0$ and for a free boundary $\frac{\partial \zeta}{\partial z} = 0$.
- (ii) Thermal conditions. The principle of energy conservation is applied to rigid boundaries (fluid-solid) and the free interface (air-fluid) depending on the respective conductivities and diffusivities. The Newton's cooling law at the free interface in its dimensionless form is: $\nabla_z T = -Bi(T - T_{air})$.

²In a Newtonian fluid the coefficients of the viscous stress tensor do not depend on the velocity field.

1.3.1. Bénard-Marangoni convection

Bénard-Marangoni convection is driven by thermocapillary and thermogravitatory effects. Because surface tension decreases with temperature ($\frac{d\sigma}{dT} < 0$), thermocapillary forces (surface tension forces) acting on the free air-fluid interface, cause hot surface regions (with smaller surface tension) to be pushed towards colder regions (with higher surface tension). On the other hand, thermogravitatory effects pull up hotter fluid volumes (with smaller density) than their surroundings. Because of continuity also a downward fluid motion is produced.

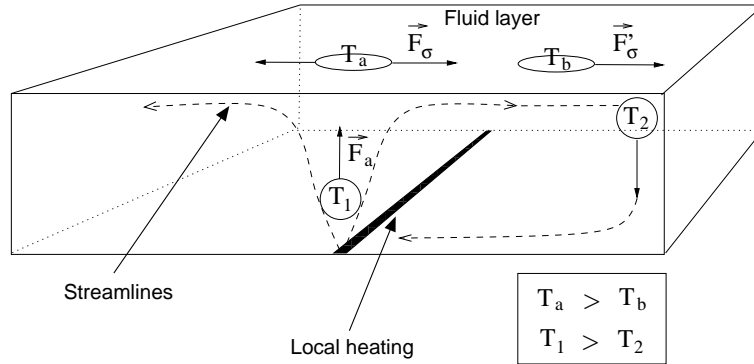


Figure 1.5: Sketch of the forces acting on a fluid element under Bénard-Marangoni convection.

In the case of the 1D-cell studied in the following chapters, we have sketched in Fig. 1.5 the destabilizing mechanisms on a fluid element of size l in the bulk. This fluid volume, regarding the surrounding temperature, has a local temperature gradient ΔT . The modulus of the Archimedean force is $|F_a| \sim \rho g \alpha (\Delta T) l^3$, where α is the volume expansion coefficient and ρ is the average local density. A fluid element on the interface is subjected to the surface traction force with modulus $|F_\sigma| \sim \Delta \sigma L$ where L is the perimeter of a surface element. Convective flows are produced, in the bulk of the fluid layer, because a coupling is produced between the displaced fluid elements on the interface (under surface forces \vec{F}_σ) and the ascending (under the buoyancy force \vec{F}_a) and descending fluid elements (by continuity).

1.3.2. Instability mechanisms of hydrothermal waves

In the case of the cylindrical cell studied in Chapter 5, we introduce the destabilizing mechanisms that, in a convective fluid layer, yield hydrothermal waves (HW). Hydrothermal waves were experimentally found in microgravity experiments with floating zones [55–57] in crystal growth processes (Czochralski method in a melting core) where oscillatory instabilities due to thermocapillary forces were responsible for the existence of inhomogeneities. Theoretically, Smith and Davis [58, 59] predicted the HW instability from the linear stability analysis, but without gravity.

In a fluid layer, thermocapillary convection arises under vertical and horizontal temperature gradients and from two competing effects: buoyancy forces and surface stresses. Consider an open fluid layer of depth d subjected to a horizontal thermal gradient ΔT_h along a distance L . Thermocapillary convection is easily afforded by working with large geometric aspect ratios ($\Gamma_g = L/d \gg 1$). In the following, we discuss the HW instability mechanisms considering that the interface deformations $z = \zeta(x, y, t)$ and surface temperature conductance are disregarded

by choosing a flat surface and $Bi = 0$. As soon as $\Delta T_h \neq 0$, a basic steady shear flow settles (*return flow*). The surface velocity (\vec{v}_ζ) points towards the colder wall, downstream (see Fig. 1.6). For Prandtl numbers $Pr > 1$, the fluid layer holds thermogravitatory effects (RB convection) induced by the gravitatory field (\vec{g}) and thermocapillary effects (Marangoni convection) induced by the surface tension: $\sigma = \sigma_o - \gamma(T - T_o)$, with $\gamma = -d\sigma/dT > 0$. Hydrothermal waves, counterintuitively, move upstream in the direction of the positive temperature gradient (from the colder side at T^- to the hotter one at T^+).

According to the theoretical approach given by Smith [60], in Fig. 1.6 we have sketched a fluid layer ($Pr > 1$) with a return flow given by the velocity field $\vec{u}(x, z)$ and the corresponding temperature profile $\Theta(x, z)$. The velocity field $\vec{u}(x, z)$ is supposed to transport heat disregarding viscous dissipation. Concerning the stabilizing effect of the temperature profile, a propagative disturbance along an initial hot line (\hat{y}) on the interface becomes unstable because of two mechanisms:

- (i) The hot line induces a Marangoni convection mechanism in which a surface flow comes out from the hot line towards the opposite sides ($\pm\hat{x}$), the upflow from the bottom layer is colder, and by continuity, the hot surface fluid turns down, producing a hot subsurface layer (see Fig. 1.6). This HW instability is triggered above a threshold (i.e. above a critical Marangoni number). The process is reversed when the hot line becomes colder below the critical Marangoni number.
- (ii) Because the colder upflow from the bottom layer has a smaller velocity than the interface velocity (\vec{v}_ζ), this velocity slows down on the right-side of the hot line, meanwhile parallel interface lines on both sides of the hot line reach the maximum temperature by conduction. This is the key effect for $Pr > 1$: the subsurface layer is at the maximum temperature by conduction in front of the convective motion of fluid volumes ($\tau_\kappa > \tau_\nu$). Then, as the downstream comes from the left-side wall with the highest temperature (T^+), at a certain moment, the surface tension at the hot line becomes higher (lowest temperature) than the surface tension at the adjacent left-side new hot line (highest temperature) (see Fig. 1.6) which will pull the disturbance upstream.

The balance between both mechanisms produces a net propagation of the disturbance (hot line) upstream ($-\hat{x}$) or with a small deviation, and with velocity \vec{v}_{HW} . In Fig. 1.6 longitudinal hydrothermal waves appear propagating towards the hotter wall at T^+ .

For high Prandtl numbers ($Pr > 10$) the wavevector is colinear or quasicolinear to the temperature gradient, if we define the angle $\psi = (\vec{k}, \vec{\nabla}T)$, then $\psi = 0^\circ$; this means that the disturbance propagates in the streamwise direction (\hat{x}). For small Prandtl numbers ($Pr < 1$), the instability mechanisms are the same but they act in a different way because of the dominant effect of inertial forces ($\tau_\nu > \tau_\kappa$). In this case, the wavevector \vec{k} characterizing HW is perpendicular to the temperature gradient direction $\vec{\nabla}T$, then $\psi \approx 90^\circ$; this means that the disturbance propagates in the spanwise direction (\hat{y}). For intermediate Prandtl numbers (i.e. $Pr = 10$) there is always a degree of tilting $0 < \psi < 90^\circ$. Depending on the number of components defining \vec{k} we may distinguish between 1D-HW and 2D-HW.

If there are no interactions, that is nonlinear effects between surface waves and hydrothermal waves, for instance we choose a flat interface between a fluid layer and a passive gas, the stability analysis by Smith and Davis [58] without gravity and without surface conductance ($Bi = 0$) predicts the following patterns:

- Stationary longitudinal rolls due to similar mechanisms as for the Marangoni convection for a *linear flow*. This instability, in the case of a return flow, was not found by Smith and Davis.
- 1D-HW (HW1) are traveling waves which can be defined by one component wavevector \vec{k} . Experimentally, they are found in rectangular cells with a variety of Pr numbers. This instability has been found to be supercritical in annular cells [61] and in rectangular cells [29, 62]. The instability toward HW1 is generally linked to the presence of a line-source or of a line-sink in 2D-experiments.
- 2D-HW (HW2) are traveling waves defined by two component wavevector \vec{k} . Experimentally they have been found in cylindrical cell experiments [63] and in rectangular cells [29].

How do HW depend on the aspect ratio? By varying the aspect ratio, the stability diagram has similar curves although for different thresholds, but the underlying hydrodynamics between traveling hydrothermal waves and longitudinal rolls (corrotational rolls) is the same [29, 64].

Because in these systems traveling waves solutions are convective, from a theoretical point of view J. Pried and G. Gerbeth [65] reported an interesting contribution to the problem of determining the position of thresholds in convective instabilities versus absolute ones. They found that for $Pr > 1$ the absolute threshold is above the convective one.

Nonlinear interactions between hydrothermal and surface waves are still a matter of discussion [57, 58, 66] and still leave a great area for research in both experiments and theory.

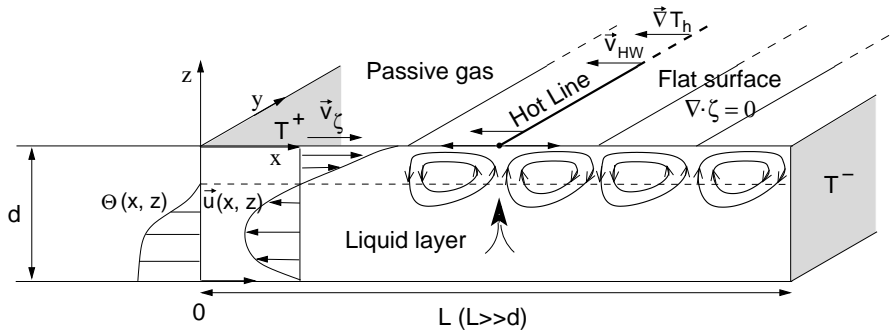


Figure 1.6: Hydrothermal waves instability mechanism disregarding boundary effects at the lateral walls and vertical heat fluxes. The streamlines in the bulk of the fluid are closer to the free surface so the “cooled from below” temperature profile in the return flow is balanced by the dominant conductive regime in the subsurface layer where the HW instability takes place.

1.4. Similar dynamics in other experimental systems

A wide variety of patterns with different global and local dynamics have been obtained in the last decades from very different dissipative extended systems. These systems may also show coherent patterns like bursting patches, fronts, pulses, amplitude holes, solitons, defects, sources and sinks. Some of these experiments are: the printer’s instability [67, 68], circular liquid column arrays [69–71], directional solidification [72], directional viscous fingering [73], the Taylor-Dean system [31], rotating fluid layer under convection [44], electroconvection in liquid crystals with

rectangular cell [74, 75], lateral heating in a rectangular cell [29, 64, 76–78], lateral heating in an annular cell [50], lateral heating in a cylindrical cell [63], quasi-1D heating in a rectangular cell [79–86].

Many different extended hydrodynamical systems display **mixed patterns** which are characterized by the presence of irregular patches emerging over a basic lattice pattern like in the Faraday experiment (2D), and in 1D experiments such as the convection of rectangular and annular layers, or over homogeneous patterns like in the plain Couette experiment (2D).

1.5. Phase synchronization phenomena

A system is referred as complex if its dynamics has to be described by a high number of degrees of freedom, for example a network of N -nonlinearly coupled oscillators. These oscillatory units might be chaotic or “self-oscillating”. Self-oscillating means that trajectories in the plane phase space fall into an isolated limit-cycle orbit which corresponds to a periodic solution. These kind of oscillators are self-sustained, nonlinear and dissipative. This ensemble of coupled oscillators may interact all-to-all (a global interaction like in the mean-field theory), locally (between the nearest neighbors like in the Ising model for paramagnetic to ferromagnetic transition) and nonlocally (farther than the nearest neighbors like chemical waves in a reactive-diffusion system).

Systems which exhibit self-sustained oscillations are frequently found in nature and in the laboratory: biological systems [87, 88], chemical reactions like the Belousov-Zhabotinsky [89, 90] and the CO oxidation on platinum crystal [91], semiconductor lasers [92], superconductors (Josephson-junction arrays [93]), pacemakers cells in the beats of cardiac rhythms [94], dynamics of neurons [95], ecosystems [96, 97]. These oscillatory systems may reach synchronized or self-entrained states when an adjustment of different frequencies between oscillators is produced. Synchronization is the result of a coupling between oscillators and may be sustained by nonlinearities. The natural consequence of a synchronization process is the generation of an ensemble of synchronized oscillators defined as a “cluster of synchronization”. The dynamics imposed by this clustering process can simplify complex dynamics like in weak-turbulent regimes by synchronizing several degrees of freedom, an example is the presence of vortices and spirals in turbulent hydrodynamic systems like in Couette-Taylor [98], cylindrical Couette [98], von Kármán [99]; target and spiral waves in reaction-diffusion chemical systems [91, 100, 101]; and spirals in RB convection [102]. There are interesting theoretical models on extended multicellular systems [103, 104].

In complex systems we may distinguish three main groups of synchronization processes: *complete synchronization* of phase and amplitude, *intermittent synchronization* when a phase desynchronization is produced like bursts, and *phase synchronization* which is the most common type of synchronization in extended systems in nature and in laboratory experiments. In nature, fireflies emit synchronized flashes and pacemaker cardiac cells tune beats; in the laboratory, circuit arrays of semiconductor lasers “simulate” nonlinear weak coupled pendulums which may bifurcate towards inphase self-pulsing states, catalytic CO oxidation on platinum where spiral and target waves arise from coupling between chemical oscillators, and in the present work an array of convective cells which by nonlinear diffusive and nonlocal coupling display diverse synchronized phenomena.

Phase synchronization arise from nonlinear interactions between oscillators (i.e. convective

oscillators become coupled by thermal or vorticity diffusion interactions). These interactions yield an entrainment process in which, after a finite time, more oscillators fall into the same *phase dynamics*, but only those fulfilling a synchronization condition that will be explained later on. Under certain constraints given by the driving forces phase mismatches $\Delta\Psi_{ij} = |\Psi_i - \Psi_j|$ with $i, j = 1, \dots, N$ are produced between N -oscillators (convective cells).

The complete phase Ψ_i , or raw phase, of one i -oscillator is a function of various phase contributions:

$$\Psi_i = \Psi_i(\phi_i^{v_1}, \dots, \phi_i^{v_n}, \phi_i^c, \phi_i^o)$$

We expect Ψ_i to be a “cumulative function” of time; and the instantaneous frequency to be $\omega_i|_{t_o} = \partial_t \Psi_i$. A new synchronized pattern contributes to each oscillators phase Ψ_i , by adding a new phase component ϕ_i^c (critical phase) which is responsible for the phase synchronization transition. The original oscillatory phase state (at the departure pattern) is given by $\phi_i^{v_j}$, which corresponds to n -fundamental travelling modes [v_j stands for travelling modes with ($j = 1, 2, \dots, n$)], and ϕ_i^o represents a constant phase shift which can be provided, for example, by a previous stationary pattern. In Fig. 1.7(a) we show a simple example of the raw phase Ψ_i belonging to an individual i -oscillator. This raw phase corresponds to a new bifurcated phase of an i -oscillator with critical frequency ω_1 . This critical frequency guides the dynamics in this bifurcation and is superimposed to the original i -oscillator phase which is described by two fundamental frequencies ω_2 and ω_3 . The Fourier spectrum of the raw phase Ψ_i in Fig. 1.7(b) provides the fundamental frequencies of the new phase of the i -oscillator. We observe that frequencies ω_1 and ω_2 are very close, thus a beating phenomenon on larger temporal scales (involving several oscillators) might emerge under the proper coupling between oscillators, Γ_{ij} .

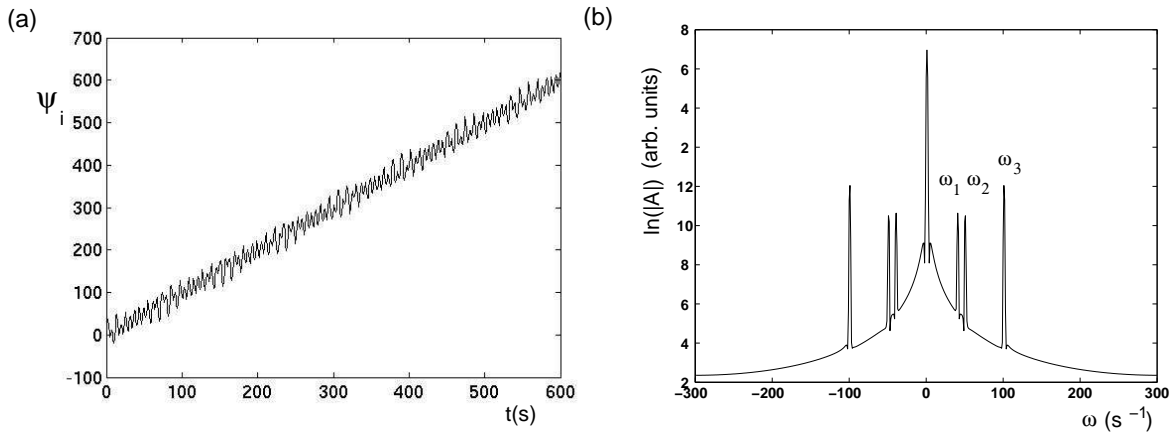


Figure 1.7: (a) Raw phase Ψ_i of an individual oscillator; (b) Fourier spectrum of the signal (a) where $|A|$ is the modulus of the amplitude of the raw phase.

A phase description of the dynamics is suitable far from the threshold of an instability when the amplitude becomes turbulent. The main idea of a phase synchronization phenomena is the appearance of low-dimensional patterns imposing in the system a new slow scale (T) which is given by the cluster phase dynamics, $\Phi(T)$. If we take for instance an ensemble of coupled oscillators, $\Phi(T)$ might be viewed as the result of a phase mismatch between close fundamental frequencies. Meanwhile, fast scales (t) are given by the individual oscillators phase dynamics

$\Psi_i(t)$. In Fig. 1.8 we have sketched an array of equispaced oscillators, each vector on the circles represents the oscillators phase $\Psi_i(t)$, the solid line represents the slow phase dynamics $\Phi(T)$. The cluster phase $\Phi(T)$ describes a state which is the envelope of each phase contribution.

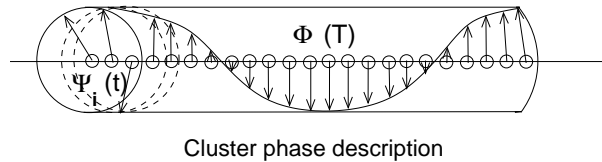


Figure 1.8: Phase space of an array of equispaced oscillators with individual phases $\Psi_i(t)$ and cluster phase $\Phi(T)$.

1.5.1. Weak coupling in an ensemble of synchronized oscillators

Disregarding topology, an ensemble of weakly coupled oscillators is capable of locking each others phases. This statement was discovered experimentally by Huygens (synchronized clocks, 1665) and later on developed by Winfree (biological communities [5]), Kuramoto (chemical waves [105]) and Osipov [106, 107]. Kuramoto established the theoretical basis for phase synchronization phenomena in *the phase reduction theory of weakly coupled limit-cycles* [105], a midway between nonlinear dynamics and statistical physics. Modelling extended 1D system of N -coupled oscillators undergoing global phase instabilities under certain constraints, such as weak coupling between oscillators subjected to the same driving force, has allowed to build rich phase spaces [108].

The Kuramoto model (KM) describes an ensemble of N -identical oscillators with weak³ and global coupling Γ_{ij} . The phase dependence on time is given by:

$$\frac{d\phi_i}{dt} = \omega_i + \sum_{j=1}^N \Gamma_{ij}(\phi_i - \phi_j) \quad (1.2)$$

The simplest attractive-repulsive coupling might be a sinusoidal function $\Gamma_{ij}(\phi_i - \phi_j) \sim \sin(\phi_i - \phi_j)$. In the KM, natural frequencies ω_i , are obtained from a suitable phase distribution function, which depends on the dynamics. This distribution function is only applied to those oscillators whose phases fulfil: $\phi_i \leq |\Phi - \Delta|$ where Δ is the maximum phase mismatch permitted to assure synchronization, and Φ is the phase of the cluster. This is the condition for synchronization.

In Fig. 1.9(a) we show an example of coupling $\Gamma_{i,i+1} = \Psi_i - \Psi_{i+1}$ between two adjacent oscillators with a small mismatch between their phases [see Fig. 1.9(b)]. A coupling of this kind is supposed to drag a greater ensemble of oscillators to fall into the phase of synchronization ϕ_i^c . In order to quantify phase mismatches between these coupled oscillators the cross-correlation vector $\langle \cos(\phi_i^c), \cos(\phi_{i+1}^c) \rangle$ shown in Fig. 1.9(c) provides information about the times of maximum phase correlation and the times of minimum phase correlation.

From the synchronized phase of the system Φ (cluster phase), KM defines the complex order parameter ($\sigma e^{i\Phi}$) for the ensemble of N -oscillators with random phases ϕ_j :

³Weak coupling between oscillators assures a “regular” circle orbit, otherwise for a strong coupling orbits may become too “irregular” to use a perturbation method.

$$\sigma = \frac{1}{N} \sum_{j=1}^N e^{i|\phi_j - \Phi|} \quad (1.3)$$

The parameter σ is a measure of the coherence of the system, like a control parameter.

On synchronization in oscillatory and complex systems, the field of Networks has introduced the study of “geometric networks” where the topology of the network, which refers to the spatial distribution of the oscillatory units, might be time-dependent [109, 110]. In Chapter 4 we propose a suitable model to describe synchronization in the 1D-array of convective oscillators.

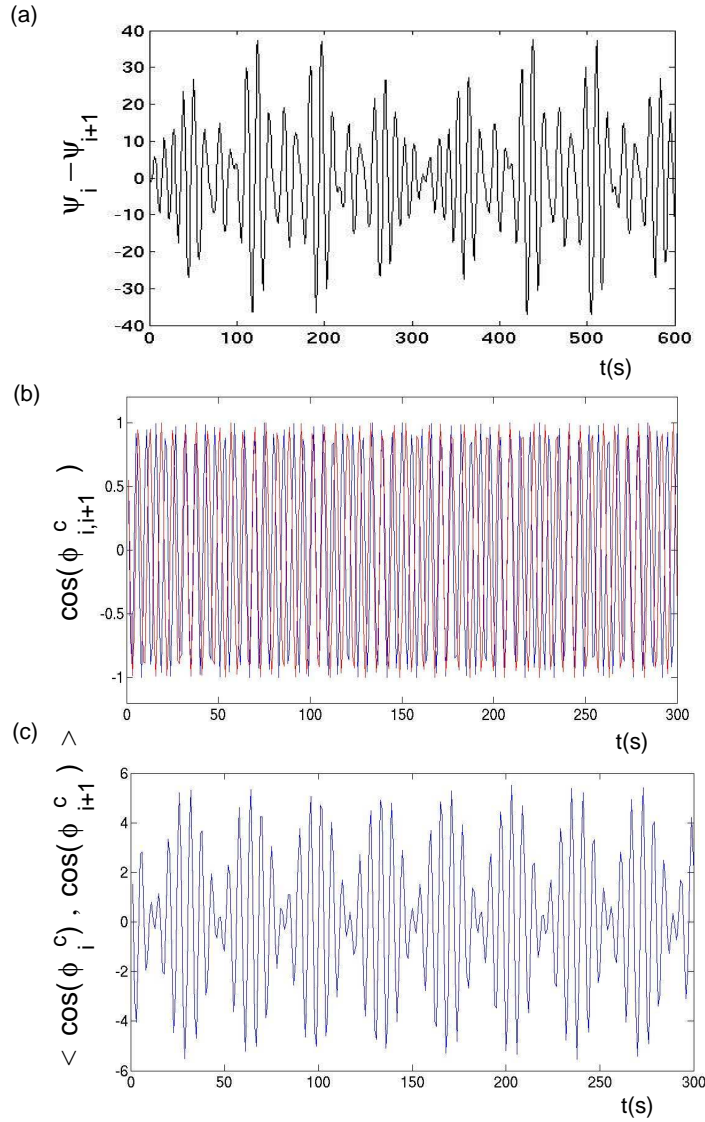


Figure 1.9: Given two coupled adjacent oscillators i and $i + 1$: (a) coupling given by the raw phase difference $\Gamma_{i,i+1} = \Psi_i - \Psi_{i+1}$; (b) cosine representation of their critical phases: $\cos(\phi_i^c)$ and $\cos(\phi_{i+1}^c)$; (c) cross-correlation between cosines of (b): $\langle \cos(\phi_i^c), \cos(\phi_{i+1}^c) \rangle$.

Chapter 2

Laboratory techniques and signal processing in the 1D-cell experiment

In this chapter we introduce the experimental setup of the 1D-cell. It basically consists of a convective rectangular cell, the optical system and the fluid layer. We also describe the acquisition system. This experimental system is an improved version of a previous experiment developed by Burguete *et al* [79, 111]. In pursuit of robustness, we choose the appropriate materials of the cell in order to control the temperature profile at the bottom, and besides in order to obtain a horizontal level of the bottom. Therefore, at permanent regimes the experimental cell can yield a proper quasi-1D heating at the center and along the largest direction of the cell. We have developed a stable optical system, which implements the shadowgraphy technique of fluid visualization, in order to quantify with accuracy the relevant parameters (amplitudes, wave numbers and frequencies) nearby the thresholds of the fluid layer instabilities, and besides, in order to cover the maximum extension of the cell.

On the other hand, we try to explain novel contributions in the way data is analyzed by means of the discrete fast Fourier transform and demodulation techniques. Complex demodulation techniques applied to the study of weakly nonlinear regimes in convective systems were developed for the first time by Kolodner and Williams [112]. Two different analysis have been carried owing to two different physical interpretations of the system. Firstly, a *global analysis* applied to a continuous convective field whose patterns break certain symmetries and are the result of linear and nonlinear combination of fundamental global modes. Energy transference between modes is produced as the result of nonlinear competition between modes. And secondly, a *discrete analysis* applied to a lattice of convective cells which is a 1D-array of roughly 80 nonlinearly coupled oscillators. These oscillators may become phase synchronized in space and time. Nonlocal (further than first neighbors) and nonlinear interactions between nearby oscillators are produced taking part of “phase” diffusion processes.

2.1. The rectangular cell

The fluid layer of depth d is placed in a narrow convective channel $L_x \times L_y$ (470 mm \times 60 mm) shown in Fig. 2.1(a). This layer lies over a flat surface, a mirror of thickness 3 mm. As it is shown in Fig. 2.1(b), the bottom of the mirror is in contact with a heater rail of 1 mm (thickness)

which provides the heating line (HL) in the \hat{x} direction. This rail belongs to an aluminum block with an inner closed water circuit thermoregulated by a heater bath (Polystat 86696-35, 1500 W and 11 l/min) at T_h . Under conditions $d = 4$ mm and $T_h = 48$ °C, the temperature measured at HL (on the mirror surface) differs from the one given by the heater bath probe in -3.00 K. The heat diffusion in the \hat{y} direction is smoothed because of the thermal diffusivities of the mirror and the lateral walls of Plexiglass that surround the heater rail (see Table 2.1). Therefore, at the asymptotic regimes, in the transversal direction of the cell (\hat{y}) the system achieves a temperature profile similar to a Gaussian one. The lateral walls are two aluminum blocks (coolers) whose temperatures are controlled at $T_c = 20 \pm 0.1$ °C by means of a secondary water circulation. This temperature is given by the cooler bath probe (Polystat 1268-32) and it is the same as the one measured at the top of the aluminum blocks. The shorter boundary walls at the opposite extremes of HL are made of Plexiglas. These elements are assembled inside a Delrin block. The effective dimensions of the cell are 450 mm \times 60 mm \times 15 mm ($L_x \times L_y \times L_z$), however the optical setup allows us to visualize only a centered area from an upper surface of 310 mm \times 60 mm [Fig. 2.1(a)]. The geometric aspect ratios for $d = 4$ mm are: $\Gamma_x = L_x/d = 112.5$ and $\Gamma_y = L_y/d = 15$. The ratio $\Gamma_x/\Gamma_y = 7.5$ allows us to classify the system as weakly confined in \hat{x} .

In comparison with other experimental setups which use a resistive wire (20 μ m - 50 μ m diameter) [83–85] where there is a coupling between the temperature fields of the circulating flow and the wire, in our system because of the great thermal inertia (induced by the high thermal diffusivities of the Delrin and the Plexiglass see Table 2.1) couplings between the temperature field of the convective flows and the HL are not expected.

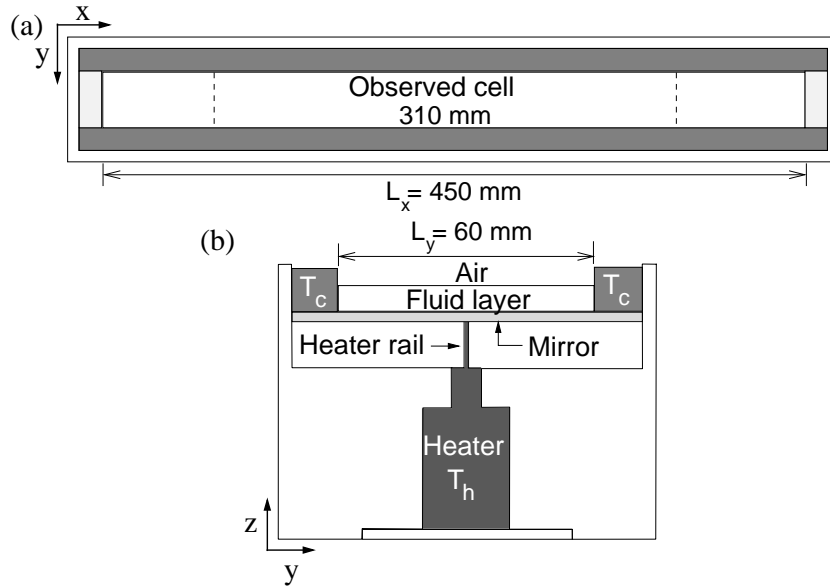


Figure 2.1: Sketch of the experimental setup. Rectangular cell: (a) top view and (b) cross section of the rectangular vessel. The scaling in both views is different

The cell is placed inside a container which allows the air to circulate freely along the upward direction \hat{z} until the air flow encounters the beam-splitter surface 47 cm above the fluid surface (see Fig. 2.2). The room temperature outside the cell is measured with a T-thermocouple and

Material	Thermal conductivity χ ($\text{Wm}^{-1}\text{K}^{-1}$)	Thermal diffusivity κ (m^2s^{-1}) $\cdot 10^{-8}$
Aluminum	237	9975
Glass	0.93	43
Plexiglass	0.19	663.42
Air	0.0256	1938
Delrin	0.24	440.14
Silicone oil	0.1	7

Table 2.1: Thermal conductivities and diffusivities of the materials involved in the cell.

controlled at $T_r = 20 \pm 0.1$ °C by means of an air conditioner. The upper surface of the fluid layer is opened to the atmosphere, hence a turbulent air flow is expected.

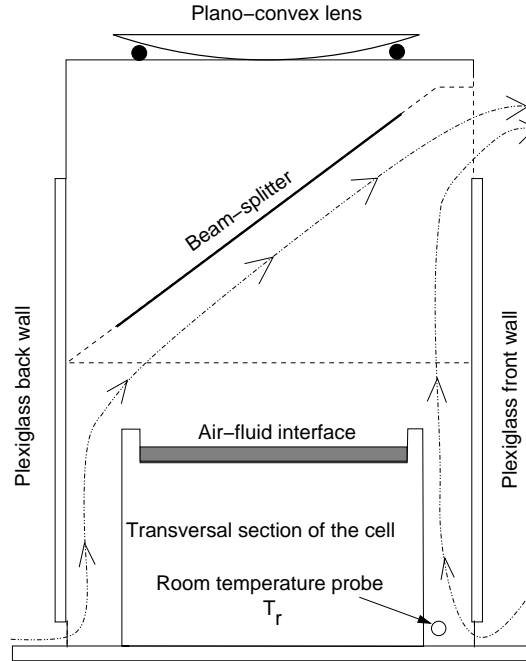


Figure 2.2: Lateral side view of the container. Arrows represent air flow streamlines. Dashed lines do not disturb the air circulation.

2.2. The fluid

The fluid used is a silicone oil (brand name: *Dow Corning 200*) with a nominal viscosity of 5 cSt (see properties on Table 2.2). It is a polymer (PDMS) *polydimethyl siloxane* with a lineal chain,



This fluid is transparent to visible light and therefore it is suitable for the shadowgraphy technique. Patterns arising from a thermoconvective dynamics are observed using the shadowgraphy technique which reproduces the variations of the temperature field from the variations of the

refractive index field in the bulk of the fluid layer. The Lorentz-Lorenz equation [113] determines the dependence of the refractive index with density:

$$\frac{n^2 - 1}{n^2 + 2} = \rho \cdot Const.$$

This fluid has a low volatility, the depth of the fluid layer diminishes with a rate of approximately 0.01 mm/24 hours through the interfacial area (270 cm²) at 20 °C, so we can work (in the range of temperatures applied) with the layer opened to the atmosphere. Under this condition, we assume that the depth, measured with a precision of 0.01 mm with a micrometric screw, remains constant along each measurement (for a maximum of 900 s). The small surface tension of the silicone oil in comparison with the water one (70 mN m⁻¹) allows us to disregard the meniscus effect at the boundary walls. The low density sends heavier impurities to the bottom of the fluid layer.

From the corresponding physical properties on Table 2.2, two relevant dimensionless numbers can be obtained: the Prandtl number $Pr = \nu/\kappa \approx 75$ (\equiv compares *viscous diffusivity* vs *thermal diffusivity*) and the dynamic Bond number $Bo_D = R/M \approx 1.05$ (at $d = 3$ mm) (\equiv compares *thermogravitatory effects* vs *thermocapilarity effects*). As well, at $d = 3$ mm and $\Delta T_v = 30$ K, we can determine two characteristic time scales: the viscosity time scale $\tau_\nu = 2$ s and the thermal diffusivity time scale $\tau_\kappa = 135$ s. Consequently the dynamics is driven by the field with the longest characteristic time scale, the temperature field.

The fluid dynamics is in the context of the Oberbeck-Boussinesq approximation for the working range of temperatures. Thus, variations in viscosity and thermal conductivity with temperature are disregarded, only density variations with temperature are allowed.

Physical properties of the 5 cSt silicone oil	
Surface tension (25°C)	$\sigma = 19.7 \text{ mN m}^{-1}$
Thermal conductivity (50°C)	$\lambda = 0.117 \text{ W m}^{-1} \text{ K}^{-1}$
Thermal diffusivity ($\lambda/\rho c_p$)	$\kappa = 6.68 \cdot 10^{-8} \text{ m}^2 \text{ s}^{-1}$
Kinematic viscosity (25°C)	$\nu = 5 \text{ cSt} (5 \cdot 10^{-6} \text{ m}^2 \text{ s}^{-1})$
Density (25°C)	$\rho = 913 \text{ kg m}^{-3}$
Refractive index (25°C)	$n = 1.3960$
Linear expansion coefficient	$\alpha = 0.00105 \text{ K}^{-1}$
Surface tension/temperature	$\frac{\partial \sigma}{\partial T} = -8 \cdot 10^{-5} \text{ N m}^{-1} \text{ K}^{-1}$

Table 2.2: Physical properties of the 5 cSt silicone oil.

2.3. The thermal field

We have checked the thermal inertia of the cell and the temperature homogeneity along HL for a fluid layer of $d = 3$ mm, although the present results are obtained with a less powerful heater bath (1000 W and 10 l/min). We measure the temperature along HL with a type T-thermocouple. The temperature of the thermocouple is recorded by a computer controlled multimeter (HP-34970A) and the error associated is $\pm 1^\circ \text{ C}$.

- Selecting 50°C in the heater bath, we measure temperatures along the interface air-fluid with a computer motorized translator stage (C-842.20). In Fig. 2.3(a) we show a transient regime that finally achieves the asymptotic one. It corresponds to 460 measurements along 45 cm of the cell during 1 hour, therefore the temperature at the HL becomes stable in 26 minutes. Under these conditions, we infer that the system needs at least one hour to achieve permanent regimes. The average temperature is $36.12 \pm 0.67^{\circ}\text{C}$ [see Fig. 2.3(b)], fluctuations in the last stretch are important because the translator stage has to be manually displaced.

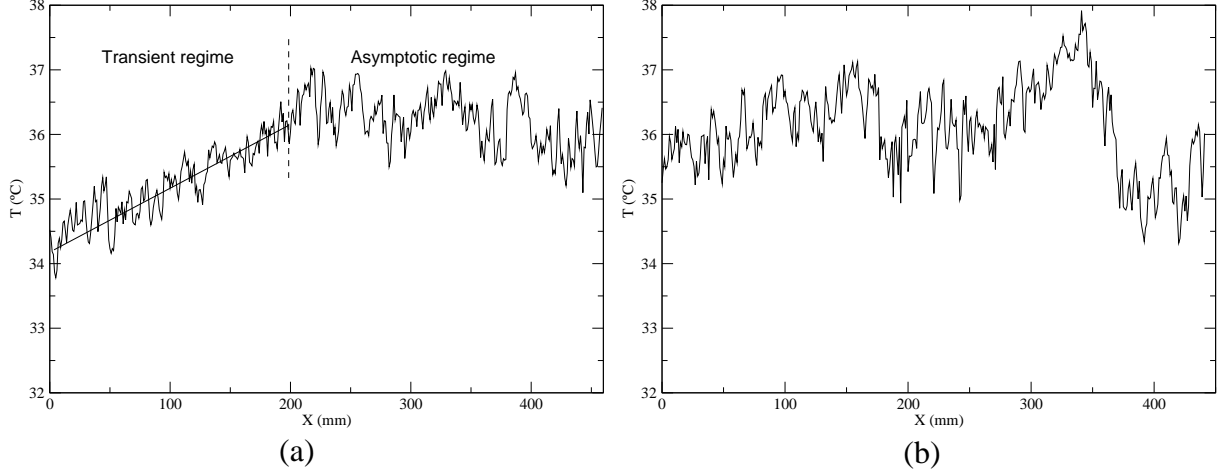


Figure 2.3: (a) Temperature profile at the heating line (HL) in a transient regime. (b) Temperature profile at the heating line (HL) in an asymptotic regime.

- Selecting 50°C in the heater bath, but measuring at fixed positions in the cell, we determine from results in Fig. 2.4(a) that: (1) the temperature at the rail (the temperature probe is in contact with the rail surface) is of approximately 5 K less than the temperature at heater bath probe; (2) the temperature difference between the extreme positions of the HL is of 0.68 K; (3) the horizontal temperature difference between the rail and the boundary walls is constant.
- Selecting 45°C in the heater bath, and using a different temperature sensor (hypodermic probe HYP1) from results in Fig. 2.4(b) we check: (1) a difference of 5 K between the temperatures at heater bath and the rail; (2) a temperature difference between the extreme positions of the HL of approximately 1 K.

Fourier analysis has been applied over measurements obtained with a new bath (Polystat-86696, 1500 W and 11 l/min) for which the temperature difference between the heater bath and the HL (on the mirror surface) is of 3 K, and also the temperature difference between the opposite extremes of the HL is expected to be diminished.

2.3.1. The control parameters

The relevant control parameters in the quasi-1D convective dynamics are:

- The depth of the fluid layer d , we have worked in between $1 \text{ mm} \leq d \leq 5 \text{ mm}$.

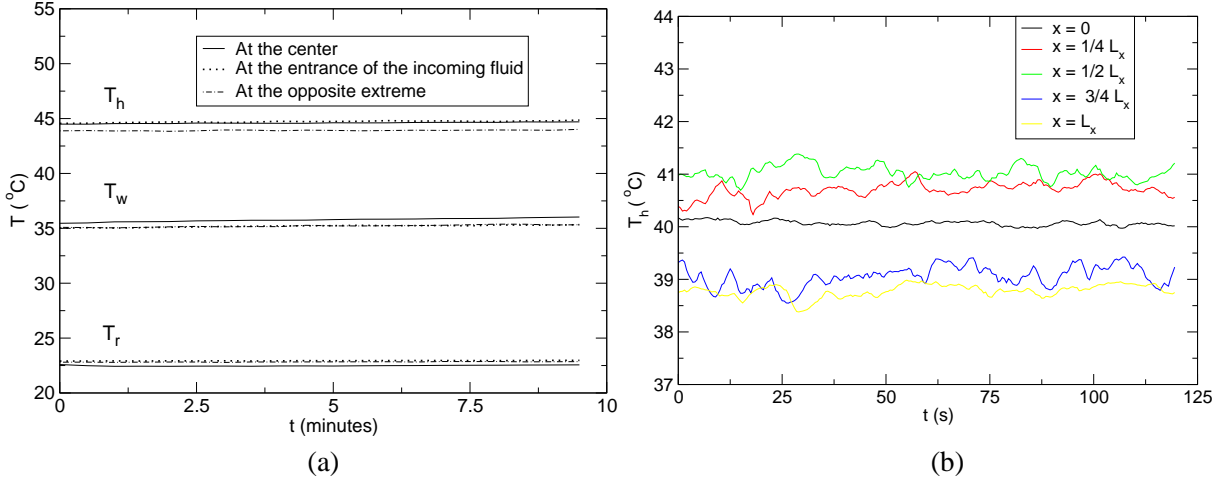


Figure 2.4: (a) Temperatures at the heating line HL (T_h), at the boundary wall (T_w) and the room temperature (T_r). These temperatures are controlled during 9.5 min at the center of the cell and the two opposite extremes. (b) Temperatures at fixed positions along HL ($L_x = 44$ cm) for 120 s.

- The vertical temperature difference $\Delta T_v = T_h - T_r$, keeping $\Delta T_v < 65^\circ\text{C}$ in order to maintain the dimensional stability of the polymer chain.
- The horizontal temperature gradient $\Delta T_h = T_h - T_c$. According to previous results with a similar cell [79] the dynamics does not qualitatively change with the horizontal temperature gradient.

Under these conditions, we have obtained the smallest threshold for the primary bifurcation at $d = 4.5$ mm. To build the stability diagram we have explored depths $d = 2.5, 3, 3.5, 4, 4.5$ and 5 mm. To locate the different asymptotic regimes we have worked with step (steps are given by small values of ΔT_v) $|\Delta T_v| = 2$ K, except at $d = 2.5$ mm with a bigger step ($|\Delta T_v| = 5$ K) and some isolated measurements at $d = 3.5$ mm looking for TW. Meanwhile boundaries have been defined with a maximum step of $|\Delta T_v| = 1$ K. To determine the nature of the bifurcations at $d = 4$ and 4.5 mm, we increase and decrease ΔT_v with steps of $|\Delta T_v| = 1, 0.5$ and 0.3 K, allowing the system to achieve the asymptotic state for 1 hour in the ascending sequences, and 3 hours in the descending sequences nearby the threshold.

2.4. Shadowgraphy technique

This technique has been very widely used in other convective systems, for example in isotropic fluids [15, 114, 115, 115] and in nematic liquid crystals [116, 117]. Our shadowgraphy flow-visualization system is sketched in Fig. 2.5 where elements are kept at fixed positions. The shadowgraphy image on the screen is a symmetric grey modulated pattern along a central dark line which corresponds to the HL. It is caused by the thermal lenses effect which produces brighter profiles from convergent rays contrasted with darker profiles from divergent rays. The shadowgraphy technique is obtained using a high diameter plano-convex lens (diameter 31 cm and focal length + 100 cm) which provides a parallel light beam which is sent through the patterned fluid

layer. The light beam crossing the fluid layer suffers different deflections depending on the refractive index gradients. In consequence, the analysis of the spatiotemporal periodicity of the modulation of the light beam, that has crossed the fluid layer, provides information about the temperature field of a certain pattern. In a similar experimental cell the deflection induced by traveling waves was below $1 \mu\text{m}$ for a depth of 3 mm [79], therefore the information analyzed is expected to come from the convective flow in the bulk. Once it is reflected back at the mirrored bottom the output beam is projected into a screen by means of a beam-splitter (tilted 45°). In order to obtain quantitative results for a sequence of measurements, the light intensity of an incandescent light bulb (white and incoherent light from a $6\text{V } 5\text{A}$ bulb) is controlled with a power supply (Agilent E3644A).

The image on the screen is recorded with a charge coupled device or CCD (Hamamatsu C5405 with a resolution of 570 units of pixels \times 485 units of pixels) keeping constant the focal length, the aperture and the gain in order to quantify the evolution of the grey profile nearby the onset of an instability.

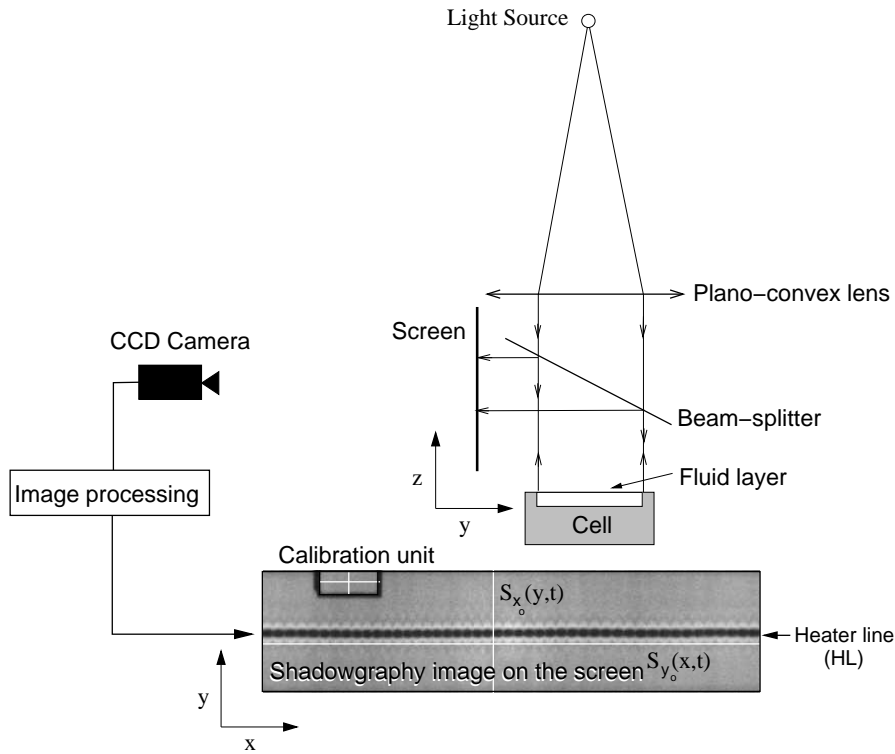


Figure 2.5: Optical setup for the shadowgraphy technique.

Periodically at a frequency of 1 s^{-1} , a line over the bright modulation next to HL is recorded to obtain a spatiotemporal diagram $S_{y_o}(x, t)$, and another line placed perpendicular to HL (at a central position x_o) is also recorded to obtain a spatiotemporal diagram $S_{x_o}(y, t)$. Regarding the maxima of brightness, the acquisition system inspects the grey profile averaging over a temporal sequence, for times longer than the viscous relaxation ($21 \text{ s} > \tau_\nu \approx 2 \text{ s}$), in order to select a fixed position y_o to record $S_{y_o}(x, t)$ (see Fig. 2.8). Thresholds are measured designing an acquisition system in order to obtain low contrasted shadowgraphy images (selecting a suitable position y_o). In this way we try to avoid spatial harmonics arising from the nonlinear optics. Hence, unstable

convective modes are roughly the unique unstable modes that are present at the onset of the instability and this fact allows us to quantify strictly the evolution of critical amplitudes (the screen effects due to refraction and absorption have been disregarded because the screen is a thin film of Plexiglass).

2.4.1. The calibration process

In the analogical to digital data conversion, the grey level is quantified from the light intensity of the shadowgraphy image. Grey levels remain always between 0 and 255. In the acquisition process, we select a dynamical range of reference between two extreme intensity values, generally a minimum of 0 and a maximum of 150, and never over the maximum recommended value of 192. To quantify data close to the onset of an instability, we keep constant every reference value along a sequence of measurements.

Each spatiotemporal diagram $S_{y_o}(x, t)$ is the result of a spatial and temporal sampling process (at equally spaced intervals) determined by the image acquisition board (VISION-plus with a resolution of 512×512 units of pixels) connected to the CCD, and the developed software. For all the measurements we work with a temporal frequency sampling of 1 s^{-1} which is below the characteristic time scales of the convective dynamics (the thermal diffusivity time scale $\tau_\kappa \approx 135$ s and the vorticity diffusivity time scale $\tau_\nu \approx 2$ s) in order to avoid any possible aliasing effect (Nyquist criteria [118]). A calibration process in \hat{x} and \hat{y} is carried at the beginning of each measurement extracting the grey profiles of a mirror unit placed next to the cell (see Fig. 2.5). These grey profiles allows us: (i) to perform a spatial calibration to map spatial units of the real continuous signal into the discrete signal $S_{y_o}(x, t)$ (we extract an average value of 0.625 mm per pixel); (ii) to perform a calibration of the light bulb by measuring the average illuminance (we keep constant the illuminance along a sequence of measurements).

2.5. Data analysis I: A global view of the convective field

In this section we work with continuous convective field signals that correspond to lattice patterns. We describe the Fourier transform and demodulation techniques that have been applied in order to analyze these lattice patterns and present particular examples of patterns with and without 1D-fronts.

Spatiotemporal diagrams $S_{y_o}(x, t)$ and $S_{x_o}(y, t)$ are real input signals obtained over two perpendicular lines. These diagrams show patterns with spatial and temporal modulations. The Fourier analysis techniques are a powerful tool to decompose continuous modulated signals. In the bidimensional Fourier space (k, ω) we define the Fourier transform $\mathcal{U}(k, \omega)$ which is a complex output signal of a continuous function $u(x, t)$:

$$\mathcal{U}(k, \omega) = \frac{1}{2\pi} \int \int_{-\infty}^{\infty} u(x, t) e^{i(kx + \omega t)} dx dt$$

On the discrete signal $S_{y_o}(x, t)$, and identically for $S_{x_o}(y, t)$, we apply the *matlab* algorithm of the discrete fast Fourier transform (2D-FFT), which in the bidimensional space (k, ω) corresponds to a distribution of j -peaks ($j = 1, \dots, N$) whose maxima, the j -modes $M_j(k_j, \omega_j)$, are located at $(k_j \equiv \frac{\partial \phi_j}{\partial x}; \omega_j \equiv -\frac{\partial \phi_j}{\partial t})$ with amplitude A_j , wave number k_j and frequency ω_j . Now $S_{y_o}(x, t)$

can be expressed as:

$$S_{y_o}(x, t) = \sum_j A_j(x, t) e^{i(k_j x + \omega_j t)}$$

Because the original signals $S_{y_o}(x, t)$ and $S_{x_o}(y, t)$ contain background distortions (spatial and temporal large scale modulations coming from the experimental devices like the illumination or the air conditioner) the mean must be conveniently removed. Temporal and spatial steady distortions contribute in the Fourier space to enlarge the central peak $M(0,0)$, whereas continuous spatiotemporal background to enlarge the thickness of the axis (\hat{k} and $\hat{\omega}$). Therefore, we remove the average background signal $B_o(x, t) = \langle S_x(x, t) \rangle_x^\dagger \langle S_x(x, t) \rangle_t$ by dividing the original signal, thus we obtain the new signal:

$$S_{B_o}(x, t) = \frac{S_{y_o}(x, t)}{B_o(x, t)}$$

In order to minimize the effect of a rectangular window in the 2D-FFT (convolution of the transformed signal with a square wave ¹), the signal $S_{B_o}(x, t)$ is multiplied by a Hamming window [119], $W(x, t)$, in the (x, t) -space before transforming: $S(x, t) = S_{B_o}(x, t) \cdot W(x, t)$.

The transformed signal is (FFT stands for fast Fourier transform):

$$S(k, \omega) = FFT[S(x, t)] = \sum_j A_j(k, \omega) \otimes \delta(k, \omega) + c.c.$$

In Fig. 2.6 we show different Fourier spectra corresponding to different 1D-patterns. These spectra consist of several peaks which correspond to fundamental modes and their harmonics. The fundamental modes are: the stationary mode $M_s(k, 0)$ for a *stationary pattern*, the right-traveling mode $M_{v+}(k_v, \omega)$ or the left-traveling mode $M_{v-}(k_v, -\omega)$ for a *propagative pattern*, both contrapropagative modes (or antiphase modes) are coupled with the stationary mode which determines a resonant triad, for an *alternating pattern*. We might consider that the Fourier spectrum is an energy representation in terms of competing modes. A diffusive system, like ours, generates in the Fourier space rough Gaussian peaks.

2.5.1. Bidimensional complex demodulation technique

The complex demodulation technique consists in transforming the original signal by selecting on the Fourier spectrum the mode $M_j(k_j, \omega_j)$ under study. By means of a low-pass filter, a Butterworth filter of sixth order $F_{Butt}(k, \omega)$ centered at $M_j(k_j, \omega_j)$,

$$F_{Butt}(k, \omega)|_{M_j} = \frac{1}{1 + (\sqrt{2} - 1) \left(\frac{(k-k_j)^2}{r_k^2} + \frac{(\omega-\omega_j)^2}{r_\omega^2} \right)^6}$$

¹The convolution is defined as:

$$(F \otimes G)(x) = \int_{-\infty}^{\infty} F(x-x') \cdot G(x') dx'$$

which means that (FFT is the fast Fourier transform):

$$FFT[f(x) \cdot g(x)] = \frac{1}{2\pi} (F \otimes G)(k)$$

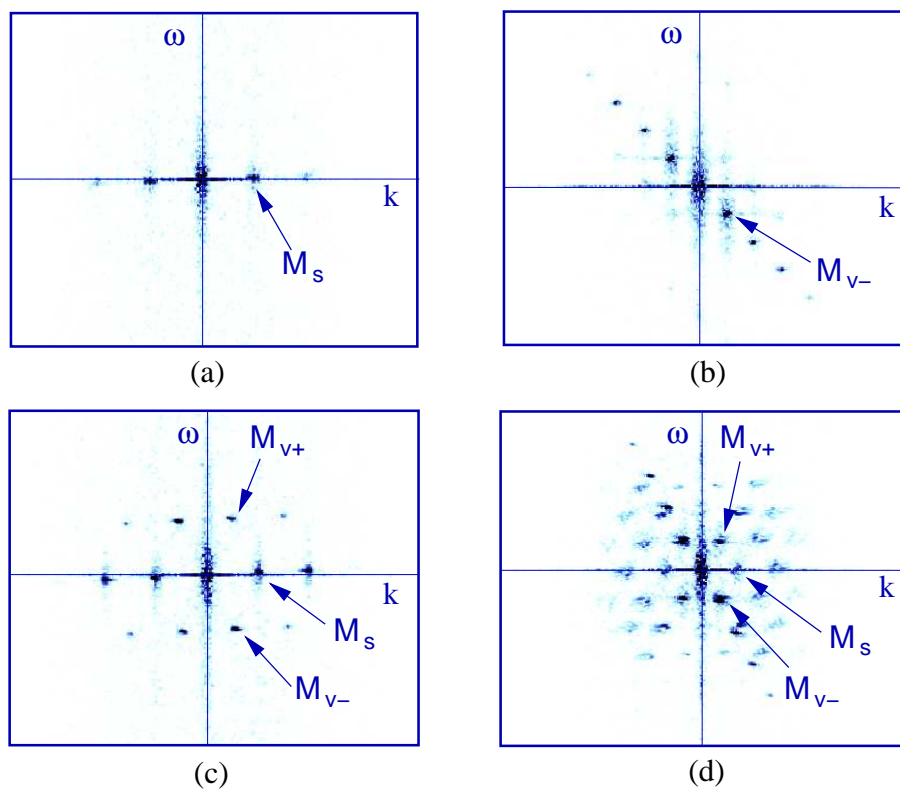


Figure 2.6: Fourier spectra corresponding to: (a) a stationary wave $M_s(k_s, 0)$ and its *c.c.*; (b) a left-traveling wave $M_{v-}(k_v, -\omega)$ and its *c.c.*; (c) two counterpropagative waves $M_{v\pm}(k_v, \pm\omega)$ and the stationary wave $M_s(k_s, 0)$ in a weakly nonlinear regime, and their *c.c.*; (d) two counterpropagative waves $M_{v\pm}(k_v, \pm\omega)$ and the stationary wave $M_s(k_s, 0)$ in a strongly nonlinear regime, and their *c.c.*. In the spectra white color corresponds to zero values and dark color to large volumes (Fourier peaks).

and selecting the proper radii (r_k and r_ω) in order to avoid the neighboring transform tails that arise from the Gibbs' phenomenon (lobes emerge from the convolution of the original signal with a window), we remove the remaining modes. The filtered signal is ²:

$$S_{\text{filt}}(k, \omega) = S(k, \omega) \cdot F_{\text{Butt}}(k, \omega)|_{M_j}$$

Because the absolute value $|S(k, \omega)|$ is an odd function ($|S(k, \omega)| = |S^*(-k, -\omega)|$) we work with peaks inside the semi-space defined by $0 \leq k \leq \pi$ and $-\pi \leq \omega \leq \pi$.

We take special care of: (i) stationary modes on the \hat{k} axis, or modes nearby the central peak $M(0, 0)$; and (ii) when the background signal comes from localized patterns in bistable phenomena. In consequence, we must check results on $(|A_j|, k_j, \omega_j)$ obtained from demodulation techniques straightforward from the Fourier spectra. In this case the amplitudes are obtained applying the *Parseval identity* which states that [regarding the applied window $W(x, t)$]:

$$\int \int_{-\infty}^{\infty} |S_{B_o}(x, t) \cdot W(x, t)|^2 dx dt = \int \int_{-\infty}^{\infty} |S_{B_o}(k, \omega) \otimes W(k, \omega)|^2 dk d\omega$$

The right-hand side of this equality is nothing but the integration of the energy spectral density. Amplitudes are obtained integrating peaks over ellipsoidal surfaces whose axes are determined from the shape of the peaks. A better resolution in the Fourier spectrum means less dispersive base of peaks which might be improved in time by recording longer diagrams, however the spatial resolution is limited by the size of the plano-convex lens in the case of $S_{y_o}(x, t)$.

To get back to the original (x, t) -space, we apply the inverse fast Fourier transform (FFT^{-1}) to the filtered region on the Fourier spectra containing the j -mode:

$$S_j(x, t) = FFT^{-1}[S_{\text{filt}}(k, \omega)|_{M_j}] = A_j(x, t) e^{i\phi_j(x, t)}$$

Once the window has been removed, the new signal might be averaged over the (x, t) -space ($\langle \rangle_{x, t}$). But in order to improve accuracy (reduce the errors), we choose a critical amplitude value μ to build a binary transfer function to be applied into the inverse space signal $S_j(x, t)$. Finally, we obtain the average values of the amplitude $|A_j|$, wave number k_j and frequency ω_j over the normalized amplitude regions which satisfy the criteria $A_j(x, t) / \max A_j(x, t) \geq \mu$ with $0 < \mu < 1$. In this way we obtain over these regions (x_μ, t_μ) , for the selected j -mode, the modulus of the amplitude:

$$|A_j| = \langle |S_j(x, t)| \rangle_{x_\mu, t_\mu} + \delta A_j$$

the wave number:

$$k_j(x, t) = \frac{\partial \phi_j(x, t)}{\partial x}; \quad k_j = \langle k_j(x, t) \rangle_{x_\mu, t_\mu} + \delta k_j$$

and the frequency:

$$\omega_j(x, t) = -\frac{\partial \phi_j(x, t)}{\partial t}; \quad \omega_j = \langle \omega_j(x, t) \rangle_{x_\mu, t_\mu} + \delta \omega_j$$

δA_M , δk_M and $\delta \omega_M$ are the standard deviations. This is the cause why in graphs shown in this work from demodulation techniques analytical error bars are smaller than the data symbols (squares, circles, ...).

²Given the matrices A_{ij} and B_{ij} , the product $A_{ij} \cdot B_{ij}$ is a new matrix with elements $C_{ij} = A_{ij} B_{ij}$.

2.5.2. A practical application to a pattern without fronts

If we take as an example an experimental spatiotemporal diagram from the 1D-cell in a regime consisting of two counterpropagative modes and a stationary mode [see the corresponding spatiotemporal diagram in Fig. 2.7(a)]:

$$S_{y_o}(x, t) = A_s e^{i(k_s x)} + A_{v+} e^{i(k_v x + \omega t)} + A_{v-} e^{i(k_v x - \omega t)}$$

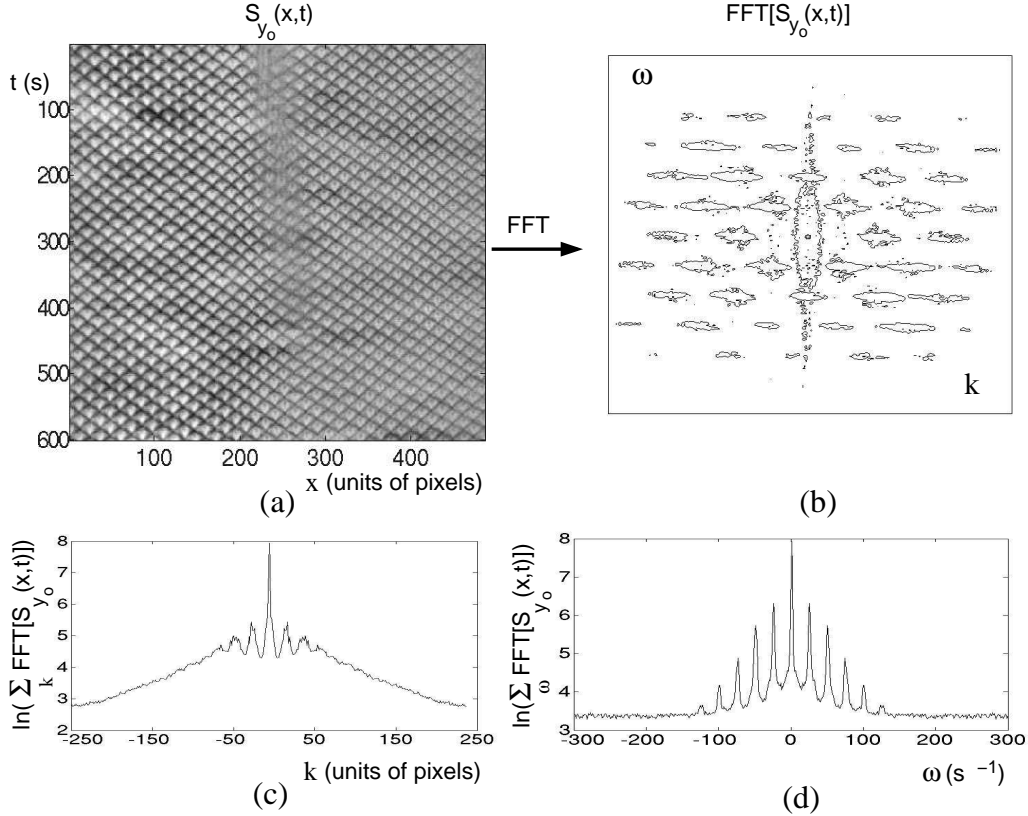


Figure 2.7: (a) Spatiotemporal diagram $S_{y_o}(x, t)$ for an alternating pattern at $d = 4$ mm and $\Delta T_v = 23$ K; (b) the corresponding bidimensional Fourier spectrum; (c) logarithm of the Fourier spectrum over k ; (d) logarithm of the Fourier spectrum over ω .

The resonant triad information (amplitudes, wave numbers and frequencies) can be extracted from the Fourier spectrum $2D\text{-}FFT[S_{y_o}(x, t)]$ [Fig. 2.7(b)] or by demodulation techniques. Otherwise if we had worked with two different 1D-FFT analysis, we would have obtained the same information as from the graphs in Fig. 2.7(c-d).

At the same time, the acquisition system is recording the vertical signal $S_{x_o}(y, t)$ at a central position x_o [see the dynamics of the grey level profile in graphs in Fig. 2.8].

2.5.3. Extracting subcritical parameters from bistable patterns

Demodulation techniques allow us to characterize the dynamics of localized patterns and fronts. The amplitude of the demodulated signal $A_j(x, t)$ for a chosen mode $M_j(k_j, \omega_j)$ (from the signal

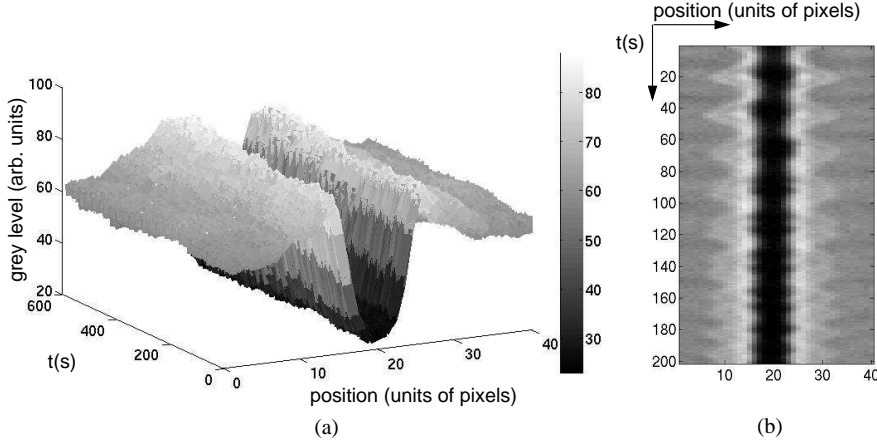


Figure 2.8: For an alternating pattern at $d = 4$ mm and $\Delta T_v = 23$ K: (a) dynamics of grey profiles corresponding to the vertical recorded signal $S_{x_o}(y, t)$; (b) spatiotemporal diagram $S_{x_o}(y, t)$.

$S_{y_o}(x, t)$ is processed by disregarding the normalized amplitude below a critical value $\mu = 1/e$; actually, we assume that the surface of the demodulated amplitude fits a decaying exponential function. Under these conditions, we define the following parameters on $A_j(x, t)$:

- (i) The **coherence length** L_c is the average size of localized patterns regardless of the nature of their boundaries: stationary or fluctuating fronts. A similar parameter is defined in other systems like in the Küppers-Lorz instability [120], the plane Couette flow [121] and the Belousov-Zhabotinsky reaction [122].
- (ii) The **velocity of propagation** v_p of a 1D-front is determined by measuring the velocity of the front defined by the amplitude of the new traveling mode. This method is not suitable for fluctuating boundaries.
- (iii) The **invasion rate** σ_{inv} is the ratio between the total surface occupied by the amplitude domains belonging to a certain mode with respect to the total extension of $S_{y_o}(x, t)$. This parameter is determined for a new unstable mode invading the whole system.
- (iv) The **attenuation length** ξ is measured for coexisting patterns, and it is the length for which the new unstable pattern penetrates further beyond the coexisting domain [123]. We choose the unstable mode which represents the new pattern, and we measure the length for which its amplitude decays according to $A_j \sim e^{-x/\xi}$ (from critical phenomena [26]), where ξ is a correlation length of the system. This parameter might be understood as a “spatial memory” inside the neighboring domain. This measurement is not suitable for fluctuating boundaries.

2.5.4. A practical application to a pattern with fronts

In Fig. 2.10(a,b) we show the filtered domains (with $\mu = 1/e$) of the spatiotemporal diagram $S_{y_o}(x, t)$ (see Fig. 2.9, for $d = 4$ mm and $\Delta T_v = 28$ K) where the TW domain and the ALT

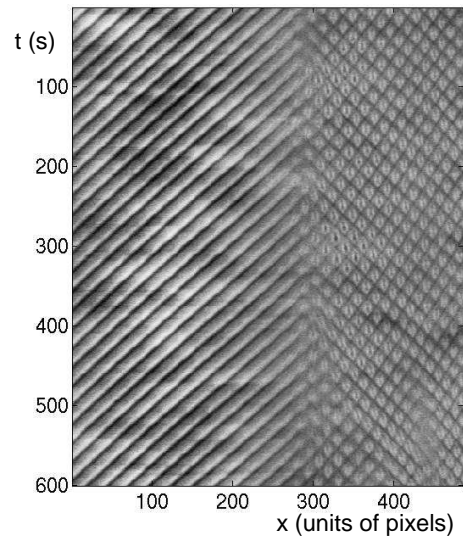


Figure 2.9: Spatiotemporal diagram $S_{y_o}(x, t)$ at $d = 4$ mm and $\Delta T_v = 28$ K.

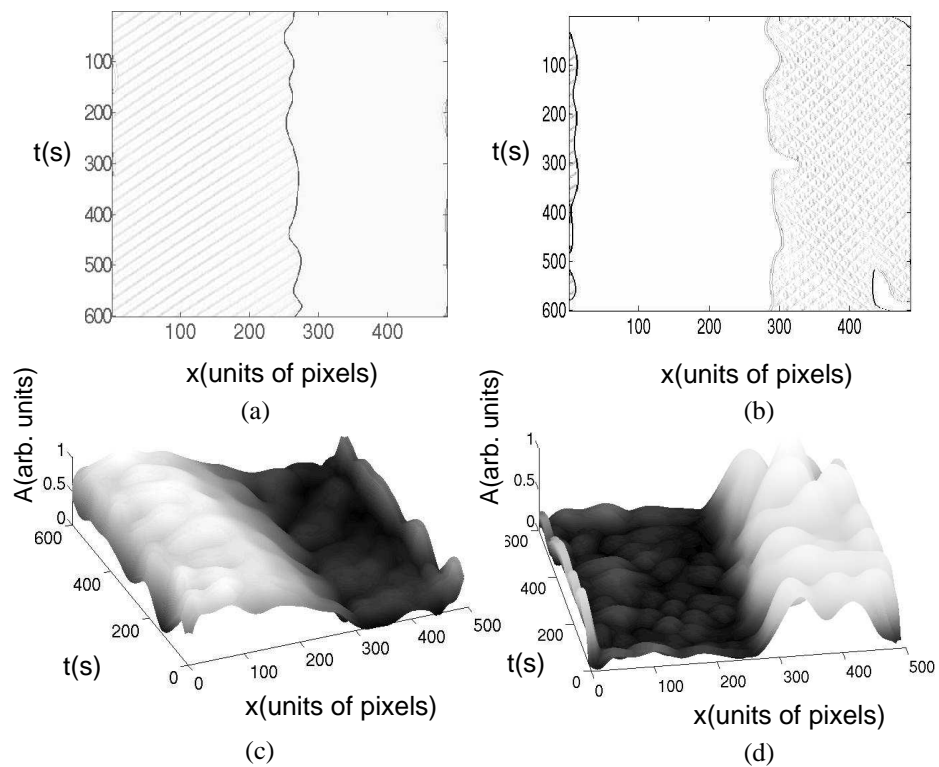


Figure 2.10: From a spatiotemporal diagram $S_{y_o}(x, t)$ at $d = 4$ mm and $\Delta T_v = 28$ K. Filtered domains: (a) TW domain; (b) ALT domain. Demodulated amplitudes: (c) of the left traveling mode A_{v-} ; (d) of the right traveling mode A_{v+} .

domain are connected by a 1D-front. From the corresponding demodulated images:

- In Fig. 2.10(a,b) we can see the 1D-fronts where we can measure the degree of fluctuation of the front, in (a) fluctuations are of the order of 14 mm, and in (b) 37 mm. Besides, we obtain the velocities of propagation $v_p \approx 0.0092$ mm/s in (a), and 0.0064 mm/s in (b). The binary matrix used to filter each domain allows us to quantify $\sigma_{inv} = 54.35$ % for the TW domain and $\sigma_{inv} = 37.42$ % for the ALT domain.
- In Fig. 2.10(c) for the TW domain we show how the amplitude smoothly decays in order to quantify the attenuation length ξ . Whereas, in Fig. 2.10(d), for the ALT domain the amplitude decays sharply, this is because we have selected M_{v+} as the critical mode representing the ALT domain. From Fig. 2.10(c) we obtain the attenuation length of the amplitude A_{v-} which is $\xi \approx 56$ mm, and from Fig. 2.10(d) the attenuation length of the amplitude A_{v+} is $\xi \approx 38$ mm.

2.6. Data analysis II: A network of convective coupled oscillators

In this section, we describe the discretization process developed on the spatiotemporal diagrams $S_{y_o}(x, t)$ in order to obtain discrete signals for each convective oscillator belonging to a lattice of 50 oscillators. For each one of these signals, the fundamental frequencies are filtered on the Fourier spectrum (in ω) with similar demodulation techniques than the ones described in the previous section. From the phases belonging to each oscillator (Ψ_i), the critical frequency (*cluster frequency*) is extracted by demodulation techniques. Our aim is to carry out a cross-correlation study of the oscillators phases in order to understand cooperative phenomena like spatiotemporal phase synchronization transitions.

2.6.1. Tracking the oscillators trajectories

Contrasted shadowgraphy images allow us to map the positions of hotspots over the heating line HL using the brightness profile (modulation of the brightest contour because of the effect of thermal lenses). We observe from Fig. 2.11(a) which corresponds to a photograph of the shadowgraphy image, and from Fig. 2.11(b) which is an instantaneous bright modulation along the array that: (i) extrema are equispaced; and (ii) between two consecutive minima there are one or two oscillators. In Fig. 2.11(b) we distinguish two characteristic scales: stationary for λ_s and oscillating for $2\lambda_s$. Therefore, the analysis of the spatiotemporal diagram $S_{y_o}(x, t)$ begins with the selection the implied relative extrema (at the starting time) which represent the oscillating units (the approximate size of each oscillator is of 6 mm). We choose the minima for convenience. Afterwards, we follow the involved absolute or relative minima along the temporal series $S_{y_o}(x, t)$, this is defined as the *tracking method*. For each i -oscillator we obtain the trajectory $X_i(t)$:

$$X_i(t) = x_i + a_i \cos[\Psi_i(\phi_i^{v_1}, \dots, \phi_i^{v_n}, \phi_i^c, \phi_i^o)]$$

where x_i is the zero position of oscillation, a_i is the amplitude of oscillation which remains inside equispaced intervals of 10 units of pixels, Ψ_i is the raw phase containing all the involved phases: $\phi_i^{v_j}$ for oscillating modes ($j = 1, \dots, n$), ϕ_i^c for critical modes (the ones which trigger the instability)

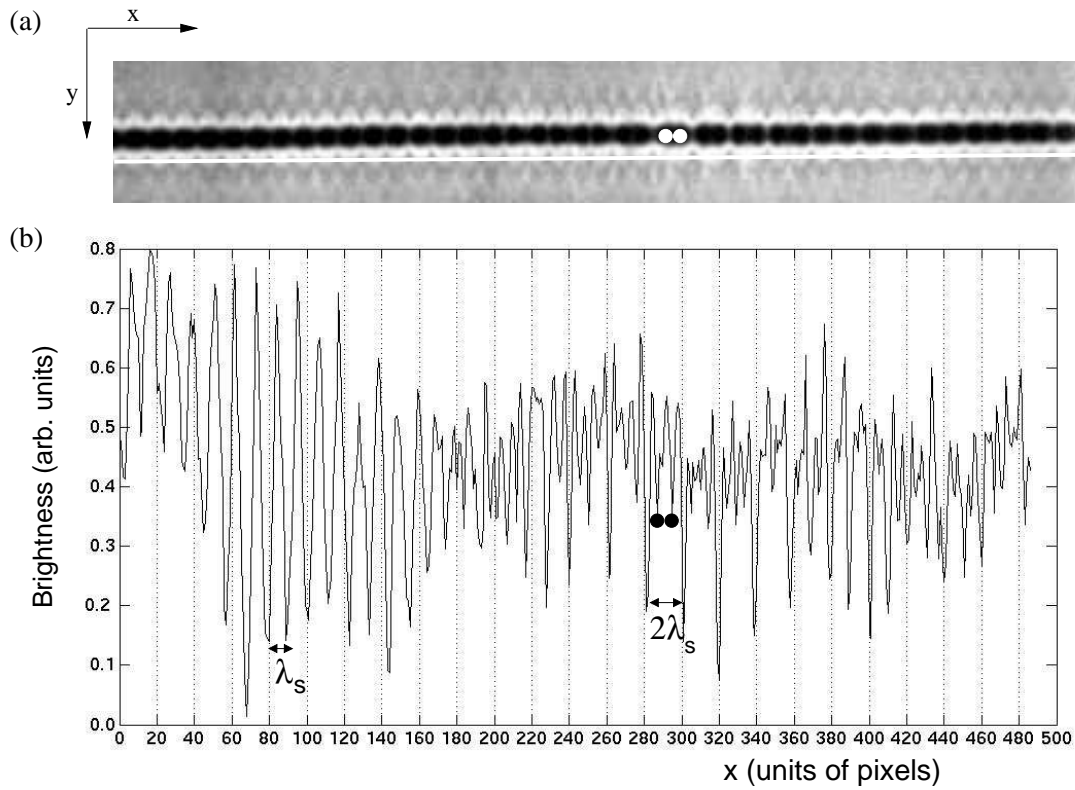


Figure 2.11: (a) Photograph of the shadowgraphy image of the patterned fluid layer on the screen. The white line represents the recording line, white circles represent two neighboring hotspots. (b) Instantaneous brightness profile of the same pattern in (a) where oscillators are equispaced at both λ_s and $2\lambda_s$. Black circles represent the corresponding hotspots highlighted in (a).

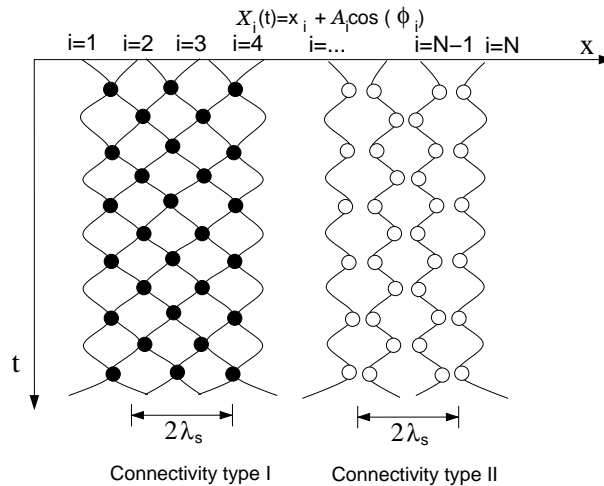


Figure 2.12: Sketch of a counteroscillating spatiotemporal pattern (antiphase pattern) of N -coupled oscillators. Each oscillator describes a trajectory $X_i(t) = x_i + a_i \cos[\Psi_i(\phi_i^{v_1}, \dots, \phi_i^{v_n}, \phi_i^c, \phi_i^o)]$. Two kinds of connectivity are distinguished: connectivity type I for overlapped positions, and connectivity type II when no contact is produced between oscillators.

and ϕ_i° is a constant phase shift. In Fig. 2.12 we have sketched the tracked information for the entire array of N -oscillators.

The dynamics represented in Fig. 2.12 belongs to the kind of counterphase oscillating hotspots. This is an antiphase state because of the attractive-repulsive coupling between oscillators. We deal with two main kinds of connectivity (Fig. 2.12) depending on whether oscillators collide with each other, this is defined as **connectivity type I**, or not, **connectivity type II**.

After decoding the global information from two different antiphase patterns $S_{y_o}(x, t)$, we obtain the tracking images shown in Fig. 2.13. In Fig. 2.13(a) synchronized i -oscillators (in one fundamental frequency) in between $0 < i < 25$ form two irregular domains, the first one collapses. Meanwhile, in Fig. 2.13(b) synchronized i -oscillators (in two fundamental frequencies) in between $26 < i < 38$ form a coherent and stationary domain. From this new discrete system, we perform demodulation techniques: using 1D-FFT and designing a suitable filter around the *critical frequency* ω_i^c , in order to obtain the frequency distribution ω_i^c along the array ($i = 1, \dots, N$). Because in this process we apply the demodulation technique at each oscillator, and the parameters of the filter are exclusively given by the synchronized i -oscillators (oscillating with ω_i^c), the frequency obtained for the desynchronized oscillators will remain outside of the variance Δ of the frequency of the synchronized ones. The frequency of synchronized oscillators will satisfy $|\omega_i^c - \omega_\Phi| \leq \Delta$, where ω_Φ is the frequency of the cluster and Δ is the frequency bandwidth for which phase locking is assured, this is a *condition of synchronization*. In Fig. 2.14 we show the frequency distribution along the array at the threshold of a phase synchronization, the frequency of the cluster ω_Φ is obtained averaging the critical frequencies of the oscillators belonging to the cluster.

From the tracking matrix, which follows the positions of each individual oscillator in time, we look for the interaction loci between neighboring oscillators (connectivity type I: attractive interaction with collision) in order to determine the time-varying topology, this topology is the result of antiphase oscillations. The interaction loci are the nonzero elements of a new matrix defined as **link matrix** L_{ij} . Thus, $L_{ij} = 1$ for positions satisfying $X_{i-1}(t) = X_i(t)$ and $L_{ij} = 0$ otherwise. The link matrix shows the wiring by contact in space and rewiring in time. In order to get rid of unreal contact interactions because of experimental noise, only the oscillators within a band of frequencies centered at the cluster frequency ω_Φ are selected by a previous filtering process using 1D-FFT. In Fig. 2.15(a) we show the link matrix, and in Fig. 2.15(b) the corresponding histogram showing the number of collisions for each oscillator.

Applying the statistical method of *running averages* (a temporal signal is averaged over temporal steps) on L_{ij} with the right choice of the temporal step, enables us to discover possible underlying relations between the connectivity and the dynamics of the global system, for example the amplitude modulations of the critical modes. So, the greater the number of links is the greater the spatial correlation is expected.

The *cross-correlation* is a statistical method that reveals the existence of spatiotemporal domains displaying the cluster frequency, and enables us to bound cluster domains. Correlation analysis is performed following the standard definition of cross-correlation between two time-dependent column vectors X_{ik}, X_{jk} of length $k = t_f$:

$$C_{ij}(X_{ik}, X_{jk}) = \langle X_{ik}, X_{jk} \rangle = \frac{\sum_{k=1}^{t_f} (X_{ik} - \bar{X}_{ik})(X_{jk} - \bar{X}_{jk})}{\sum_{k=1}^{t_f} (X_{ik} - \bar{X}_{ik})^2 \sum_{k=1}^{t_f} (X_{jk} - \bar{X}_{jk})^2} \quad (2.1)$$

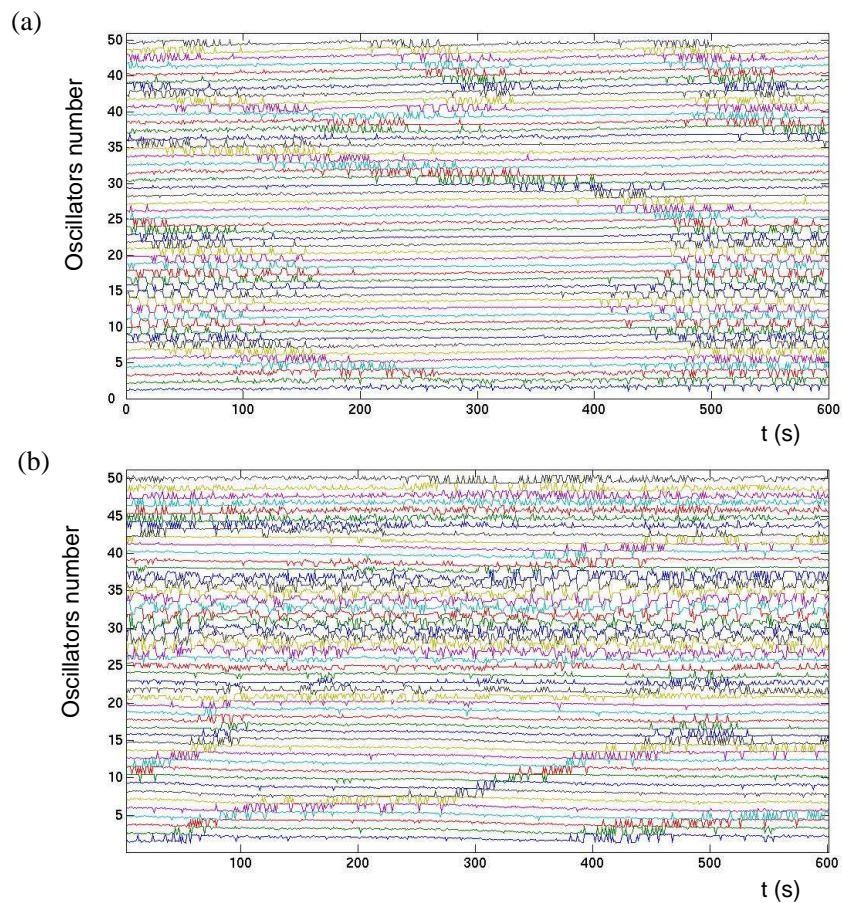


Figure 2.13: Two examples of spatiotemporal tracking for two different oscillatory dynamics: (a) synchronized i -oscillators ($0 < i < 25$) form irregular domains (at the beginning and at the end); (b) synchronized i -oscillators ($26 < i < 38$) form a coherent and stationary domain.

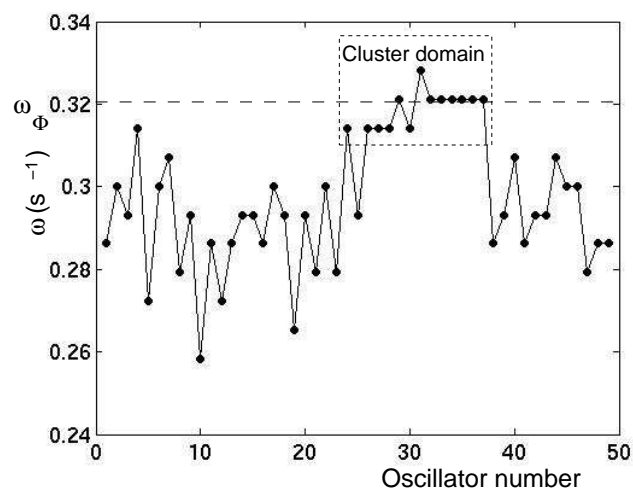


Figure 2.14: Critical frequencies along the oscillators array. The horizontal dashed line corresponds to the value of ω_ϕ which is the average of the critical frequencies inside the cluster domain.

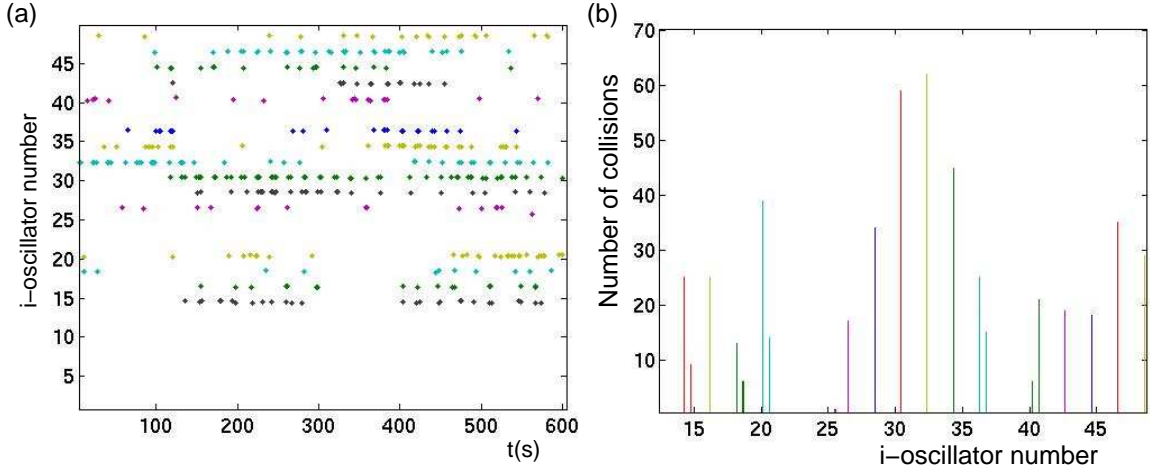


Figure 2.15: (a) The link matrix L_{ij} . (b) The corresponding histogram of (a), each bar length correspond to the number of collisions between adjacent oscillators.

It provides information about the degree of correlation at zero time lag. In order to extract the characteristic time lags between two time-dependent vectors, results in Chapter 4 are obtained using the matlab algorithm (“*xcorr*”) which yields a cross-correlation function of the time lags $\mathcal{C}_{ij}(\tau_l)$, where time lags τ_l vary from zero (maximum correlation) to $2t_f - 1$. The **cross-correlation vector** $\mathcal{C}_{ij}(\tau_l)$ is symmetric with respect to element $\tau_l = t_f$, which corresponds to our zero lag ($\tau_l = 0$). In order to compute phase mismatches we use the cosine function of the phases as it is explained in Chapter 4. Then, for each pair of synchronized oscillators, the corresponding vectors X_{ik}, X_{jk} are cosine functions. The envelope of the cross-correlation function $\mathcal{C}_{ij}(\tau_l)$ is expected to decay smoothly from $\tau_l = t_f$. Thus, the **correlation time** τ_c fulfills $|\mathcal{C}_{ij}(\tau_c)| = |\mathcal{C}_{ij}(\tau_l = t_f)|/e$.

By using cross-correlations, from the N -discrete signals of the oscillators, we are able to determine phase correlations between oscillators. If we study cross-correlations between N vectors (which are cosine functions of the phases), we build the **inphase matrix** \mathcal{I}_{ij} with dimensions $N \times N$. Each element is obtained from the maximum value of the cross-correlation function $\mathcal{C}_{ij}(\tau_l)$, then $\mathcal{I}_{ij} = \max \mathcal{C}_{ij}(\tau_l)$. Diagonal elements \mathcal{I}_{ij} represent self-correlations. Similarly, we build the **antiphase matrix** \mathcal{A}_{ij} with dimensions $N \times N$. Each element is obtained from the minimum value of the cross-correlation function $\mathcal{C}_{ij}(\tau_l)$, then $\mathcal{A}_{ij} = \min \mathcal{C}_{ij}(\tau_l)$. Diagonal elements \mathcal{A}_{ii} represent self-correlations.

Chapter 3

Characterization of instabilities in an extended 1D convective system

In this chapter we present the study of spatiotemporal patterns that appear in the out-of-equilibrium dynamics of a 1D system. This system consists of a rectangular layer of fluid which is locally heated along a line beneath its free surface. The Bénard-Marangoni convection accounts for the different dynamics depending on two control parameters: the depth of the fluid layer d and the vertical temperature difference ΔT_v . It is a spatially extended system consisting of approximately 75 convective cells which will be driven far away from the first instability towards weak turbulence (spatiotemporal chaos). In contrast to the continuous system studied in this chapter, a different view will be given in Chapter 4 for a discrete network of 50-oscillators.

In 1970 Krishnamurti showed in an experimental work on convective fluid layers for different silicone oils that fluids with $Pr \geq \mathcal{O}(10)$ [124] exhibit a great diversity of steady patterns in the route towards turbulence, and that these patterns occupy large regions on the parameter space. Our convective fluid layer of silicone oil with a high Prandtl number ($Pr \approx 75$) exhibits about eight different regimes in the explored space of the control parameters ($d, \Delta T_v$) including bistable regimes. Non-bistable regimes and propagative pulses had already been characterized on a similar cell by Burguete [79, 111]; besides it was found that controlling the horizontal temperature difference ΔT_h , the stability diagram $(\Delta T_v, \Delta T_h, d)$ was qualitative the same. The novelty of the present work is to characterize the nature of bifurcations (close to the onset) choosing the right order parameters.

For deep layers the basic homogeneous pattern which consists of two counter-rotative rolls bifurcates supercritically towards a traveling wave pattern, this type of transition has been widely explored in other systems (i.e. lateral heating, binary fluids, crystal growth). Consequently, our main priority is to characterize the successive secondary instabilities that take place at lower depths from a basic cellular pattern. Depending on the depth, the cellular pattern may undergo two different kinds of subcritical transitions which always involve bistability and hence, the presence of 1D-fronts. For every fixed depth at the maximum ΔT_v , a defect-like dynamics arises. We consider this pattern to be the last step of a weak developed turbulence.

For shallow layers, particular attention is given to a clustering process towards a spatiotemporal beating phenomenon which is the result of a spatiotemporal splitting of the traveling modes. To our best knowledge, this is the first evidence in hydrodynamics of such a process. Far from

primary instabilities, every secondary instability is a phase-like synchronization transition with global and absolute character which can be described from the modulus of the amplitudes of the critical modes close to the threshold.

3.1. Introduction

Our convective layer is a dissipative and “ideal” quasi-1D extended system that undergoes a sequence of secondary instabilities from the basic cellular pattern with wave number k_s for intermediate and shallow layers. Choosing a suitable order parameter, for example the amplitude of the critical modes, we characterize the nature of these instabilities and we find out that these instabilities are oscillatory, the kind of oscillatory Hopf bifurcations (plane phase diagrams correspond to limit cycles) that arise from a stationary pattern.

In 1D cellular systems, Couillet and Ioss [16] (CI) classified the global character of secondary bifurcations using a Bloch-Floquet analysis [125] and predicted ten generic secondary instabilities. This theory, taking into account the coupling between the phase of the basic pattern and the amplitude of the unstable modes associated to the secondary bifurcation, predicts a doubling wave length pattern with $k_s/2$ ($\equiv k_{s/2}$).

Later on, Gil found localized solutions like solitons, breathers and amplitude holes using phase-amplitude coupled equations with less restrictive symmetry arguments [19] in 1D cellular systems. Previously, he had also obtained localized solutions implementing the Swift-Hohenberg equation [18]. Simulations with this type of equations, like with the nonlinear Schrödinger equation [126], obtain localized solutions in cellular patterns emulating wave propagation in crystal lattices. This point of view coming from solid state physics provides good qualitative results.

In subcritical transitions, the presence of localized drifting domains has been tackled theoretically by Goldstein [17]. This theory enables us to explain the presence of drifting domains of broken parity, such as our kind of “subcritical” traveling waves, but in the framework of a doubling wave length bifurcation.

For a supercritical model it has been proved that the “convective” critical control parameter for a confined system verifies $\varepsilon_c = \varepsilon_a + \mathcal{O}(L_x^{-2})$, where ε_a is the “absolute” critical control parameter of the corresponding extended system [127], so for $d \geq 4.5$ mm the approximation $\varepsilon_c \approx \varepsilon_a$ is valid.

Similar 1D convective systems reporting oscillatory patterns are found in Refs. [50, 80–82, 84–86, 128]. Other 1D and 2D systems displaying similar dynamics (stationary cellular patterns and oscillatory patterns) are cited in Chapter 1.

3.2. An extended 1D convective system

In our fluid layer, thermo-buoyant-capillary instabilities are driven by Bénard-Marangoni mechanisms (see a more detailed explanation in Chapter 1), which are the result of the combination between Archimedean forces (Rayleigh-Bénard convection) and surface tensions (Marangoni convection). When the dynamic Bond number is $Bo_D = 1$ (this happens for a depth of $d = 2.92$ mm) both forces are comparatively equal. Our research is focused on every instability the system comes through and in consequence, on every 1D pattern at the onset and further beyond. Non-homogeneous patterns, like the aforementioned stationary cellular pattern or the traveling

wave pattern, are the dynamical solutions of an unbounded 1D-array of 52 convective cells, which correspond to the central region of observation from a complete 1D-array of 75 convective cells. Each convective cell arises from microscopic thermal fluctuations in the bulk of the fluid layer, in fact, a coarse-graining mechanism is naturally performed. Because the physical aspect ratios in the cellular range $d = [3, 4]$ mm are within $\Gamma_\lambda = L_x/\lambda_s = [75, 59]$, we might consider that this 1D-array is not being affected by the boundary conditions at the extremes, in \hat{x} , hence we are dealing with a spatially extended system.

Without threshold, as soon as $\Delta T_v \neq 0$, a homogeneous convective pattern (PC) appears: the fluid over the heater line (HL) raises by the effect of a negative vertical temperature gradient and it returns down near the cooling walls. Therefore, a circulating flow at both sides of HL develops the structure of two counter-rotative rolls whose axis are parallel to the HL. For the subsequent instabilities, at any value of the control parameter ΔT_v , the PC pattern will invariably remain.

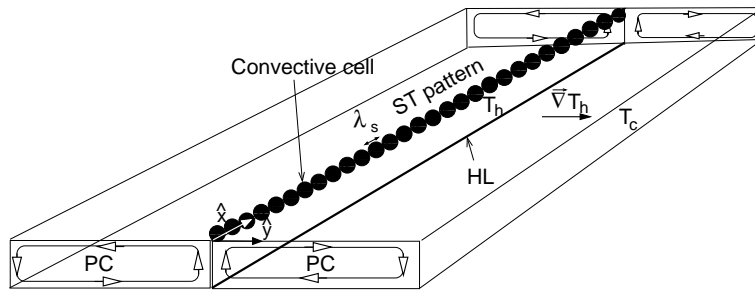


Figure 3.1: Sketch of the stationary cellular ST pattern (with wave length λ_s) over the heating line (HL), PC designates the two counter-rotating rolls of the primary convection. T_h is the temperature at HL, T_c is the temperature at the cooling walls, and $\vec{\nabla}T_h$ is the horizontal temperature gradient.

The PC pattern can be driven, increasing ΔT_v , to two different kinds of *primary bifurcations* depending on the depth of the fluid layer d in between 2.5 and 5 mm:

- For $d \leq 3.5$ mm: as soon as $\Delta T_v \neq 0$ a stationary cellular pattern (ST) with wave number k_s becomes unstable. This quasi-1D pattern belongs to the type of stationary rolls predicted by Smith & Davis [58] with a wavevector perpendicular to the horizontal temperature gradient (see Fig. 3.1).
- For $d \geq 4.5$ mm: a traveling wave pattern (TW) becomes unstable from the PC pattern. This bifurcation happens to be supercritical, hence the whole ensemble of oscillators cooperatively decide to travel towards a privileged direction. For this supercritical bifurcation the correlation length is supposed to diverge without the presence of any front. This bifurcation is an oscillatory supercritical Hopf bifurcation that might be theoretically described by the cubic complex Ginzburg-Landau equation. Experimentally, this kind of supercritical bifurcation is found in many other extended systems [29, 86] and references therein. For lower depths, according to the experimental results which are shown below, the TW pattern bifurcates subcritically from the ST pattern.

For higher values of ΔT_v , a new possible oscillatory instability still remains involving the presence of two counter-propagative waves. This new regime appears beyond both primary instabili-

ties, it is a resonant triad termed alternating pattern (ALT). It consists of two counter-propagative waves with wave numbers $k_s/2$ overlapping the ST pattern. Patterns, up to this point, had already been identified in a previous work [79] but differing in the magnitudes characterizing the TW pattern (with a doubling-wave length). Probably, as it was expected, the improvement of accuracy by means of an optimized optical system, a different experimental cell and a different data acquisition system have contributed to a better knowledge. Nevertheless, we show that the ALT pattern belongs to the type of spatial period-doubling oscillatory bifurcation in agreement with the CI theory. Buoyancy plumes can be observed in the shadowgraphy image of the ALT pattern in Fig. 3.2, these plumes are detached along the perpendicular axis to HL when a pair of hotspots collide.

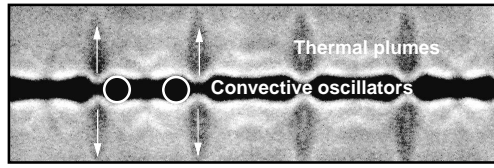


Figure 3.2: Zoomed image on the screen of the oscillatory ALT pattern: two counter-propagative waves overlapping the stationary cellular pattern. Dark convective cells or hotspots (white superimposed circumferences) are observed over the heating line at the center and dark thermal plumes (white arrows) are localized every two neighboring convective cells and detached outwards.

3.3. The Fourier spectra of asymptotic patterns

The spatiotemporal diagrams $S_{y_o}(x, t)$ and the bidimensional Fourier spectra of the introduced patterns ST, TW and ALT are shown in Fig. 3.3. The fundamental modes of each pattern are: the stationary mode $M_s(k_s, 0)$ for the ST pattern, one of the two possible traveling modes [right(+) or left(-)] $M_{v\pm}(k_v, \pm\omega_v)$, and for the ALT pattern the triad: $M_s(k_s, 0)$, $M_{v\pm}(k_v, \pm\omega_v)$ ¹.

In a sequence of measurements, varying smoothly the control parameter ΔT_v , from the Fourier spectra:

- *In the TW pattern* [Fig. 3.3(b)] we obtain a mean period of approximately 25 s. The phase velocity $v_\phi = \omega_v/k_v$ increases monotonically with ΔT_v . We have measured that the linear group velocity verifies $v_g = d\omega/dk \approx 0$, as it will be shown later on from a transient regime.
- *In the ALT pattern* [Fig. 3.3(c)] we obtain a mean period about 23 s. However, for an ascending sequence the phase velocity keeps constant. This pattern is strongly nonlinear as the result of the competition between the fundamental modes of a resonant triad and their harmonics [see Fig. 3.3(c.2)]. In our system, differing from other convective experiments, nonlinear interactions between the two counter-propagative modes restore the stationary mode. These nonlinear interactions, under subcritical conditions, drive the system to exhibit localized domains in the ALT pattern coexisting with the cellular ST pattern, this mixed

¹Strictly speaking, as we show in a later section, for the TW pattern $k_v = k_{2s/3}$ and for the ALT pattern $k_v = k_s/2$, but on the following graphs we use the same symbol $M_{v\pm}$ to show the evolution of the propagative wave numbers, k_v . The reason comes from the technique of localization, in a surrounding area on the bidimensional Fourier spectra, of peaks belonging to propagative modes.

pattern is termed ST/ALT [Fig. 3.3(d)]. These domains in ALT may collapse when they have fluctuating boundaries. In Fig. 3.3(d.2) we may observe that the coupling between oscillatory modes in the ST/ALT pattern is weaker than in Fig. 3.3(c.2). Most of the research reported in this chapter is devoted to the study of bistable regimes, like the mixed ST/ALT pattern, where two different solutions share the same control parameters. Coexistence necessarily implies the study of boundaries or 1D-fronts.

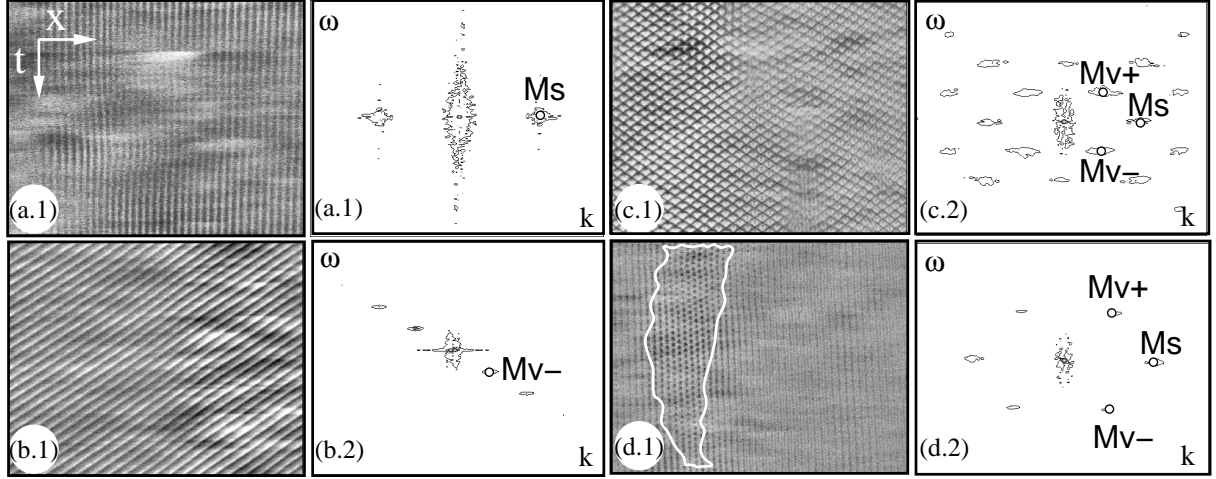


Figure 3.3: Spatiotemporal diagrams $S_{y_o}(x, t)$ and the bidimensional Fourier spectra for: (a) the ST pattern at ($d = 3$ mm, $\Delta T_v = 16.7$ K); (b) the TW pattern at ($d = 4$ mm, $\Delta T_v = 18.6$ K); (c) the ALT pattern at ($d = 4$ mm, $\Delta T_v = 25$ K); (d) the mixed ST/ALT pattern at ($d = 3$ mm, $\Delta T_v = 30$ K). The boundary of the localized pattern ALT has been highlighted (filtering with $\mu = 1/e$). The fundamental modes are: the stationary mode M_s , the traveling modes $M_{v\pm}$ (TW) and $M_{v\pm}$ (ALT). The central spot corresponds to the central peak ($k = 0, \omega = 0$).

3.4. Dynamics of the convective cells: breaking the symmetries

As the system is driven far from the primary instability more symmetries are lost from the original patterns (from a homogeneous pattern or from a stationary cellular pattern). This fact is easily observed from the convective cells shown in Fig. 3.4, they are observed along HL because of the shadowgraphy technique and arise from the microscopic thermal interactions. Rays emerging from the layer converge on the screen at the bright modulations, while diverging rays due to the ascending convective flow form an array of dark spots, which we call hotspots (a more detailed description of the shadowgraphy technique is found in Chapter 2). This is the so-called effect of thermal lenses.

In this array of coupled oscillators there may exist localized discontinuities that correspond to 1D-fronts. These fronts on the spatiotemporal diagram $S_{y_o}(x, t)$ bound localized domains. Two different kinds of **localized domains** can be distinguishing regarding the wave length of the oscillations:

- (i) **Localized ALT domains**, with wave length λ_{2s} , in the mixed ST/ALT pattern.

- (ii) **Localized ZZ domains** (zig-zag domains), with a slightly shifted wave length $\lambda_{2s} - \delta\lambda$, in the ST/ZZ pattern [Fig. 3.4(d)].

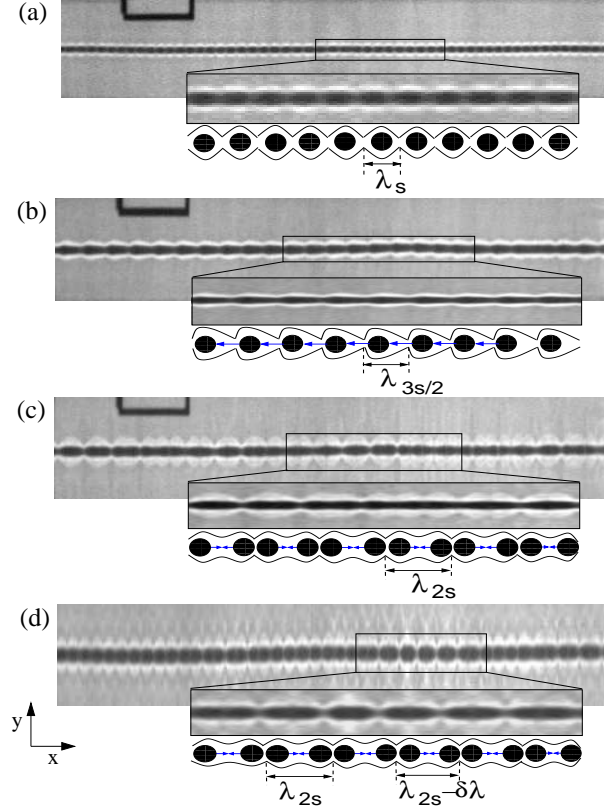


Figure 3.4: Pictures on the screen and a zoom view of the selected area for: (a) the ST pattern at $d = 3$ mm; (b) the TW pattern at $d = 4$ mm; (c) the ALT pattern at $d = 4$ mm; (d) the ST/ZZ pattern at $d = 3$ mm. Below, a sketch of the dynamics of hotspots over HL. The arrows between hotspots indicate the direction of their movement. Scales between pictures are not maintained.

In Fig. 3.4, we have sketched below the shadowgraphy images: (i) how the dynamics of the array of convective cells is observed over HL, and (ii) how the contours of maximum brightness reveal the spatial symmetries.

Instabilities always break certain spatial and/or temporal symmetries, this fact yields a different description of patterns:

- In the homogeneous PC pattern, the continuous spatial translation symmetry is broken into a stationary cellular ST pattern. This new pattern has a discrete translation symmetry on space (\hat{x}) given by λ_s and a continuous one on time.
- The TW pattern has a discrete spatial translation symmetry given by $\lambda_{3s/2}$, besides it breaks the parity symmetry ($x \rightarrow -x$) and the temporal continuous translation symmetry. Convective oscillators take the position of their neighbors along one direction with frequency ω_v .
- The ALT pattern has a discrete spatial translation symmetry given by λ_{2s} . Convective oscillators collide by pairs, recovering their initial positions after a cycle of frequency ω_v .

- The ZZ pattern has two discrete spatial translation symmetries given by λ_{2s} and $\lambda_z = \lambda_{2s} - \delta\lambda$. Convective oscillators collide by pairs with two close frequencies: ω_v and ω_z .

3.5. The stability diagram

Subsequent *secondary bifurcations* for different depths, in the explored range $d = [2.5, 5]$ mm, allow to build the following itineraries to weak turbulence as we increase ΔT_v (see the stability diagram in Fig: 3.5 and the Table 3.1):

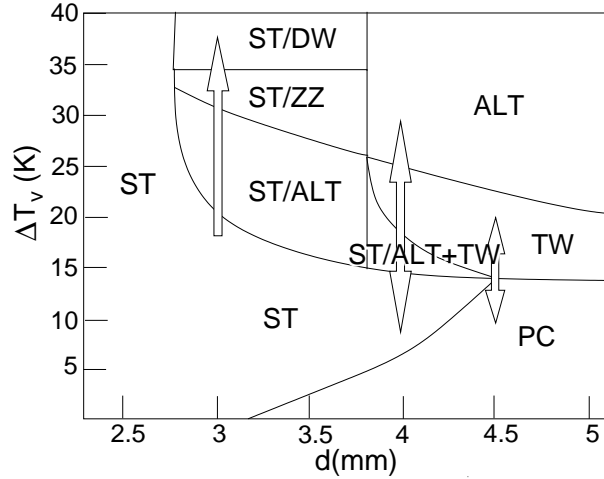


Figure 3.5: Stability diagram. Solid lines bound regions with the same asymptotic dynamics. The upward arrow corresponds to ascending sequences of measurements and two-sided arrows correspond to hysteresis cycle measurements. Stationary patterns are: PC (primary convection) and ST (cellular pattern). Oscillatory patterns are: ST/ALT (mixed pattern with irregular clusters), ST/ZZ (spatiotemporal beating regime with stationary clusters), ST/DW (temporal beating regime) and TW (traveling waves). ST/ALT+TW corresponds to the coexistence of the mixed ST/ALT pattern with the TW pattern.

- (i) **Deep layers:** For $4.5 \leq d \leq 5$ mm and further from the threshold of the primary bifurcation to TW, the system undergoes a new bifurcation to the ALT pattern. The relative amplitudes in the ALT pattern verify $|A_{v-}| \approx |A_{v+}|$ and $|A_s| \approx |A_{v\pm}|/2$.
- (ii) **Intermediate layers:** For $4 \leq d \leq 4.5$ mm the system becomes unstable from ST to TW via a bistable regime. This bistable regime consists of a mixed ST/ALT pattern that coexists with the new unstable TW pattern. The front connecting these two regimes (ST/ALT and TW) is stationary because we have measured a zero front velocity ($v_p \approx 0.01$ mm/s). Beyond the bistable pattern, the TW pattern bifurcates towards the ALT pattern. For higher values of the control parameter ΔT_v , the ALT pattern has a dynamics of defects [Fig. 3.6(a,b)]. On the phase gradient diagram in Fig. 3.6(c) we can observe how these defects are spontaneously generated, adjusting locally the wave number of the pattern.
- (iii) **Shallow layers:** For $d \leq 3$ mm, from the basic ST pattern, the system becomes unstable successively towards:

Table 3.1: Asymptotic regimes from secondary instabilities in a 1D-array of coupled convective cells.

Stationary pattern (ST)	1 mode: $M_s(k_s, 0)$
Traveling waves (TW)	1 mode: $M_{v\pm}(k_v, \pm\omega_v)$
Mixed pattern (ST/ALT)	3 modes: $M_s(k_s, 0)$, $M_{v\pm}(k_v, \pm\omega_v)$
Spatiotemporal beats (ST/ZZ)	5 modes: $M_s(k_s, 0)$, $M_{v\pm}(k_v, \pm\omega_v)$, $M_{z\pm}(k_z, \pm\omega_z)$
Temporal beats (ST/DW)	5 modes: $M_s(k_s, 0)$, $M_{v\pm}(k_v, \pm\omega_v)$, $M_{w\pm}(k_w, \pm\omega_w)$

1. The **ST/ALT** pattern for which irregular domains in the oscillatory ALT pattern grow or collapse (also termed breathing 1D-fronts).
2. The **ST/ZZ** pattern for which the spatiotemporal splitting of the traveling modes is produced in one or two domains with high spatiotemporal coherence.
3. The **ST/DW** pattern (its designation comes from “double (D) frequency (W)”) for which a temporal splitting of the traveling modes still remains above the ST/ZZ regime, however there is not any spatial splitting. In this ST/DW pattern, a unique and wider domain in DW exists whose 1D-fronts, as we increase ΔT_v , convert into a chain of dislocations [see Fig. 3.7(a,b)]. In addition, there is a drifting of the stationary mode the same way it has been observed in other convective systems for high values of the control parameter [129].

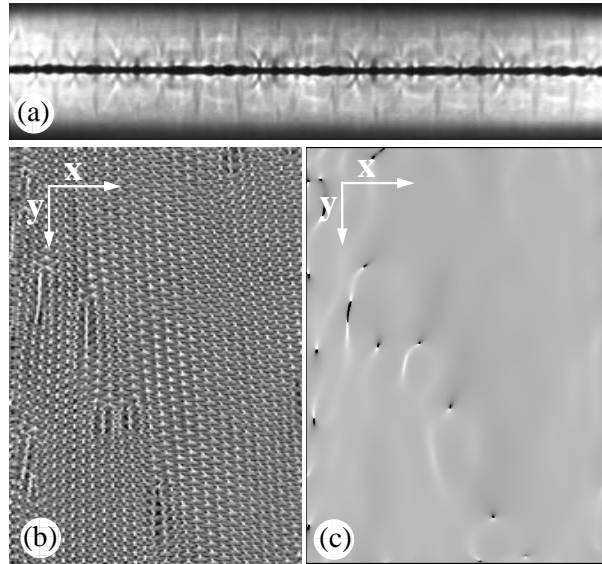


Figure 3.6: ALT pattern with the presence of defects at $d = 5$ mm and $\Delta T_v = 62$ K: (a) the shadowgraphy image on the screen; (b) the spatiotemporal diagram; (c) phase gradient of the stationary mode M_s , discontinuities correspond to dislocations.

For thinner layers $d \leq 2.5$ mm and $\Delta T_v \geq 55$ K, a classical Bénard-Marangoni convection appears for which the hexagonal cells are arranged symmetrically with respect to HL.

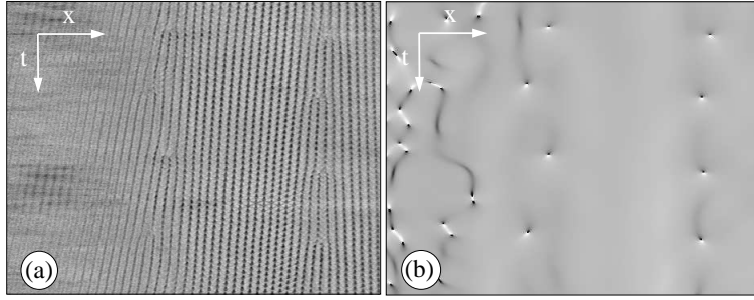


Figure 3.7: (a) Spatiotemporal diagram $S_{y_o}(x, t)$ at $d = 3$ mm and $\Delta T_v = 42$ K; (b) the corresponding diagram for the phase gradient of the mode M_s . Spatiotemporal grain boundaries are observed as chains of dislocations.

For intermediate layers at $d = 4$ and 4.5 mm (see the stability diagram in Fig. 3.5), we show in the following section that, as we get closer to the codimension-2 point ($d = 4.5$ mm, $\Delta T_v = 14$ K) the subcritical behavior of the system is expected to become weaker. At this critical point the system bifurcates to TW in two possible ways, depending on the history (the chosen trajectory in the phase space): from the homogeneous PC pattern or from the cellular ST pattern. From $d \approx 4.5$ mm the threshold from the PC towards the ST pattern gradually decreases until $d \approx 3$ mm, where the ST pattern appears without threshold. This experimental result is in agreement with the theoretical prediction (a linear stability analysis) for a similar experimental setup [130] that shows that, as far as the Gaussian profile of the temperature field flattens a smaller threshold for the ST pattern is expected. Above (for $d \geq 4.5$ mm) the system undergoes a supercritical bifurcation towards TW [see the sketch in Fig. 3.8(a)].

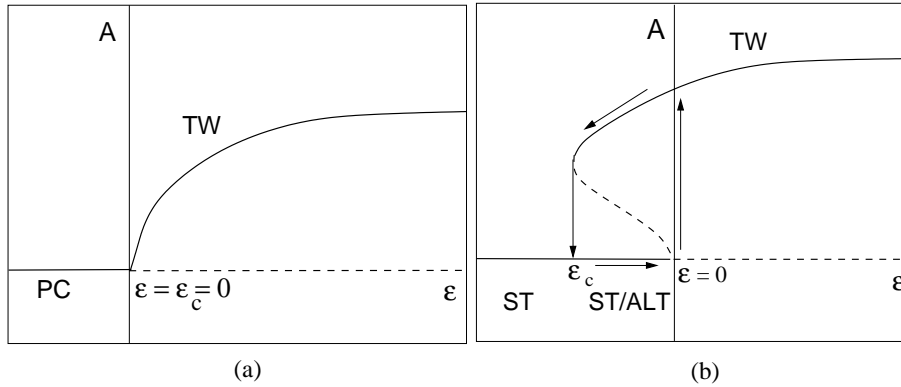


Figure 3.8: Sketch of the bifurcation diagram for: (a) a supercritical bifurcation to TW; (b) a subcritical bifurcation to TW.

3.6. Dynamics in intermediate layers: Subcritical bifurcation to traveling waves and further

In order to characterize the subcritical nature of the secondary bifurcation to TW at intermediate layers ($4 \leq d \leq 4.5$ mm), we are going to look for a hysteresis cycle studying the modulus

of the amplitudes of the fundamental modes [see Fig. 3.9(a) for $d = 4$ mm]. We define the control parameter ε , which is obtained from the *forward transition*, and the critical control parameter $-\varepsilon_c$, which is obtained from the *reverse transition*. Our aim is to determine the subcritical interval ($-\varepsilon_c \leq \varepsilon \leq 0$) where the bistable regime consists of the mixed ST/ALT pattern coexisting with the TW pattern (ST/ALT+TW) [see the sketch in Fig. 3.8(b)].

In an ascending sequence of measurements (forward transition), when the system approaches the threshold of the TW pattern from the cellular ST pattern, we define the reduced control parameter $\varepsilon = \Delta T_v / \Delta T_{vc}^a - 1$, where ΔT_{vc}^a is the critical parameter. In Fig. 3.9(a) we show how the amplitude of the critical mode $|A_{v-}|$ grows sharply at this point, meanwhile the amplitudes $|A_s|$ and $|A_{v+}|$ decay to zero. The subcritical parameter of the hysteresis cycle is given by $\varepsilon_c = \Delta T_{vc}^d / \Delta T_{vc}^a - 1 < 0$, where ΔT_{vc}^d is the critical parameter obtained from the descending sequence (reverse transition) at which the system returns to the original ST pattern.

In order to figure out how this transition is produced, in Fig. 3.10 we show a correlative ascending sequence for the secondary bifurcation to TW at $d = 4$ mm from the ST/ALT pattern:

- For $\varepsilon_c \leq \varepsilon \leq 0$ the mixed ST/ALT pattern emerges. The wave length of the stationary mode is calculated from Fig. 3.11(a), $\lambda_s \approx 8.67 \pm 0.18$ mm. In the localized domains of the ALT pattern the competition between the traveling modes with similar amplitudes, produce a resonant nonlinear interaction with the stationary mode $M_s(k_s, 0)$. From Fig. 3.11(a) we obtain the wave numbers of the mixed ST/ALT pattern with $k_{s/2}$, and of the TW pattern with $k_{2s/3}$. We notice that the propagative modes of the mixed ST/ALT pattern are selected by the system before the TW modes play a destabilizing role. This nonlinear interaction is sketched in Fig. 3.12. Attending to the first nonlinear resonant criterion, a resonant interaction cannot be triggered between the stationary and the traveling modes. On the other hand, in Fig. 3.12 we show that although frequencies in the subcritical interval are roughly the same for the oscillatory modes with different wave numbers $k_{2s/3}$ and $k_{s/2}$ (this frequency is termed ω_{sr} in Fig. 3.12), close to the subcritical parameter $-\varepsilon_c$ the stationary mode $M_s(k_s, 0)$ activates only the resonant ALT modes $M_{v\pm}(k_{s/2}, \omega_{sr})$.
- For $\varepsilon = 0$ the system bifurcates towards the TW pattern at the same time that coexists with the original ST/ALT pattern, this is a bistable regime. In this regime, a discontinuity of the amplitude of the traveling mode $M_{v-}(k_{2s/3}, -\omega_v)$ has been produced in the corresponding domain, the TW pattern. The front velocity is approximately zero $v_p \approx 0.01$ mm/s. However, we have observed this bistable pattern for positive and small values of ε because our measurements are restricted by the size of the step.
- For $\varepsilon > 0$ the whole system has bifurcated to the TW pattern without the presence of boundaries, neither sources nor sinks, so $M_{v-}(k_{2s/3}, -\omega_v)$ is a global unstable mode.

At $d = 4$ mm, in the forward transition with a step of 0.5 K [see Fig. 3.9(a)] we obtain that a discontinuous jump of $|A_{v-}|$ is produced at $\Delta T_{vc}^a = 17.7$ K. To verify the existence of hysteresis we have worked with two new sequences, an upward and a reverse transition, with smaller a step of 0.3 K [see Fig. 3.9(b-c)]. From these measurements, we have obtained $\Delta T_{vc}^a = 16.4$ K and $\varepsilon_c = -0.07$. Close to the codimension-2 point (at $d = 4.5$ mm) following a hysteresis cycle with step 0.3 K, we have determined a narrower subcritical interval with $\varepsilon_c = -0.02$. If we compare the two upward transitions, with different steps 0.5 K [Fig. 3.9(a)] and 0.3 K [Fig. 3.9(b)], we

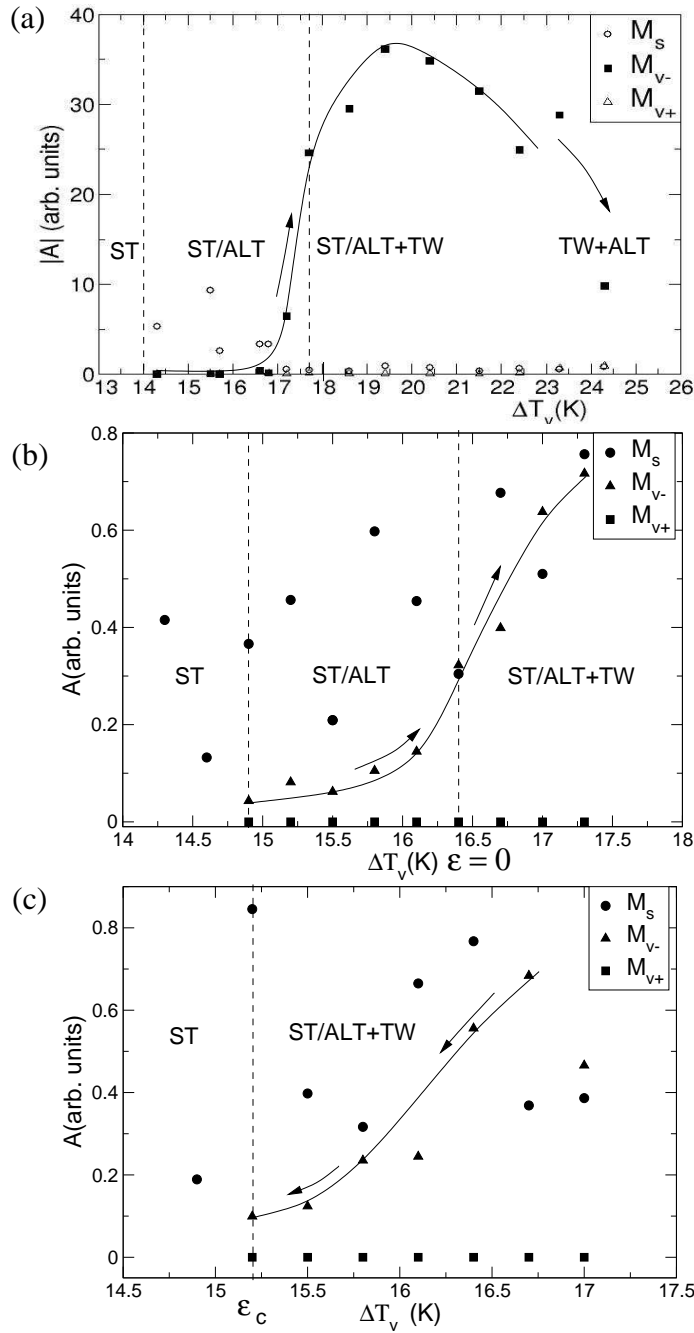


Figure 3.9: (a) Bifurcation diagram at $d = 4$ mm with ascending steps of 0.5 K. Far from this threshold at $\Delta T_v \approx 19.2$ K the amplitude of the mode M_{v-} decays in favor of the counter-propagative mode M_{v+} representing the advance of the front that splits the patterns TW and ALT; (b) upward bifurcation diagram at $d = 4$ mm with ascending steps of 0.3 K; (c) reverse bifurcation diagram at $d = 4$ mm with descending steps of 0.3 K. Solid lines are a guide to the eye. Dashed lines split different regimes. Arrows show the upward/reverse directions of the transitions.

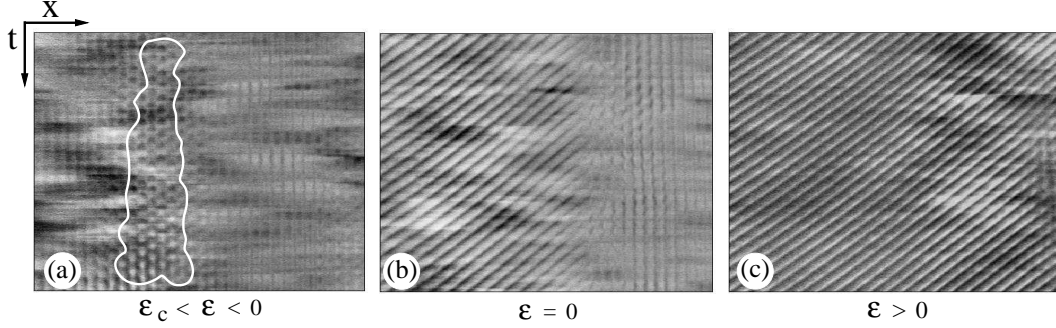


Figure 3.10: Spatiotemporal diagrams corresponding to the secondary bifurcation to TW at $d = 4$ mm (for an ascending sequence): (a) the mixed ST/ALT pattern belongs to the subcritical interval, the boundary of the ALT domain has been highlighted (filtering with $\mu = 0.5$); (b) the bistable pattern ST/ALT+TW at the threshold, these patterns are connected by a stationary front; (c) the TW pattern above the threshold.

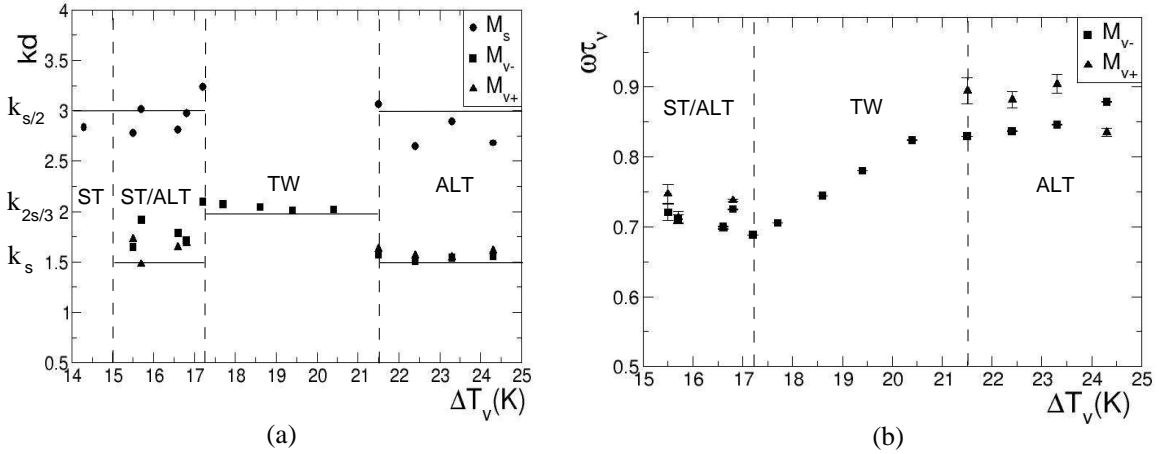


Figure 3.11: At $d = 4$ mm evolution vs ΔT_v (with step $|\Delta T_v| = 0.5$ K) of: (a) the dimensionless wave numbers (horizontal solid lines correspond to the average wave numbers); and (b) the dimensionless frequencies ($\tau_v = d^2/\nu = 3.2$ s) for each involved fundamental mode: M_s (stationary mode), $M_{v\pm}$ (right-left traveling modes). Vertical dashed lines separate different patterns.

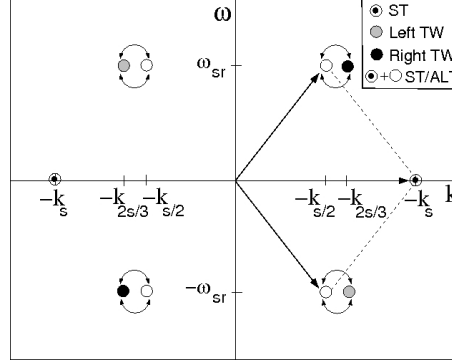


Figure 3.12: Sketch of the mechanism of activation of the resonant triad in the ALT domains (mixed ST/ALT pattern) induced by the emerging TW modes. The frequency at the subcritical interval ($-\varepsilon_c \leq \varepsilon \leq 0$) is ω_{sr} .

find out that the discontinuous jump of the amplitude $|A_{v-}|$ is produced before with the smaller step at $\Delta T_{vc}^a = 16.3$ K ($\Delta T_{vc}^a = 17.7$ K with step 0.5 K). This fact may suggest that, even for smaller steps we could measure a lower value of ΔT_{vc}^a , however we have shown that the subcritical interval increases the smaller the depth is (see the stability diagram in Fig. 3.5). On the other hand, at $d = 4$ mm the finite jump of wave numbers and frequencies is produced at $\Delta T_{vc}^a = 17.2$ K [Fig. 3.11(a,b)] before the jump of the amplitude of the mode M_{v-} at $\Delta T_{vc}^a = 17.7$ K [Fig. 3.9(a)] for an ascending sequence (with step 0.5 K).

On the other hand, from Fig. 3.11(a), in the mixed ST/ALT pattern, we have measured a finite jump of wave lengths of the propagative modes (of the order $\delta k \cdot d \approx 0.25$) that in comparison with the average values in the ALT pattern, is considered to be smaller than the experimental error. From Fig. 3.11(b) we infer that the phase velocity keeps constant in the ST/ALT regime and increases monotonically in the TW regime, until the system reaches the stronger nonlinear ALT regime.

If we evaluate the amplitudes of the propagative modes for the subsequent transition to the ALT pattern (from the TW pattern) we find an upward jump (this result will be shown in a later section), this fact and the existence of 1D-fronts connecting ALT and TW domains provides strong arguments to consider this bifurcation to be subcritical. 1D-Fronts belonging to these subcritical regimes are also reported in a later section.

3.7. Dynamics in shallow layers: Overview of a clustering process

In this section we focus on the dynamics at $d = 3$ mm where the basic stationary ST pattern with $\lambda_s \approx 6.81 \pm 0.07$ mm [from Fig. 3.13(a)] never loses stability against the emerging unstable traveling modes. For this reason new unstable domains coexist with the ST pattern. According to the weakly nonlinear coupling revealed from the Fourier spectra [see Fig. 3.14(c)], we infer that inside the fluctuating 1D-fronts the two counter-propagative modes $M_{v\pm}(k_v, \pm\omega_v)$ locally destabilize the basic ST pattern, triggering the resonant triad of the ALT regime. As we increase the control parameter ΔT_v , an interesting route to weak turbulence appears (see the stability diagram in Fig. 3.5). Because we have not observed any hysteresis behavior in this route we only

measure upward transitions. This route consists of the following three subsequent instabilities towards:

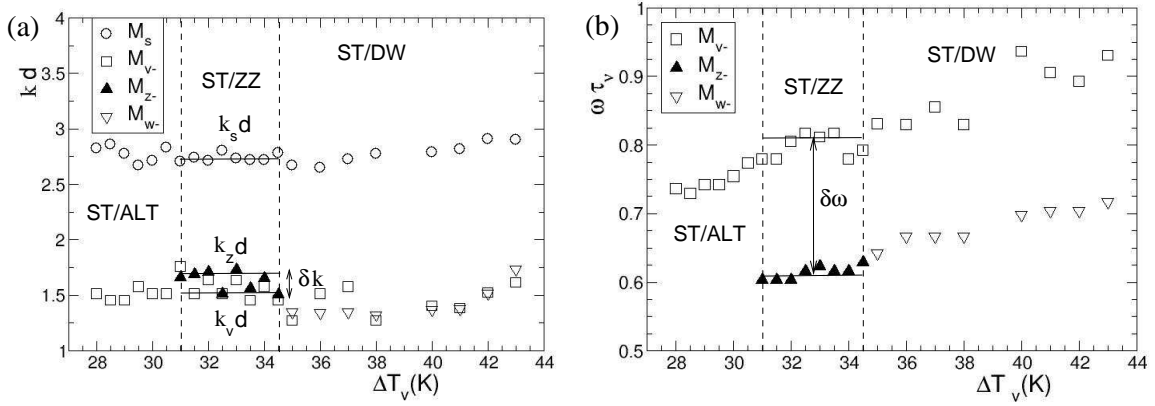


Figure 3.13: Evolution of the wave numbers (a) and the frequencies (b), scaled with $d = 3$ mm and $\tau_v = d^2/\nu = 1.8$ s, respectively. Vertical dashed lines correspond to threshold values ($\Delta T_{vc2} = 31$ K, $\Delta T_{vc3} = 34.5$ K) that bound the ST/ZZ regime and solid lines in the ST/ZZ regime are a guide to the eye.

- (i) **A mixed ST/ALT pattern** [see a typical surface image in Fig. 3.15(a)]. At $\Delta T_{vc1} = 21$ K, the system bifurcates towards a regime of fluctuating domains, which are irregular clusters of variable size in the ALT pattern that usually collapse [Fig. 3.14(a,b)]. From results in Fig. 3.13(b) we obtain that traveling modes have an average period of approximately 15 s.
- (ii) **A spatiotemporal beating regime or ST/ZZ pattern** [see Fig. 3.15(b)]. At $\Delta T_{vc2} = 31$ K and for a range of 5 K, one or two large domains with a zig-zag geometry (the ZZ pattern) and with an average width of $L_c \approx 80$ mm coexist with the ST pattern [see the coherent ZZ domain in Fig. 3.14(d,e)]. The ZZ domains are stationary clusters resulting from the splitting of the spatiotemporal frequencies of the fundamental modes. Thus, on the spatial Fourier spectra [i.e. Fig. 3.16(d)] we detect two close wave numbers k_z and k_v , and on the temporal Fourier spectra [i.e. Fig. 3.16(c)] we detect two close temporal frequencies² ω_v and ω_z . From the bidimensional Fourier spectrum [Fig. 3.14(f)] we identify these frequencies to belong respectively to the fundamental modes: $M_{v\pm}(k_v, \pm\omega_v)$ and $M_{z\pm}(k_z, \pm\omega_z)$. Consequently, the spatial beating phenomenon comes from $\delta k = |k_z - k_v|$ whereas the characteristic zig-zag geometry is due to the temporal beats $\delta\omega = |\omega_v - \omega_z|$. The further is the system from the threshold, the more numerous are the harmonic modes and hence, nonlinearities are thought to be stronger. From Fig. 3.13(a,b), we measure the envelope periodicities of the spatial and temporal beats ($\delta k, \delta\omega$). These results will be discussed on a later section.
- (iii) **A temporal beating regime or ST/DW pattern** [see Fig. 3.15(c)]. From $\Delta T_{vc3} = 34.5$ K [see Fig. 3.13(a,b)] onward, the spatial frequency splitting disappears. Hence, in this

²We can extract temporal frequencies (ω_v, ω_z) from diagrams $S_{x_o}(y, t)$ [i.e. from the spatiotemporal diagram $S_{x_o}(y, t)$ in Fig. 3.16(a) we obtain the frequency spectrum of Fig. 3.16(b)] and also from diagrams $S_{y_o}(x, t)$ [see Fig. 3.16(c)].

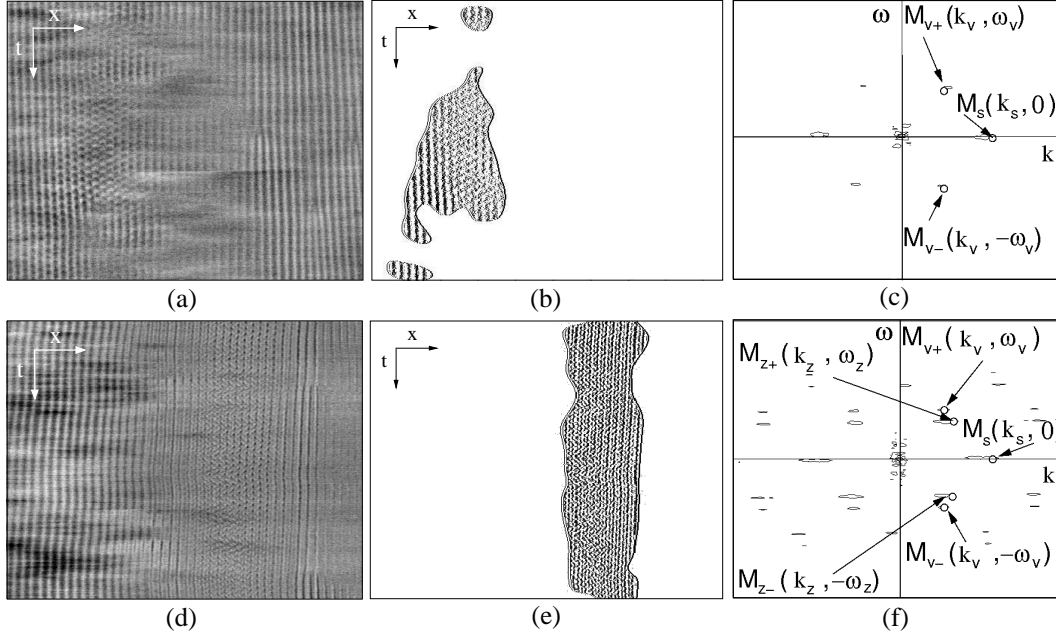


Figure 3.14: Spatiotemporal diagrams $S_{y_o}(x, t)$ in the ST/ALT (a) and the ST/ZZ (d) regimes; (b) and (e) are the corresponding filtered signals by complex demodulation techniques with $\mu = 1/e$; and (c) and (f) are the corresponding Fourier spectra where the fundamental modes have been indicated.

regime the amplitudes of the competing fundamental modes are not able to maintain the spatial beating phenomenon. Then, in this regime only temporal beats exist in a unique and larger localized domain. The new fundamental modes are: $M_s(k_s, 0)$, $M_{v\pm}(k_v, \pm\omega_v)$ and $M_{w\pm}(k_w, \pm\omega_w)$.

Along the whole cascade of bifurcations there is a linear growth of the temporal frequencies with the vertical temperature gradient [see Fig. 3.13(b)], this result contributes to an increasing phase velocity $v_\phi = \omega/k$ with a similar behavior.

For consistency with the following sections we define two reduced control parameters $\varepsilon_1 = \Delta T_v / \Delta T_{vc1} - 1$ and $\varepsilon_2 = \Delta T_v / \Delta T_{vc2} - 1$ for the two subsequent instabilities towards the mixed ST/ALT pattern and towards the spatiotemporal beating regime ST/ZZ, respectively.

3.7.1. Irregular clusters in the mixed pattern

In order to distinguish fluctuating domains in the ST/ALT pattern we visualize only localized domains where counter-propagative modes are involved (see Fig. 3.17). These patterns have a similar morphology to that of irregular clusters appearing in other dissipative systems like in some reaction-diffusion chemical experiments. From the point of view of hotspots, we might think of oscillators belonging to these domains, either being thermoconvective oscillators in our 1D-system or chemical oscillators in the Belousov-Zhabotinsky 2D-system [89], to reach synchronization³ with a critical frequency ω_v .

³In this synchronization bifurcations two critical frequencies $\omega_{v\pm}$ are involved, but from now on we refer to one critical frequency ω_v (or ω_z) depending on the type of synchronization bifurcation.

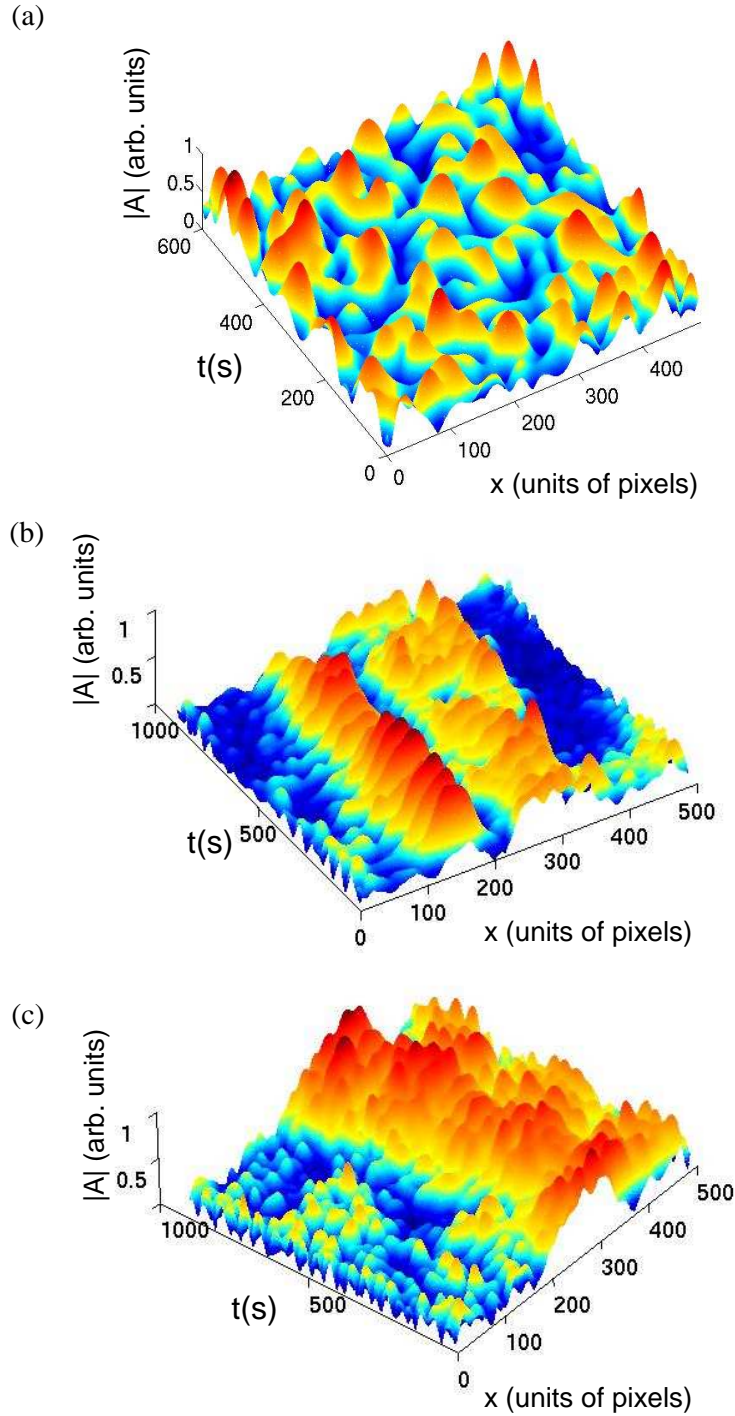


Figure 3.15: Surface images of the demodulated amplitudes of critical modes in: (a) the mixed ST/ALT pattern at $\varepsilon_1 = 0.19$ ($\Delta T_v = 25$ K) where several irregular clusters are shown selecting M_{v-} ; (b) the spatiotemporal beating regime ST/ZZ at $\varepsilon_2 = 0.08$ ($\Delta T_v = 33.5$ K) where two stationary clusters are shown selecting the pair M_{v-} and M_{z-} ; (c) the temporal beating regime ST/DW at $\varepsilon_2 = 0.32$ ($\Delta T_v = 41$ K) where two stationary clusters are shown selecting the pair M_{v-} and M_{w-} .

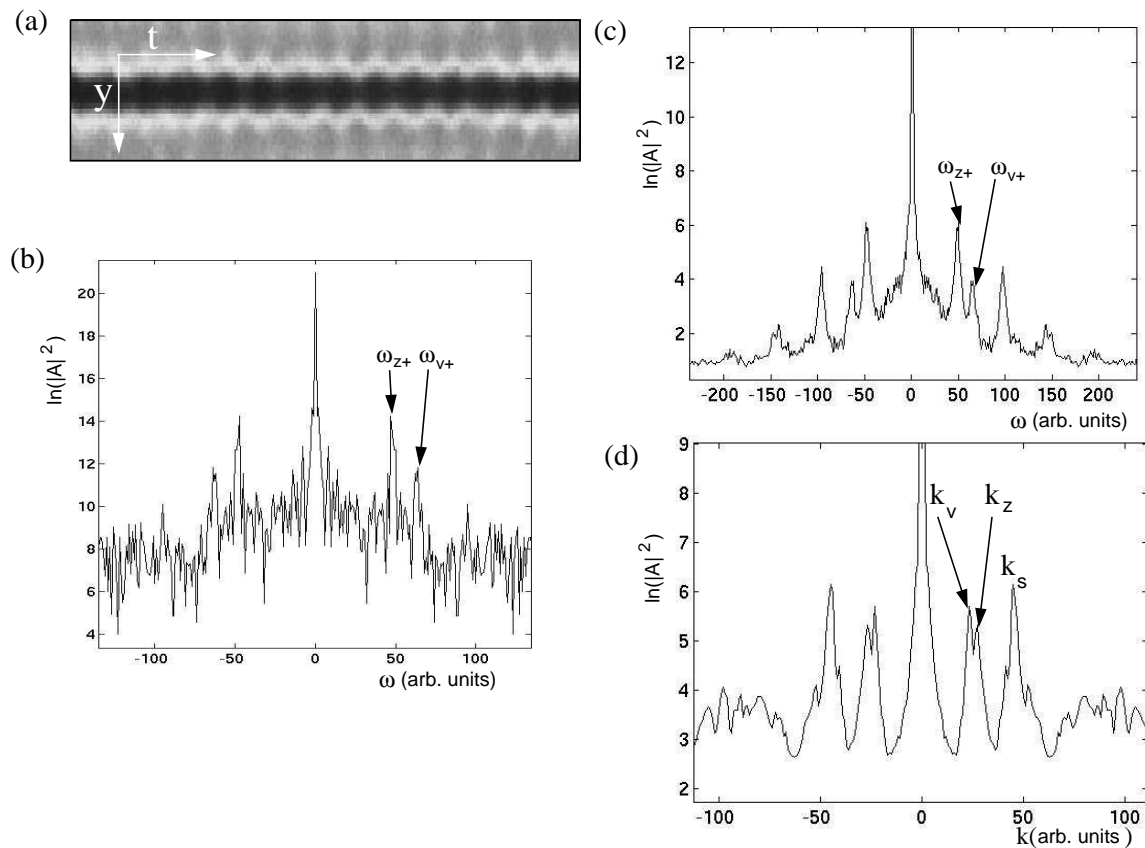


Figure 3.16: In the ST/ZZ regime, at $\Delta T_v = 33.5$ K: (a) spatiotemporal diagram $S_{x_o}(y, t)$ taken over a period of approximately 400 s along a distance $\Delta y = 30$ mm, dark spots correspond to an oscillator belonging to the ZZ domain; (b) Fourier spectrum in ω from the signal $S_{x_o}(y, t)$ [in (a)]. From the signal $S_{y_o}(x, t)$: (c) the Fourier spectrum in ω [the scaling is different from (b)]; (d) the Fourier spectrum in k . The components of the critical mode $M_{z+}(k_z, \omega_z)$ and the previous existing one $M_{v+}(k_v, \omega_v)$ have been indicated in their respective graphics.

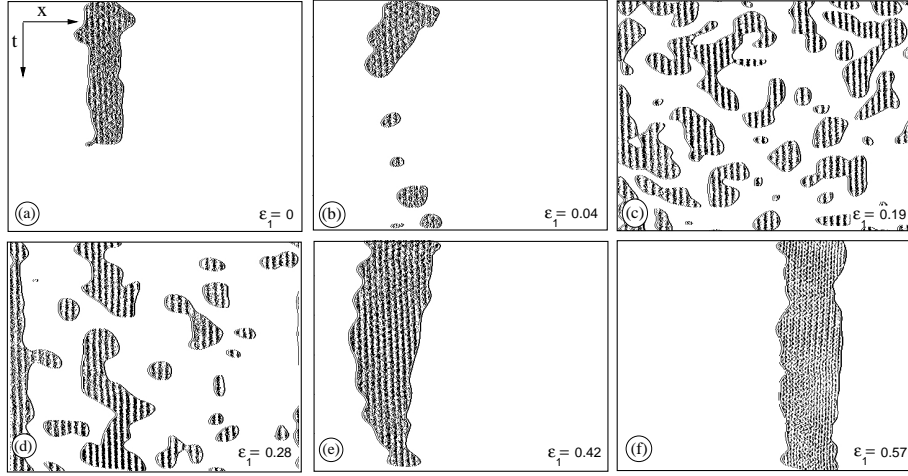


Figure 3.17: Sequence of filtered diagrams $S_{y_o}(x, t)$ with $\mu = 1/e$, the reduced control parameter is defined as $\varepsilon_1 = \Delta T_v / \Delta T_{vc1} - 1$ with $\Delta T_{vc1} = 21$ K. Diagrams (a)-(e) correspond to the mixed ST/ALT pattern, diagram (f) corresponds to the beating regime ST/ZZ at the threshold ($\varepsilon_2 = 0$).

Above the threshold ($\varepsilon_1 = 0$) clusters spread over the whole diagram $S_{y_o}(x, t)$ [i.e. Fig. 3.17(c)] until they stop collapsing at $\Delta T_v \approx 26$ K ($\varepsilon_1 = 0.24$), and saturate into a unique domain of high spatiotemporal coherence [i.e. Fig. 3.17(e)]. This domain will remain in the next instability to spatiotemporal beats [i.e. Fig. 3.17(f)] where two new unstable modes will emerge.

In Fig. 3.18 we show that the modulus of amplitude of the traveling left mode ($|A_{v+}| \approx |A_{v-}|$) is constant in the range $0 < \varepsilon_1 < 0.35$ ($\varepsilon_1 = \Delta T_v / \Delta T_{vc1} - 1$), meanwhile we observe from Fig. 3.13(b) that the corresponding frequency ω_{-v} increases monotonically with ΔT_v with an average value of 0.42 s^{-1} ($\langle \omega \tau_v \rangle = 0.75$). The inset in Fig. 3.18 represents the corresponding subcritical bifurcation diagram of the transition to the mixed ST/ALT pattern. The unstable branch is the basic cellular pattern ST which does not ever become unstable along the explored interval of the control parameter ε_1 . According to previous experimental work reported in Ref. [49] like the plane Couette flow [121], we might consider that at shallow layers subcriticality is sent to infinity, therefore the threshold branch (ST) would be unstable for diverging values of the control parameter ε_1 (see sketch in Fig. 3.18).

Because the quantitative analysis of the critical amplitudes does not reveal the nature of this instability, we decide to follow the evolution of the invasion rate σ_{inv} of the irregular clusters along ε_1 [see Fig. 3.19(a)]. If we compare these results with the filtered images in Fig. 3.17 we infer that, from the initial irregular cluster as we increase the control parameter (ε_1) the invasion rate increases monotonically (left branch) until irregular clusters spread “inhomogeneously” all over the spatiotemporal diagram $S_{y_o}(x, t)$ at $\sigma_{inv} \approx 0.40$ [i.e. Fig. 3.17(c)]. At this stage the average size of irregular clusters is $L_c \approx 30$ mm. This state is termed spatiotemporal chaos regime (STC) because of the decaying spatial and temporal correlation lengths [i.e. Fig. 3.15(a)]. From this point onward, the right branch in Fig. 3.19(a) decreases reaching a constant value of $\sigma_{inv} = 0.14$. This final value belongs to the pattern in Fig. 3.17(e) that is close to the threshold of the following bifurcation to the beating regime ST/ZZ where two domains saturate to a fixed width value of $L_c \approx 80$ mm. In Fig. 3.19(a) we have also tested the behavior of the right branch with a smaller

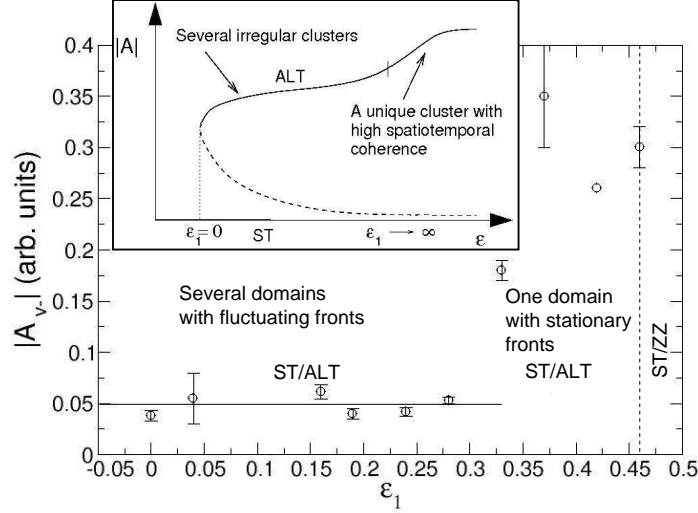


Figure 3.18: Evolution of the amplitude of the fundamental traveling mode M_{v-} along an ascending sequence of $\epsilon_1 = \Delta T_v / \Delta T_{vc1} - 1$ inside the bifurcated domains. Vertical dashed lines separate different regimes and the solid line corresponds to the average amplitudes. The inset is a sketch of the diagram of bifurcation from the stationary ST regime to the ST/ALT regime.

step.

3.7.2. Supercritical bifurcation to stationary clusters

In Fig. 3.15(b) we show a demodulated pattern in the spatiotemporal beating regime ST/ZZ with two coherent domains. These domains are two stationary clusters of width $L_c \approx 80$ mm [see also the filtered spatiotemporal diagrams in Fig. 3.20(a-d)] which exhibit stationary 1D-fronts ($v_p \approx 0.01$ mm/s). For an ascending sequence, the first stationary cluster emerges at $\epsilon_2 = 0$ ($\Delta T_v = 31$ K) from a previous ALT domain with high spatiotemporal coherence. Stationary clusters have been analyzed along two ascending sequences with steps of 0.5 and 1 K. As it is expected, the invasion rate [Fig. 3.19(b)] is approximately constant ($\sigma_{inv} \approx 0.18$) along the ST/ZZ regime. However, above $\epsilon_2 = 0.11$ ($\Delta T_{vc3} \approx 34.5$ K) at the ST/DW regime, the invasion rate increases because a unique and wider domain in DW appears where only temporal beats remain [see Fig. 3.15(c)]. Further above $\epsilon_2 \geq 0.29$ a different dynamics due to the increasing number of dislocations is responsible for a variable σ_{inv} . At this last stage, like in the pattern shown in Fig. 3.21 defects appear as chains of dislocations forming 1D-fronts and also a global drift is produced.

From results in Fig. 3.13(a,b), we extract the envelope frequencies: $\delta k \approx 0.04$ mm $^{-1}$ and $\delta \omega \approx 0.10$ s $^{-1}$. These results are in agreement with the spatiotemporal periodicities of the demodulated signals shown in Fig. 3.20(a-d), the spatial periodicity of the beats is of 157 mm ($\approx 2L_c$) and the time periodicity is of 124 s which is the doubled value of the brightness periodicity of zig-zags. In agreement with the results in Fig. 3.13(b), far beyond the threshold of the ST/DW pattern, there is an increasing number of temporal beats because the distance $\delta \omega$ becomes larger. From the

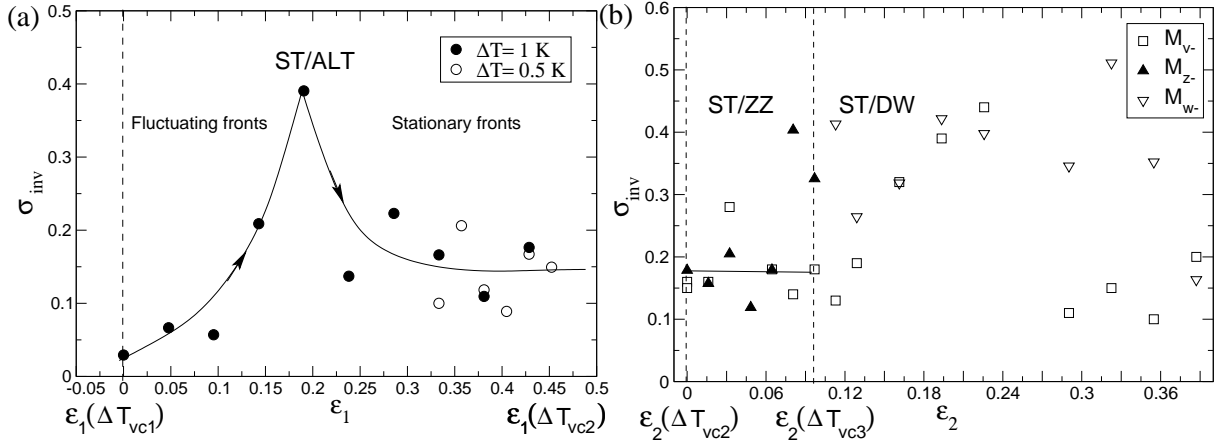


Figure 3.19: (a) Invasion rate of the traveling mode M_{v-} close and above the bifurcation to the mixed ST/ALT pattern for two different sequences with steps $|\Delta T_v| = 1$ and 0.5 K. The reduced control parameter is $\varepsilon_1 = \Delta T_v / \Delta T_{vc1} - 1$. Solid lines are a guide to the eye; (b) invasion rate determined by the modes M_{z-} and M_{v-} that represent the beating regime with $\mu = 1/e$ and along an ascending sequence. The reduced control parameter is $\varepsilon_2 = \Delta T_v / \Delta T_{vc2} - 1$. Vertical dashed lines separate different regimes at threshold values: $\Delta T_{vc1} = 21$ K, $\Delta T_{vc2} = 31$ K, $\Delta T_{vc3} = 34.5$ K.

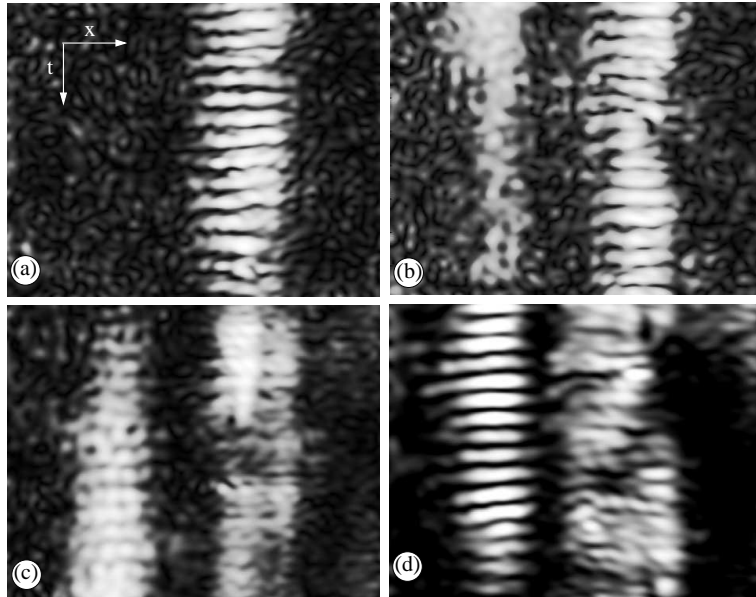


Figure 3.20: A sequence of demodulated diagrams $S_{y_o}(x, t)$ selecting the pair M_{v-} , M_{z-} for increasing ΔT_v in the ST/ZZ regime: (a) 31 K ($\varepsilon_2 = 0$), (b) 31.5 K ($\varepsilon_2 = 0.02$), (c) 32 K ($\varepsilon_2 = 0.03$), (d) 33.5 K ($\varepsilon_2 = 0.08$). Dark and bright regions correspond to the minimum and maximum values of the amplitude.

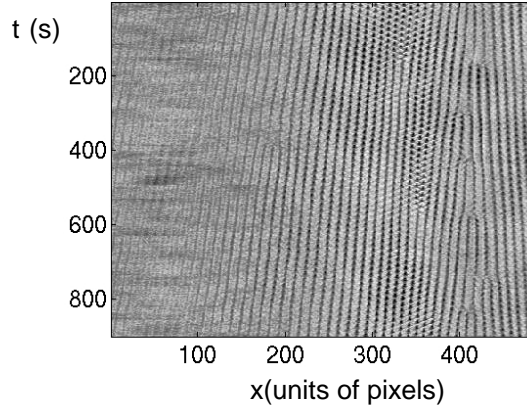


Figure 3.21: Spatiotemporal diagram of the ST/DW pattern at $\varepsilon_2 = 0.39$ ($\Delta T_v = 43$ K).

demodulated signals we infer that this beating phenomenon depends on the competition between the fundamental modes $M_{z\pm}$ and $M_{v\pm}$.

In this transition towards the ST/ZZ regime, the analysis of the module of the critical amplitudes $|A_{z\pm}|$ on the whole diagram $S_{y_o}(x, t)$ and restricted to the ZZ domain [see Fig. 3.22(a)] provides a suitable order parameter. In Fig. 3.22(a) we show the continuous growth of the critical amplitudes $|A_{z\pm}|$ until the onset of the ST/DW regime. This result agrees with a supercritical bifurcation that is developed inside the stationary clusters coexisting with ST. However, the amplitude of the stationary mode analyzed inside these stationary clusters [see Fig. 3.22(b)] keeps constant along the ST/ZZ regime.

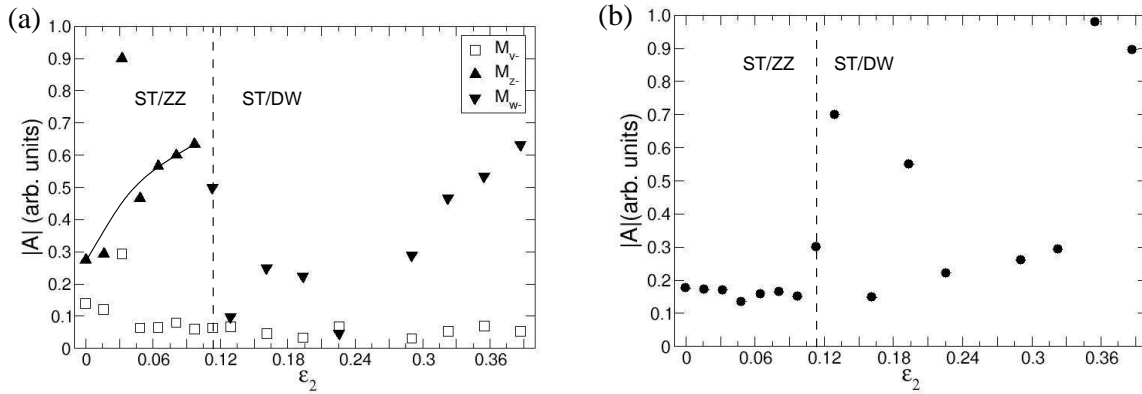


Figure 3.22: (a) Evolution of the amplitudes of the fundamental modes M_{z-} , M_{v-} inside the domains defined by ZZ and DW; (b) evolution of the amplitude of the stationary mode M_s inside the same domains in order to filter the resonant contribution of the mode M_s at the boundaries [the scaling in amplitudes is different from (a)]. Dashed lines correspond to threshold values and solid lines are a guide to the eye. In (a) and (b) $\varepsilon_2 = \Delta T_v / \Delta T_{vc2} - 1$ with $\Delta T_{vc2} = 31$ K.

In Chapter 4 we show from an **oscillators-network** point of view that this supercritical transition to ST/ZZ is the beginning of a global phase synchronization transition towards a

spatiotemporal phase synchronization of the coupled array of N -convective oscillators.

3.8. Bistability and 1D-fronts

In the asymptotic regimes, 1D-fronts connecting bistable patterns are stationary ($v_p \approx 0$) in the coexisting ST/ALT+TW, TW+ALT and ST/ZZ regimes. These stationary 1D-fronts are related to strong locking phenomena between two different modulated patterns. According to theoretical results in reaction-diffusion reactions [46, 47] where there are two competing diffusivities in the system, which obey that $D_2 \ll D_1$ (in our case $D_2 \equiv \kappa = 6.68 \cdot 10^{-8} \text{ m}^2 \text{ s}^{-1}$ is the thermal diffusivity, and $D_1 \equiv \nu = 5 \cdot 10^{-6} \text{ m}^2 \text{ s}^{-1}$ is the kinematic viscosity), it is found that the front velocity of propagation v_p fulfills $v_p \approx \sqrt{D_2}$ along a finite interval of the control parameters. Therefore, it is expected that the diffusion of a new phase into the original one is restrained with a zero front velocity because of the low thermal diffusivity of the fluid. Nevertheless, ALT domains (irregular clusters) coexisting with the ST pattern exhibit fluctuating 1D-fronts with a varying front velocity that becomes negative in the case of collapsing fronts. All these fronts belong to the normal type connecting two stable patterns that are solution of the system for the same values of the control parameters (see a more extended review about fronts in Chapter 1). A discontinuity of the order parameter (i.e. the amplitude of the critical modes or the invasion rate) in a first order instability is the reason why fronts do exist. If the dynamics of the system could be reproduced by a Lyapunov functional (variational system), then the original patterns (ST, ST/ALT and TW) and the corresponding bifurcated patterns (ST/ALT, TW and ALT, respectively) would be bistable solutions corresponding to the local and global minima respectively of a double-well Lyapunov functional.

We have previously shown that subcriticality vanishes above the codimension-2 point with dynamic Bond number $Bo_D \approx 2.38$ and according to this fact for $d > 4.5 \text{ mm}$ there are no 1D-fronts. Below the codimension-2 point, measurements on the attenuation length ξ as a subcritical length have not provided any suitable information about the dynamics of the 1D-fronts along a sequence as we show next. We try to approach the understanding of 1D-fronts for:

- *Intermediate layers* ($d = 4 \text{ mm}$). Along an ascending sequence with step 1K we measure the attenuation length in the bifurcation from the ST/ALT pattern to the TW pattern obtaining $\langle \xi \rangle \approx 27 \text{ mm}$. In the next bifurcation towards the ALT pattern we measure $\langle \xi \rangle \approx 24 \text{ mm}$. If we average discontinuities of the 1D-front, that are of the order of 8 mm around a uniform profile, we can infer that the attenuation length does not depend on the control parameter ΔT_v , but only on the characteristic diffusions (κ and ν) of the fluid. It should be stressed that at the threshold of both instabilities one or two 1D-fronts may appear depending on the location of the new pattern, either in one side or in a middle position, respectively. We focus on the last bifurcation to the ALT pattern that is produced at $\Delta T_{vc} = 21.5 \text{ K}$ (see diagrams in Fig. 3.23), at the onset there is a stationary 1D-front between these two patterns (TW and ALT) that propagates at zero velocity. In order to follow the 1D-front dynamics we define the control parameter $\varepsilon^* = \Delta T_v / \Delta T_{vc} - 1$. As the system is driven far away from the onset increasing ΔT_v , the 1D-front invades the TW domain until the whole system dynamics has transitioned to the ALT state at $\varepsilon^* = 0.29$ [i.e. Fig. 3.23(c)]. In this transition we have measured a finite jump of the amplitudes of the traveling modes at the

threshold: $|A_{v\pm}|(ALT) \approx 3|A_{v-}|(TW)$ while the amplitude of the stationary mode fulfils: $|A_s|(ALT) \approx |A_{v\pm}|/2(ALT)$.

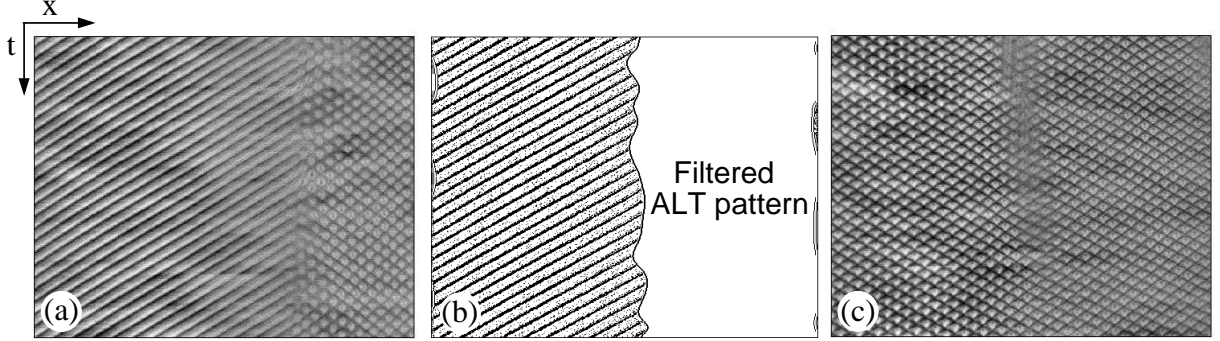


Figure 3.23: Spatiotemporal diagrams corresponding to a secondary bifurcation to ALT above the threshold: (a) there is a front connecting the TW and ALT patterns at $\varepsilon^* = 0.11$; (b) contrasted profile of the front (the left traveling mode has been filtered with $\mu = 1/e$) at $\varepsilon^* = 0.15$; (c) the ALT pattern has invaded the whole cell far from the threshold at $\varepsilon^* = 0.38$.

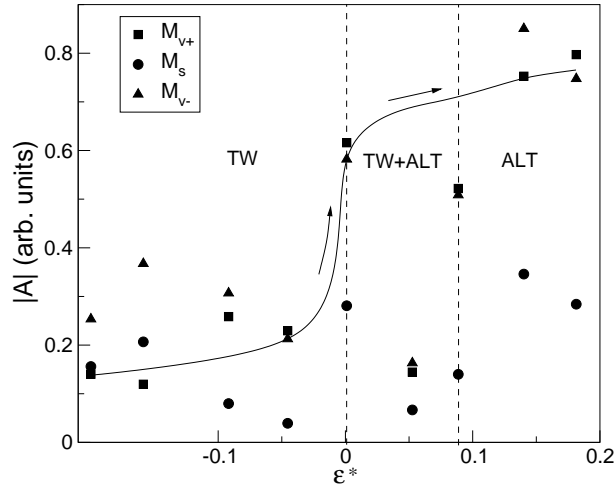


Figure 3.24: Evolution of the amplitudes of the fundamental modes along an ascending sequence of measurements from TW to ALT. The control parameter is defined as $\varepsilon^* = \Delta T_v / \Delta T_{vc} - 1$ with $\Delta T_{vc} = 21.5$ K when the stationary 1D-front first appears. Solid lines follow the discontinuous bifurcation towards the ALT pattern. Dashed lines split different regimes.

These stationary 1D-fronts are also found in catalytic reaction systems with 1D heating [36]. Theoretically, the minimum front velocity is achieved at the Maxwell point [3], but in accordance to our results the system has a *Maxwell interval*. This interval, with a minimum and constant velocity, has been theoretically studied in the previously mentioned reaction-diffusion model [46, 47]. Therefore, for intermediate layers this model fits the stationary front dynamics with $v_p \approx \sqrt{\kappa} \approx 2.58 \cdot 10^{-4} \text{ m s}^{-1}$.

- *Shallow layers* ($d = 3$ mm). Although for shallow layers capillary tensions are stronger than buoyancy forces, the zero front velocity found in the ST/ZZ regime between adjacent

patterns might obey the same diffusion model as the one explained above for intermediate layers, except for the fluctuating fronts in the mixed ST/ALT regime. Measurements on the attenuation length of the new ST/ZZ pattern inside the original ST pattern might be subjected to the same diffusion model because we obtain $\langle \xi \rangle \approx 30$ mm. Moreover, this result is in agreement with the interaction range found out for the same regime in the following chapter involving approximately 4-5 oscillators (≈ 30 mm).

Fluctuating 1D-fronts in the mixed ST/ALT pattern are generated when the resonant triad is locally triggered. This process has been observed in both, intermediate (ST/ALT+TW) and shallow layers (ST/ALT before ST/ZZ). As it has been shown in a previous section, only the nature of the mixed pattern at shallow layers allows us to develop a detailed study using the invasion rate ⁴. When the system is yielding fluctuating boundaries in the clustering process, the new “phase” in ALT grows inhomogeneously in the form of stochastic patches, like contamination processes in percolation transitions ⁵. In extended systems, this kind of phenomena was considered to be important by Pomeau [3], regarding the onset of chaos at “*subcritical turbulent*” transitions he found similarities between the underlying mechanism of percolation phenomena and spatiotemporal intermittency. In this direction, spatiotemporal patches emerging from a basic ST pattern, that always remains with increasing control parameter ΔT_v (a subcritical instability where the lower branch diverges for high values of the control parameter), show similarities with spatiotemporal intermittency regimes developed in other extended systems, for example in open flows (i.e. turbulent bursts of active patches over a laminar flow in the plain Couette experiment [51]) and in reaction-diffusion systems (i.e. fluctuating patches in the Belousov-Zhabotinsky reaction [122]).

3.8.1. Transient regimes in bistable systems

At the onset of the reported critical phenomena there is still one fundamental question to be answered: What information could we get about the convective or absolute nature of a transition? This question demands to study transient regimes close to the threshold of an instability.

For transient regimes we have observed the existence of pulses, sources, sinks and localized drifting domains with well defined boundaries and 1D-fronts. These 1D-fronts are the Fisher-Kolmogorov-Petrovsky-Piskunov fronts (FKPP) which are formed in transients moving with the minimum velocity.

Bistability is the common feature of patterns sustaining fronts and it is easily discovered from transient regimes. A transient regime produced by a temperature quench is shown in Fig. 3.25 where bistability causes the existence of localized drifting domains displaying the unstable pattern and a 1D-source. Localized domains propagate over the original pattern (TW) and locally break the symmetry imposed by the underlying pattern.

In our system, transients might also be generated by perturbing locally and mechanically the free surface close to the threshold. Next, by applying this method the critical modes are excited.

⁴For intermediate layers, the presence of a TW domain in the coexisting ST/ALT+TW pattern as ΔT_v is increased “confines” the ST/ALT pattern into a narrower region in few steps $|\Delta T_v|$ ($|\Delta T_v|$ is restricted by the accuracy of the experimental temperature controller).

⁵Contamination processes (i.e. directed percolation) in spatiotemporal intermittency were firstly introduced by Kaneko [131]. Theoretical treatment is divided into non-universal behavior of directed percolation transitions [132] and universality (i.e. coupled circle maps [133]).

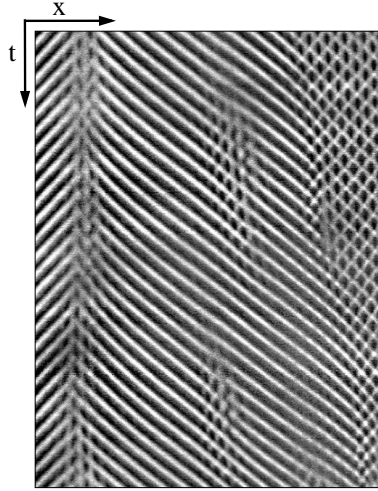


Figure 3.25: Spatiotemporal diagram of TW ($d = 4$ mm, $\Delta T_v = 20$ K) with localized drifting domains in the ALT pattern in a transient (for an upward jump with step $|\Delta T_v| = 4$ K) and the presence of a source of TW in the left hand side.

We study the following spatiotemporal diagrams in transients:

- *At the onset of the TW bifurcation* ($d = 4$ mm). The basic state ST just below $-\varepsilon_c$ (at $d = 4$ mm, $\Delta T_v = 15.5$ K) is perturbed, in Fig. 3.26(a,b) we observe the generation of a TW domain. This domain vanishes after a while because a relaxational dynamics exists below the threshold. In Fig. 3.26(c) we show the attenuation of the amplitude $|A_{v-}|$ inside the transient TW domain. The front velocity is $v_p \approx 0.17$ mm/s, therefore, close to the threshold, the TW pattern is said to be convectively unstable with a negative group velocity: $|v_g| \approx 0.12$ mm/s. The phase velocity verifies $v_\phi \approx -3.5 v_g$. Whereas, if we perturb the system above and close to the threshold, the group velocity is null. Because of the small linear group velocity we infer that the convective nature of the TW instability as we settle the system above and close to the threshold becomes straightaway absolute. On the other hand, although the TW domain arises locally in the transient regime, this instability has a global character because when the system is far away from the threshold, the TW regime invades the whole system. This global-convective/absolute instability to the TW pattern at $d = 4$ mm (with $Bo_D \approx 1.7$) compares well with the theoretical work developed by Priede and Gerbeth [65] that explains that for large Prandtl number fluids and deep layers (when buoyancy effects are important) oscillatory instabilities follow the same dynamics in the sense that the convective and the absolute thresholds might coincide.
- *Close to the threshold of the ST/ZZ bifurcation* ($d = 3$ mm). We observe in Fig. 3.27(a) that when we locally disturb the surface, the corresponding oscillatory domains become globally unstable in transient regimes (not locally as the aforementioned example for the TW instability). Besides, 1D-fronts show no transversal drifting (stationary 1D-front with $v_p \approx 0.017$ mm/s). In consequence, this instability has an absolute character with a zero group velocity. Besides, the critical amplitudes do not decay along the measurement [see Fig. 3.27(b)].

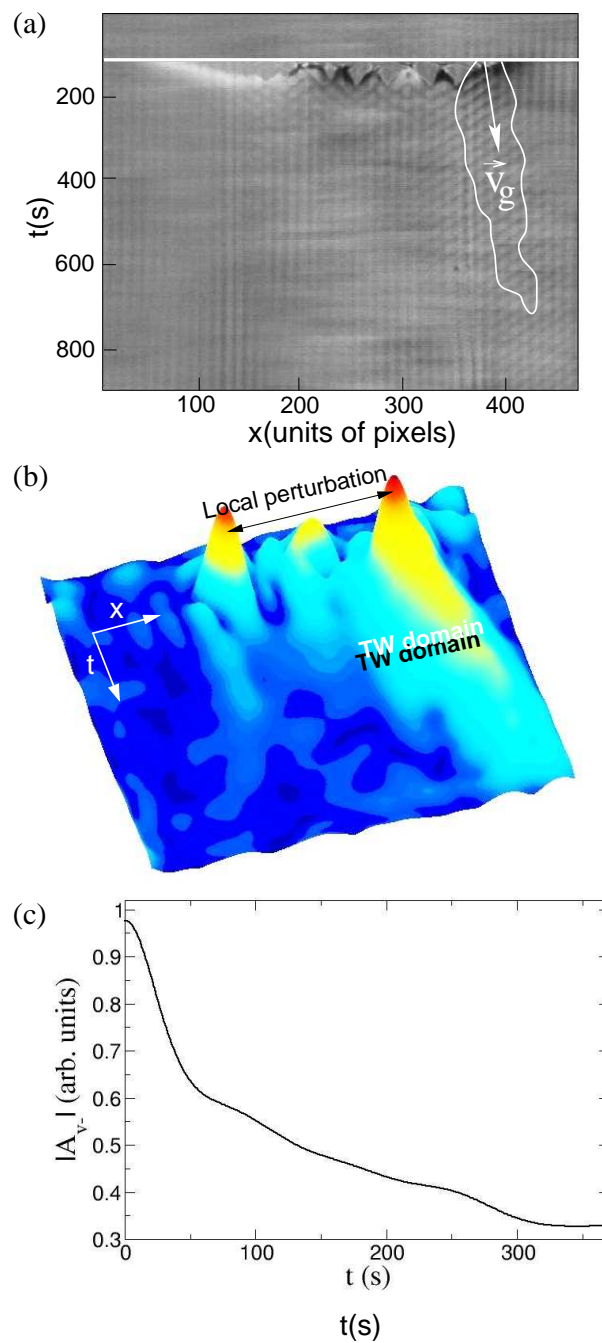


Figure 3.26: Close to the threshold of the TW pattern at ($d = 4$ mm, $\Delta T_v = 15.5$ K): (a) spatiotemporal diagram of a transient produced by a local mechanical perturbation. The sketched boundary of the drifting TW domain has been filtered with $\mu = 1/e$; (b) surface image of the amplitude of the unstable traveling mode A_{v-} corresponding to the spatiotemporal diagram in (a); (c) attenuation of the module of the traveling mode M_{v-} inside the transient domain starting at the perturbation.

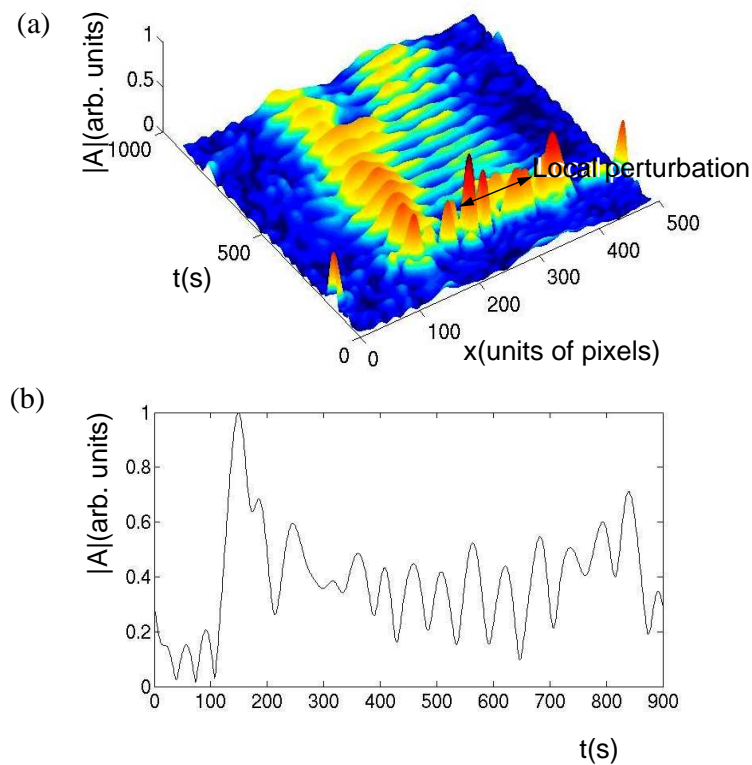


Figure 3.27: (a) Surface image of the demodulated amplitude of the critical modes M_{v-} and M_{z-} in a transient regime close to the ST/ZZ threshold. (b) Evolution of the amplitudes of the critical mode A_{z-} belonging to the right coherent domain in ZZ along the whole measurement.

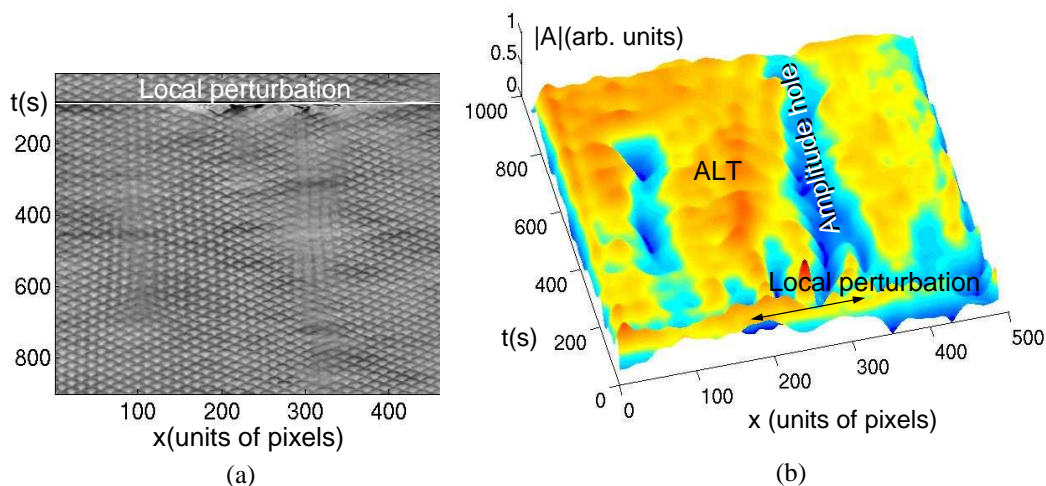


Figure 3.28: (a) Spatiotemporal diagram corresponding to a locally perturbed ALT pattern at ($d = 4$ mm, $\Delta T_v = 27$ K). (b) From (a), the surface image of the demodulated amplitude of the critical mode M_{v-} . A stationary hole solution propagates along the recorded spatiotemporal diagram.

- *Far from the threshold of the ALT bifurcation ($d = 4$ mm).* A stationary wave-hole (an amplitude hole) and a transient wave-hole are shown in Fig. 3.28. This kind of localized nonlinear wave phenomena were theoretically dealt by Mills and Trullinger [134] in superlattices looking for kink and antikink electromagnetic wave solutions. Particularly close to hydrodynamic systems is the work of Gil [19] for cellular patterns, using a more general normal form than the one developed in the CI theory, found numerically similar gap solitons (stationary and drifting).

3.9. Discussion and conclusions

In this chapter we have experimentally studied the dynamics of a thermoconvective fluid layer under a quasi-1D heating. By working with different depths of the fluid layer, shallow layers ($d \leq 3$ mm) and intermediate layers ($4 \text{ mm} \leq d \leq 4.5$ mm), we report two main different routes to weak turbulence (see the corresponding diagrams of bifurcation in Fig. 3.29). At critical values of the control parameter ΔT_v new regimes, that are characterized by a higher degree of broken symmetries, spontaneously emerge. These instabilities happen to be of absolute and global nature, except for the convective/absolute nature of the TW bifurcation which was previously discussed. From transient regimes we have checked that critical modes are damped below and close to thresholds (relaxational dynamics), on the other hand above and close to thresholds typical domains belonging to the new state are triggered.

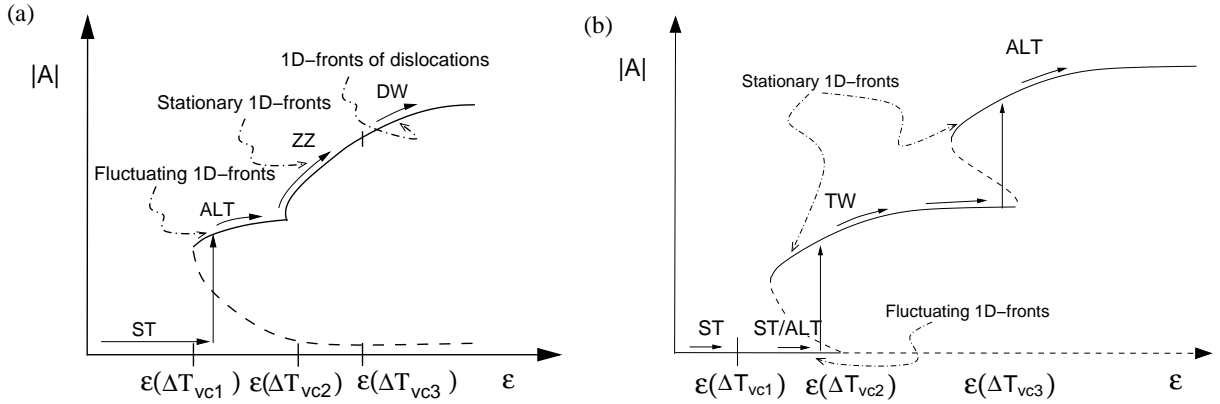


Figure 3.29: Bifurcation diagrams $|A|$ vs ε at (a) $d = 3$ mm and (b) $d = 4$ mm, where $\varepsilon = \Delta T_v / 0.1\text{K} - 1$ is the reduced control parameter defined from the threshold of the instability to ST while $\varepsilon(\Delta T_{vc1})$, $\varepsilon(\Delta T_{vc2})$ and $\varepsilon(\Delta T_{vc3})$ are the reduced control parameters at the thresholds of the subsequent instabilities. Solid arrows follow the upward bifurcations.

Discussion on the results is principally focussed on decoding universality in critical nonlinear phenomena from the analysis of our dissipative and extended 1D-system. Extended systems are susceptible to exhibit a high number of degrees of freedom, like our 1D-array of $N \approx 80$ nonlinearly coupled oscillators beyond the primary convection. Each oscillator or convective cell has its local kinetics and besides interacts nonlinearly with its neighbors. According to this, from the shadowgraphy images we are analyzing critical phenomena in the macroscopic framework disregarding “microscopic fluctuations”.

Entrainment or synchronization between interacting oscillators define domains or clusters with the same oscillatory pattern with well defined 1D-fronts. These 1D-fronts can be fluctuating or stationary depending on the coupling strength between oscillators. Weak coupling of the resonant triad $(M_s, M_{v\pm})$ always yields fluctuating 1D-fronts which may eventually collapse, meanwhile stronger coupling yields locking of the new pattern at the 1D-fronts with a zero front velocity according to the aforementioned theory for reaction-diffusion processes [46, 47] where the velocity of propagation obeys $v_p \approx \sqrt{\kappa} \approx 0$ for $Pr = \nu/\kappa \gg 1$. This zero diffusion velocity holds for an interval of ΔT_c at the asymptotic regimes, so this is the cause for defining this range of coexistence with zero diffusion velocity as a *Maxwell interval*.

According to the dynamical Bond number which might be expressed as $Bo_D \propto d^2$, together with subcriticality in the studied range $3 \text{ mm} \leq d \leq 4.5 \text{ mm}$ (see the stability diagram in Fig. 3.5), we might relate the increasing effect of thermocapillary as d decreases to the stronger subcritical nature of instabilities.

Results on the correlation length ξ , which does not diverge in neither of the reported instabilities, indeed $\xi \approx 30 \text{ mm}$, provide evidence on a possible *nonlocal coupling* (further beyond first neighbors) between oscillators. According to this fact, a suitable *spatiotemporal synchronization* theory for spatially extended systems might cope with the whole phase space. In bistable regimes *spatial synchronization* would define the morphology of *time synchronized* domains in ω_v for the ALT domains, and in ω_z for the ZZ domains.

Nevertheless, regarding the theoretical tools we have, possible models might be basically tackled according to the layer depth:

- (i) *For intermediate layers:* Results on the secondary transition to TW show that $\lambda_{TW}/\lambda_s \approx 3/2$ ($q = 2/3$), this wave length differs from the predicted doubled wave length ($q = 1/2$) by the CI theory [16] assuming a commensurate transition (for a non irrational wave number q). Although the convective cells are confined on the heating line (in the \hat{x} direction), at first sight we might infer that the selected travelling mode $q = 2/3$ responds to the contributions of the other involved directions in the system (\hat{y}, \hat{z}). However, the Gaussian profile of the temperature field on the \hat{y} direction does not yield a 2D-travelling pattern on the $\hat{x} \times \hat{y}$ cell. On the other hand, in case that a coupling between the dynamics at the boundary cooling walls and the inner quasi-1D dynamics could be possible, we find out from a previous work by Burguete [79] (with different thermal conditions at the bottom of the cell), that there is no dependence of q on the geometrical aspect ratio (L_x/L_y), although it was found that $q = 1/2$ for the TW pattern. On the other hand, differences between our experimental results and CI theory might be due to the subcritical nature of our system. At the onset of the transition to TW there is coexistence between a new TW domain and the previous mixed ST/ALT pattern. In the ST/ALT pattern, the resonant triad $[M_s(k_s, 0), M_{v\pm}(k_s/2, \pm\omega_v)]$ has been triggered because of the nearby traveling mode [for example the left one $M_{v-}(2k_s/3, -\omega_v)$ or the right one $M_{v+}(2k_s/3, \omega_v)$]. Regarding this fact, we consider that one possible reason that could explain the difference in q would come from the fact that normal forms, like the amplitude-phase coupled equations in the CI theory, are obtained at the onset of an instability, where enslaved modes (or fast modes) have been disregarded [16, 19, 135].

Drifting TW domains in transients are expected in the bistable regime (where we have checked the existence of a hysteresis cycle). This kind of regimes might be described by the

kind of amplitude and phase coupled equations that for a parity-breaking bifurcation were developed by Coulet [136] and Goldstein [17]:

$$\mathcal{A}_t = \mathcal{A}_{xx} + f(\mathcal{A}) + \alpha\phi_x\mathcal{A} + \beta\mathcal{A}\mathcal{A}_x + \dots, \quad (3.1)$$

$$\phi_t = \phi_{xx} + \gamma\mathcal{A} + \dots, \quad (3.2)$$

This model represents the coupling between the slowly varying phase ϕ (phase mismatch between the TW domain and the underlying cellular ST pattern) and the slowly varying amplitude \mathcal{A} of the unstable mode (the traveling mode M_{v+} or M_{v-}). The coupling parameters are α , β and γ . In the subcritical bifurcation to TW, if we disregard the existence of fluctuating patches in ALT, $f(\mathcal{A})$ might be expressed in terms of a fifth-degree polynomial of \mathcal{A} , because higher order terms in $|\mathcal{A}|^n$ (with odd n) are able to stabilize localized solutions in a subcritical framework. When we mechanically perturb the fluid at the onset of the TW bifurcation [Fig. 3.26(a,b)], the excitation of the amplitude of the traveling mode produces a coupling between the amplitude of the critical mode (M_{v+} or M_{v-}) and the phase gradient ϕ_x according to equation Eq. (3.1). On the other hand, Goldstein [17] considered in Eq. (3.2) the rate at which TW are generated with a new term $\gamma\mathcal{A}$. This model also considers the advection of the TW at the onset of the instability with terms like $\phi_x\mathcal{A}$ and $\mathcal{A}\mathcal{A}_x$.

- (ii) *For shallow layers:* The corresponding bifurcation diagram for our spatially extended 1D-array of convective oscillators is sketched in Fig. 3.29(a). We show a cascade of bistable regimes where the basic cellular ST pattern is always a stable solution. This cascade of bifurcations is measured for a reduced control parameter $\varepsilon = \Delta T_v/0.1\text{K} - 1$ where $\Delta T_v = 0.1$ K is the threshold of the primary instability from PC towards the stationary ST pattern. Using the amplitude of the critical modes $|A_{z\pm}|$, as the most convenient order parameter, we show how the system undergoes a supercritical bifurcation to the beating regime ST/ZZ. Synchronized clusters have different coherent widths which might be expressed in terms of the subcritical length L_c . There is a subcritical width in the ST/ZZ pattern determined by L_c that enables a supercritical bifurcation of the critical oscillatory modes $M_{z\pm}$ (inside a unique domain at the onset). This instability appears from a mixed ST/ALT pattern of localized clusters which are inhomogeneously scattered (spatiotemporal chaos regime \equiv STC regime). We have shown that the size of the clusters at the spatiotemporal beating regime $L_c \approx 80$ mm is given by the wave length of the spatial phase envelope and comes from the spatial frequency splitting. Nevertheless, this subcritical length is of the order of the correlation length at the spatiotemporal chaos regime (STC): $L_c \approx \xi \approx 30$ mm. Oscillators belonging to this STC regime are synchronized in ω_v , but often collapse. This clustering process is very similarly to an aging clustering dynamics for weak coupling, hence a possible theoretical approach is close to the diffusion-induced inhomogeneity proposed by Daido and Nakanishi [137], however it is developed in the framework of a global coupling. As we increase the control parameter a growth of the phase coherence is produced until the ensemble of N -coupled oscillators becomes phase synchronized in ω_z . Further beyond, the system keeps only temporal beats in the last ST/DW pattern.

In Fig. 3.30 we sketch the process of inhomogeneous growth of the “phase coherence” towards an “ordered phase” in the ST/ZZ pattern by means of a spatiotemporal synchronization transition where the order parameter is the module of the amplitude of the critical oscillatory

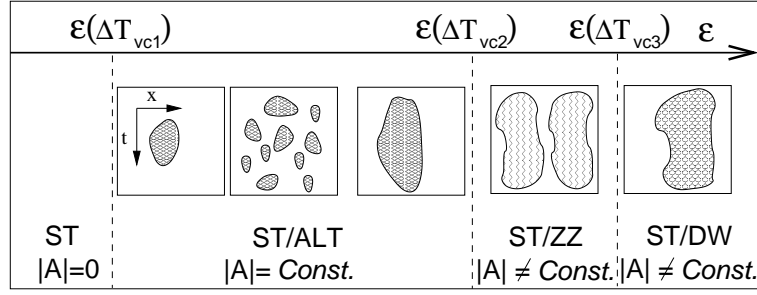


Figure 3.30: Sketch of the dynamics of the localized domains for the increasing control parameter $\varepsilon = \Delta T_v / 0.1\text{K} - 1$ defined from the threshold of the instability to ST (at $\Delta T_v = 0.1\text{K}$). The order parameter is the amplitude $|A|$ of the corresponding critical modes.

modes. We should emphasize that, from the data analysis, we show that the amplitudes of the critical modes ($M_{v\pm}$), inside the irregular domains in ALT, are constant with increasing control parameter ε until the ST/ZZ regime. Meanwhile, the number of irregular clusters is variable (variable invasion rate σ_{inv}). Previously, we have compared this transition with percolation phenomena and spatiotemporal intermittency regimes, this is because in these processes oscillators are becoming synchronized (in the ST/ALT pattern they oscillate with $\omega_{v\pm}$) and may cease to oscillate because of spontaneous damping processes, afterwards they may reactivate. This temporal behavior gives rise to the presence of patches, and as we increase the control parameter more oscillators begin to oscillate taking part of a “contamination process”. These kind of phenomena are characteristic of spatially extended systems where weak coupling between oscillators is developed.

Regarding the diverging behavior of the invasion rate σ_{inv} which increases in the left branch of Fig. 3.19, we infer that as we increase the control parameter more oscillators are synchronized nearby ω_v according to an irregular clustering dynamics similar to many reaction-diffusion processes (i.e. Belousov-Zhabotinsky chemical reaction [122]). In consequence, the critical behavior of σ_{inv} might be considered as a diverging correlation length of this phase synchronization transition. Divergent critical behaviors agree qualitatively with the Ehrenfest theory (1933) of macroscopic thermodynamics (see Chapter 1) at a second order transition point, on the other hand according to Uzunov [27] divergent behaviors (i.e. the invasion rate) correspond to real finite jumps which cannot be quantified probably because of the finite experimental accuracy.

The spatiotemporal synchronization in the ST/ALT pattern as an inhomogeneous growth must be faced as a clustering process from a nonlocal coupling. Because the amplitudes of the critical modes are constant along this regime from the threshold, a phase equation could be enough to model this regime. Perhaps, the theoretical approach that best fits the experimental results would be a *mean-field theory* applied to a 1D-array of N -nonlocally coupled oscillators. Although, mean-field theory works fine with “phases” it does not work at critical points. There are new emerging theoretical models for these kind of regimes which are called *chimera states* (Abrams and Strogatz in 2004 [103, 138] from a numerical study on a ring of phase oscillators). These chimera states are able to go through regimes exhibiting coherent patterns in spatiotemporal chaos due to a phase synchronization process for

nonlocally coupled oscillators by means of a sinusoidal or a decaying exponential nonlocal kernel (Green function). The first theoretical results on these kind of spatiotemporal synchronization phenomena were reported recently by Shima, Tanaka and Kuramoto [139, 140] trying to explain spiral patterns arising from an ensemble of nonlinearly coupled oscillators with a decreasing exponential coupling responding to a nonlocal coupling. These theoretical models work with integrodifferential phase equations of the type:

$$\frac{\partial \phi}{\partial t} = \omega - \int G(x - x') \sin[\phi(x, t) - \phi(x', t) + \phi_o] dx'$$

where ω is the natural oscillators frequency, G is a Green function determining the nonlocal range of interaction, and ϕ_o is an initial phase shift.

From our experimental point of view, the reported synchronization phenomena implies the entrainment of the coupled oscillators in order to reach the cluster phase, this nonlinear coupling processes drives the oscillators to sustain small spatiotemporal delays that are allowed by the dynamics. In consequence, from a spatiotemporal chaos regime, close spatial and temporal frequencies give rise to coherent new patterns in space and time. In the spatiotemporal beating regime (ST/ZZ), coherent patterns in space emerge from the envelope of a beating wave, this is the kind of stationary nonlinear wave which is a stable solution of our dissipative and extended system. A model for the phase synchronization process in the ST/ZZ regime is proposed in the next chapter (Chapter 4). But there is still one relevant parameter to be taken into account in the cited models (from Kuramoto to Strogatz), we have shown in this chapter the decisive role of the amplitudes of the critical modes, which represent the real competition between modes. Thus, although the beating regime is driven far from the threshold, oscillators are able to cancel beats when their amplitudes are not strong enough, this fact is asking once again for coupled phase-amplitude equations.

Chapter 4

Spatiotemporal phase synchronization from nonlocal coupling

The leading motivation of this chapter is how to proceed in a far from the threshold phase analysis in order to understand the dynamics of a nonlinear 1D-system from the point of view of a “classical bifurcation”. Because the classical amplitude analysis is not possible, other approaches are necessary.

The following results for a shallow convective layer reveal that the secondary instability towards the spatiotemporal beating regime in the convective 1D-cell arise from *nonlocal* interactions between the convective cells or oscillating thermal units. These oscillators are spatially distributed on an extended array. Under weak coupling, these oscillators are similar to the limit-cycle oscillators studied by Winfree [5] and Kuramoto [105].

Thus, in this chapter we take up again the supercritical bifurcation from a state of spatiotemporal chaos (STC) towards a pattern with spatiotemporal order (ST/ZZ). These regimes exhibit respectively, irregular and stationary clusters of time-dependent patterns. These clusters consist of counter-propagative modes where the convective cells oscillate in counter-phase (*antiphase*) with their nearest neighbors, therefore coupling comes from attractive and repulsive forces between the cells. We develop a phase mismatch analysis between oscillators from the cross-correlated data, but restricting the model to the antiphase cross-correlation matrix which is built with regard to the critical frequencies. A condition of synchronization is imposed to the antiphase matrix for which above a threshold an oscillator belongs to the cluster of synchronization. From the antiphase matrix we measure the coherence of the system by defining a discretized order parameter.

A time-varying topology is deduced from the contact interactions of type I between oscillators which was defined in Chapter 2. The characteristic spatial scales are extracted from the cross-correlations at characteristic times defined by the link matrix. The coupling analysis in a sequence of measurements shows that the convective envelope (termed Δn) consists of 4-5 oscillators, more than a merely diffusive local coupling between oscillators in the cellular ST regime or between 3 oscillators in the STC regime.

4.1. Focus on phase synchronization in the spatiotemporal beating regime

In our quasi-1D-system, a phase synchronization transition enables the N -coupled convective cells to move toward a preferred direction. The common moving frame $\varkappa = x - v_\phi t$ defines this travelling wave regime with phase velocity $v_\phi = \omega/k$. We have already shown in Chapter 3, that for thick layers ($d \geq 4.5$ mm) the N -oscillators are synchronized in ω_v (or ω_{-v}) in the traveling wave regime (TW), where the N -oscillators array conform a coherent pattern which is an example of a perfectly correlated phase.

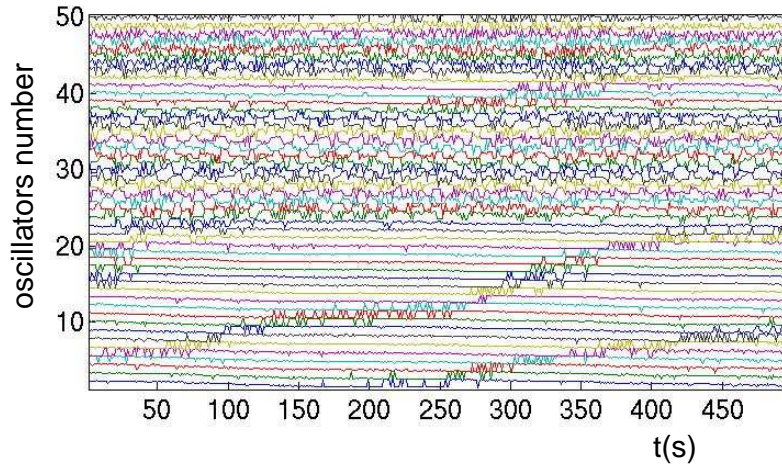


Figure 4.1: (a) Spacetime displacement of $N = 50$ oscillators at ΔT_{vc} .

For a constant depth $d = 3$ mm, as the control parameter ΔT_v is increased, the system undergoes through a “mixed pattern” which accomplishes with the requirements of a spatio-temporal chaos regime because spatio-temporal correlations decay. This STC regime is characterized by the presence of several irregular clusters. Oscillators belonging to this clusters exhibit an alternating pattern (ALT) [with wavenumber $k_s/2 \equiv k_v$ and frequency ω_v] coexisting with the basic ST pattern. We might consider that weak coupling can sustain these irregular clusters. From the coalescence of these various spreading phase subsystems the dynamics undergoes a supercritical bifurcation towards a new state of spatiotemporal beats (ST/ZZ). This ST/ZZ pattern is composed of two subsystems with stationary 1D-fronts and with high spatiotemporal coherence. It is characterized by a zig-zag geometry due to the splitting of the temporal frequency into (ω_v, ω_z) with $\omega_z \lesssim \omega_v$. Furthermore, a spatial frequency splitting into (k_v, k_z) is produced with $k_v \lesssim k_z$. In the ST/ZZ regime, a stronger coupling locks the phase into stationary clusters. Far from the threshold, this ST/ZZ regime calls for a phase description decoding the global information from the spatiotemporal diagrams $S_{y_o}(x, t)$ into a set of $N = 50$ discretized signals belonging to each oscillator. Each individual signal oscillates around its zero position (x_i): $X_i(t) = x_i + a_i \cos[\Psi_i(\phi_i^v, \phi_i^z, \phi_i^o)]$ [see Fig. 4.1] with a raw phase Ψ_i . Critical phases belonging to each oscillator ϕ_i^z are obtained by demodulation techniques applied for the critical frequency ω_z given by synchronized oscillators at a fixed ΔT_v . It should be stressed that the neighboring fundamental frequency ω_v which provides ϕ_i^v does not allow to characterize this bifurcation. Φ

is the cluster phase which slightly shifts from critical phases ϕ_i^z . The synchronization process is understood in terms of the individual phases ϕ_i^z regarding the cluster phase Φ by choosing a proper condition for synchronization which stands $|\phi_i^z - \Phi| \leq \Delta$. The spatial distribution of the oscillators in the array correspond to two very close wavenumbers k_v and k_z . More details on analysis techniques are explained in Chapter 2. In Fig. 4.2(a) we show a zoomed image of a spatiotemporal diagram in the ST/ZZ regime and the corresponding trajectories of the oscillators are shown in Fig. 4.2(b).

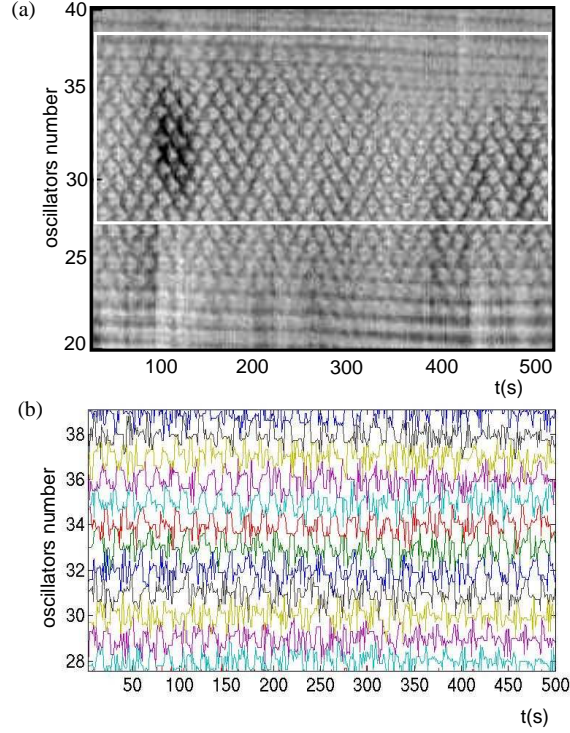


Figure 4.2: (a) Shadowgraphy image at $\Delta T_v = 32$ K; (b) trajectories of the oscillators tracked from the white frame in (a).

The following results correspond to the analysis of an ascending sequence in the range $\Delta T_v = [30, 35]$ K with step of 0.5 K, from the critical control parameter $\Delta T_{vc} = 31$ K the ZZ clusters appear supercritically as it is shown in Chapter 3. Further beyond, in the subsequent bifurcation towards ST/DW, a spatial desynchronization is produced remaining a unique domain in DW where the following traveling modes exist: $M_{\omega_{\pm}}(k_v, \pm\omega_z)$ and $M_{v_{\pm}}(k_v, \pm\omega_v)$.

4.1.1. Antiphase cross-correlation matrix

The starting point in the following sections is the discretized signal $X_i(t)$ obtained for $N = 50$ oscillators. We transform these signals using 1D-FFT in order to find the fundamental frequencies. The typical frequency spectrum corresponding to two synchronized oscillators is shown in Fig. 4.3(a), the critical frequency ω_z guides the instability towards the synchronized ST/ZZ pattern. Oscillators belonging to a cluster domain have in common the same frequency: ω_{Φ} . This frequency can be obtained by averaging the oscillators frequencies ω_i^z belonging to the cluster [see Fig. 4.3(b)].

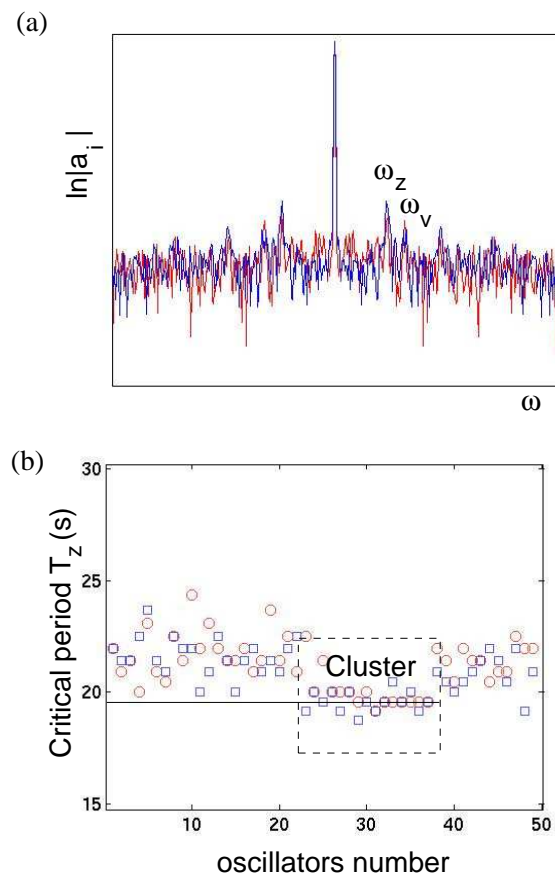


Figure 4.3: (a) Frequency spectrum (with $\ln(|A|)$) for two synchronized oscillators ($i=30,32$) belonging to the cluster, ω_z is the critical mode and ω_v is a fundamental mode still remaining from the previous state; (b) critical period distribution $T_z = 2\pi/\omega_z$ obtained by demodulating two different patterns with the presence of a cluster near and above the threshold of the ST/ZZ regime.

In Fig. 4.4 we show the frequency distribution along the oscillators array using demodulation techniques applied into two different synchronized patterns corresponding to the extremes of the sequence in the ST/ZZ regime, at the threshold ($\Delta T_v = 31$ K) and below the next instability ($\Delta T_v = 34.5$ K). Discontinuous jumps close to the clusters domain belong to desynchronized oscillators. Oscillators belonging to the cluster display an increasing frequency with temperature: $\omega_\Phi = 0.32$ s⁻¹ ($\Delta T_v = 31$ K) and $\omega_\Phi = 0.34$ s⁻¹ ($\Delta T_v = 34.5$ K).

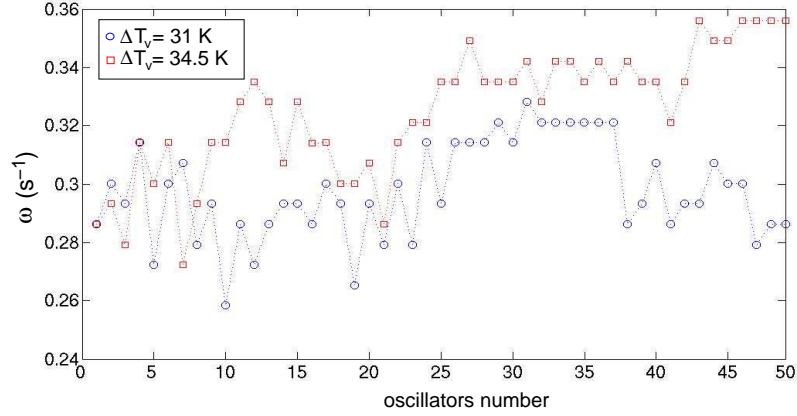


Figure 4.4: Distribution of frequencies in the array at $\Delta T_v = 31$ K and $\Delta T_v = 34.5$ K. The selected frequencies to implement the analysis technique are $\omega_z = 0.329$ s⁻¹ and $\omega_z = 0.336$ s⁻¹, respectively.

The study of phases instead of frequencies allows us to study the degree of coupling between oscillators. Raw phases Ψ_i are demodulated at the critical frequency ω_i^z choosing a suitable low-pass filter (a Butterworth filter) in order to reconstruct the critical phases ϕ_i^z for $i = 1, \dots, N$ [Fig. 4.5(a)].

From these phases, we show in Fig. 4.5(b) the critical phases belonging to two neighboring oscillators which are phase synchronized. To extract information about the phase mismatch between their respective cosine signals [Fig. 4.5(c)] we work with the cross-correlation function $\mathcal{C}_{ij}(\omega_z, \tau_l)$ [Fig. 4.5(d)]. The *phase cross-correlation vector* between each ij -pair is expressed as:

$$\mathcal{C}_{ij}(\omega_z, \tau_l) = \langle \cos(\phi_i^z), \cos(\phi_j^z) \rangle \quad (4.1)$$

where τ_l are time lags (more details are found in Chapter 2). The meaning of time lag is easily grasped from the idea that a couple of antiphase oscillators take a minimum time lag of $T/2$ (T period of an oscillation) to collapse.

The last step is to analyze cross-correlations between $N \times N$ oscillators. Thus, we build the *inphase* \mathcal{I}_{ij} and *antiphase* \mathcal{A}_{ij} matrices (see Fig. 4.6):

$$\begin{aligned} \mathcal{I}_{ij}(\omega_z) &= \max_{\tau_l} \mathcal{C}_{ij}(\omega_z, \tau_l) \\ \mathcal{A}_{ij}(\omega_z) &= \min_{\tau_l} \mathcal{C}_{ij}(\omega_z, \tau_l) \end{aligned}$$

From the overall experimental measurements, synchronized oscillators in \mathcal{A}_{ij} show a stronger correlation than in \mathcal{I}_{ij} , this means that the absolute values of the minima of the cross-correlation

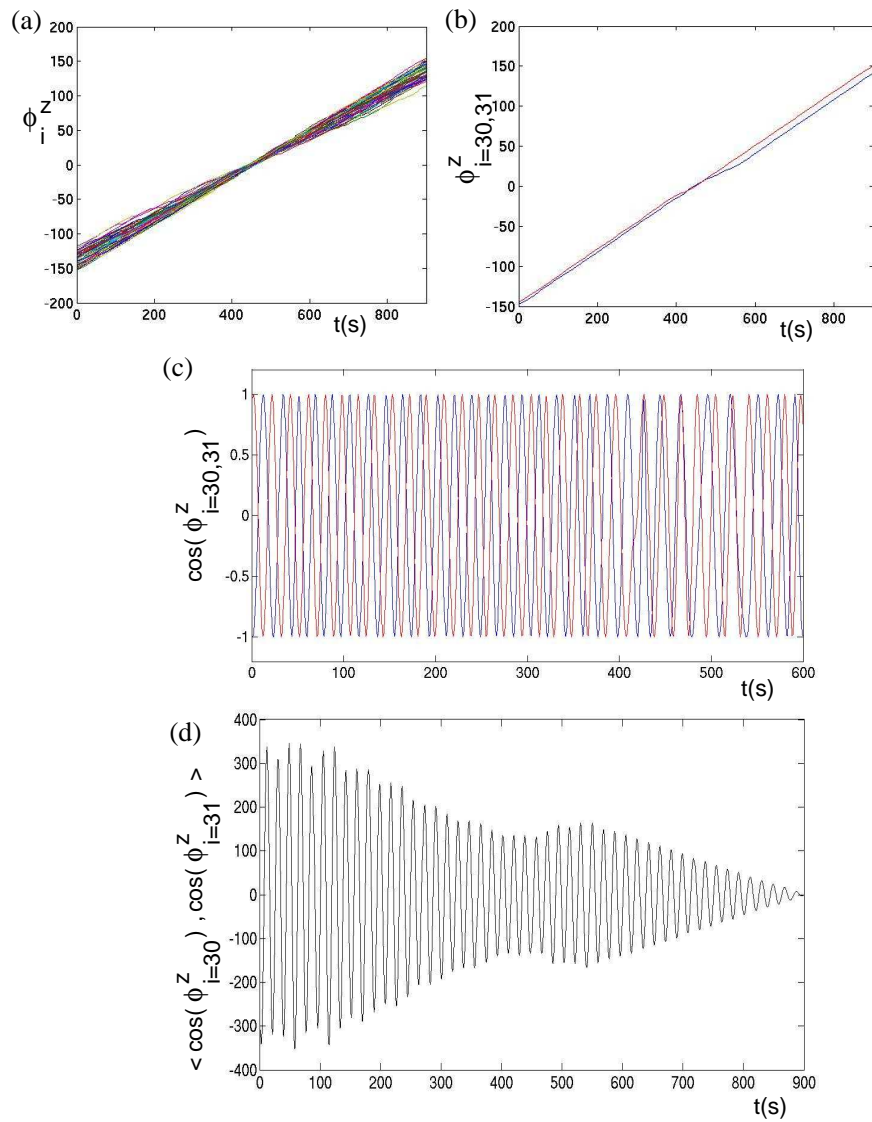


Figure 4.5: (a) Critical phases ϕ_i^z of the whole array above the threshold $\Delta T_v = 32$ K; (b) critical phases ϕ_i^z for two synchronized oscillators $i = 30, 31$ from (a); (c) cosine function of ϕ_i^z for $i = 30, 31$; (d) phase cross-correlation vector $\langle \cos(\phi_{30}^z), \cos(\phi_{31}^z) \rangle$.

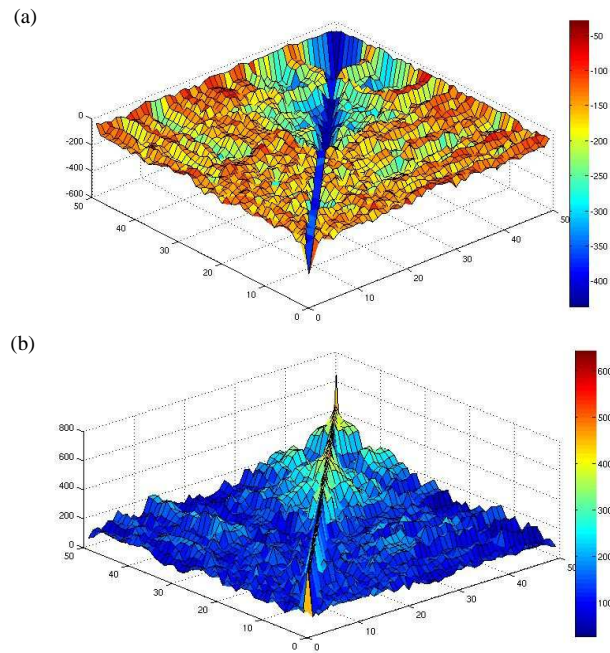


Figure 4.6: Far from the threshold at $\Delta T_v = 34.5$ K: (a) surface graph of the antiphase matrix $\mathcal{A}_{ij}(\omega_z)$; (b) surface graph of the inphase matrix $\mathcal{I}_{ij}(\omega_z)$.

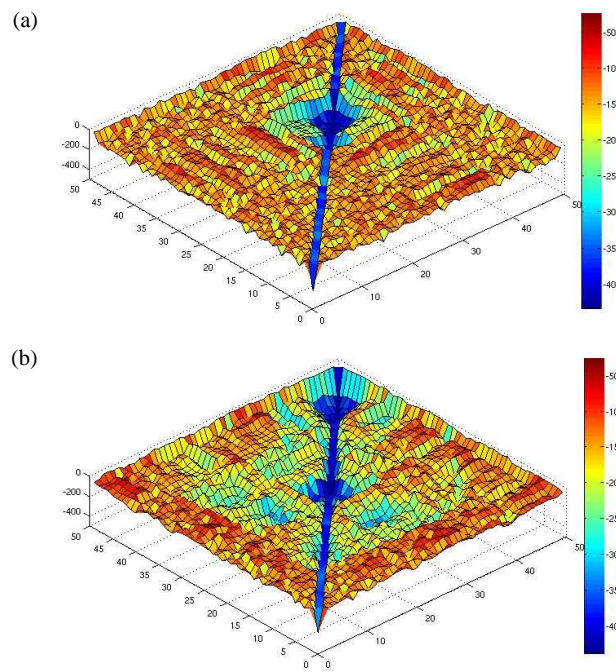


Figure 4.7: Surface views of the antiphase correlation matrices $\mathcal{A}_{ij}(\omega_z)$ at (a) $\Delta T_v = \Delta T_{vc} = 31$ K; and (b) $\Delta T_v = 34$ K.

vectors $\mathcal{C}_{ij}(\omega_z, \tau_l)$ are greater than the maxima [see Fig. 4.6]. This fact allows us to understand coupled oscillators inside ZZ clusters as the kind of antiphase oscillators. This antiphase pattern, as well as the previous domains in the ALT pattern and the subsequent ST/DW pattern, arise from attractive-repulsive forces between oscillators. Surface images obtained from the antiphase matrix in Fig. 4.7 are depressed in regions with the higher phase synchronization between oscillators, these regions correspond to clusters of synchronization. The two phase synchronization clusters, in the ST/ZZ regime, emerge because of the spatial beating phenomena. In a sequence of measurements in the ST/ZZ regime, the analysis of the antiphase matrix applied to noncritical modes $\omega = \omega_v$ does not contribute to any qualitative information about the transition as we have indicated before.

Phase shifts between two adjacent oscillators $\{i, j\}$ are computed as *period shifts*:

$$\tau_{m,i} \equiv \tau_{m,j} \pmod{T_z}$$

module $T_z = 2\pi/\omega_z$ where τ_m is the lag time at the minimum cross-correlation (maximum correlation of antiphase oscillations), hence $\mathcal{C}_{ij}(\omega_z, \tau_m) = \min_{\tau_l} \mathcal{C}_{ij}(\omega_z, \tau_l)$ within a sufficient margin error of 2 s. This means that inphase oscillators have null phase shifts, meanwhile antiphase oscillators compute with phase shifts within the critical period range $T_z \pm 2s$. Graphs in Fig. 4.8(a-c) show an increasing number of antiphase oscillators which is translated into a more coherent behavior of the collectivity. From an irregular distribution of phase shifts below the threshold at $\Delta T_v = 30$ K [Fig. 4.8(a)] towards a more regular antiphase distribution along the cluster domain at threshold [Fig. 4.8(b)], and far from the threshold [Fig. 4.8(c)]. As it is expected, in the graphs $\tau_{m,i}$ diminishes as ΔT_v is increased.

However, it is more difficult to recover the number of synchronized oscillators from period shifts than from the analysis we explain later on in order to obtain a discrete order parameter $\mathcal{Z}(\omega_z)$ from the antiphase matrix.

4.2. A global bifurcation

In Chapter 2 we introduced the *correlation time* τ_c which fulfills $|\mathcal{C}_{ij}(\tau_c)| = |\mathcal{C}_{ij}(\tau_l = t_f)|/e$, where $|\mathcal{C}_{ij}(\tau_l = t_f)|$ is the maximum value of the cross-correlation vector at zero lag. A global synchronization instability is shown from the average correlation time $\langle \tau_c \rangle$ in Fig. 4.9(a). The assigned average value $\langle \tau_c \rangle$ for each control parameter value is obtained from the correlation times over the whole array. In Fig. 4.9(b) we show the distribution of correlation times for three representative control parameter values. Far from the threshold at $\Delta T_v = 34.5$ K, τ_c reaches the maximum recording time for almost all the oscillators in contrast to the values obtained below the threshold at $\Delta T_v = 28$ K. Clearly, at threshold ΔT_{vc} the oscillators belonging to the cluster show the longest correlation times [Fig. 4.9(b)].

From the information given by the antiphase matrix, we may obtain the *antiphase cross-correlation N-vectors*: $\mathcal{A}_i(\omega_z) = \mathcal{A}_{i1}(\omega_z), \mathcal{A}_{i2}(\omega_z), \dots, \mathcal{A}_{ii}(\omega_z), \dots, \mathcal{A}_{iN}(\omega_z)$, where the *ii*-element is the self-correlation. For example, in Fig. 4.10(a-c) each graph shows three cross-correlation vectors corresponding to oscillators localized outside, at the border and inside the cluster. We might infer from these graphs the type of the coupling interaction between oscillators at the boundaries and oscillators inside the cluster. In Fig. 4.10(a) the interaction range corresponds to

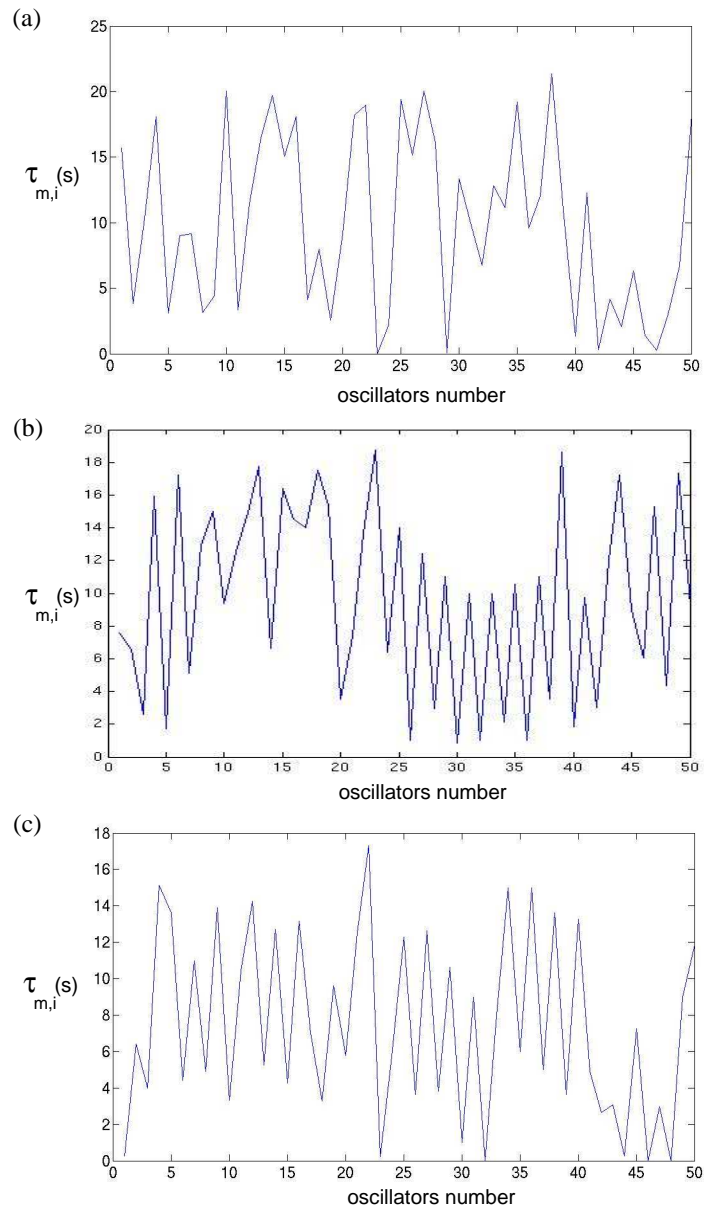


Figure 4.8: Period shifts $\tau_{m,i}$ between oscillator $i = 31$, which is becoming synchronized, and the rest at (a) $\Delta T_v = 30$ K; (b) $\Delta T_v = 31$ K; (c) $\Delta T_v = 34.5$ K.

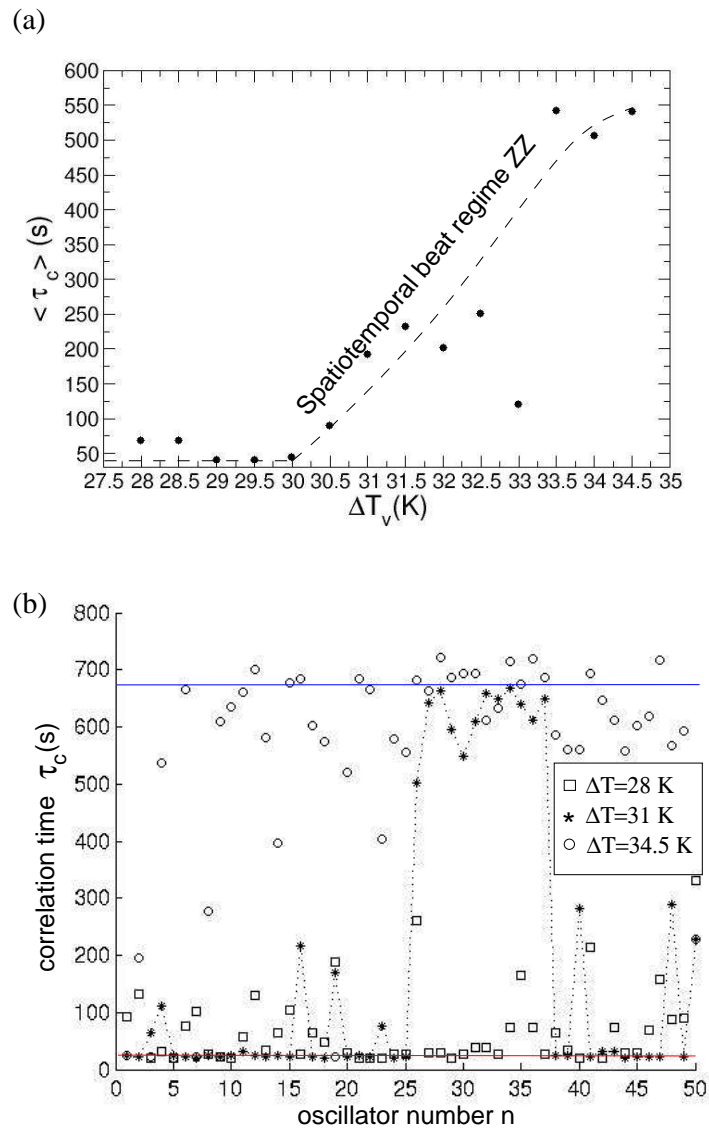


Figure 4.9: (a) Average correlation time $\langle \tau_c \rangle$ vs ΔT_v where the dashed line is a guide to the eye; (b) correlation time τ_c for each oscillator at $\Delta T_v = 28, 31$ and 34.5 K. Top and bottom solid lines represent the maximum and minimum correlation times, dotted lines at $\Delta T_v = 31$ K are a guide to the eye.

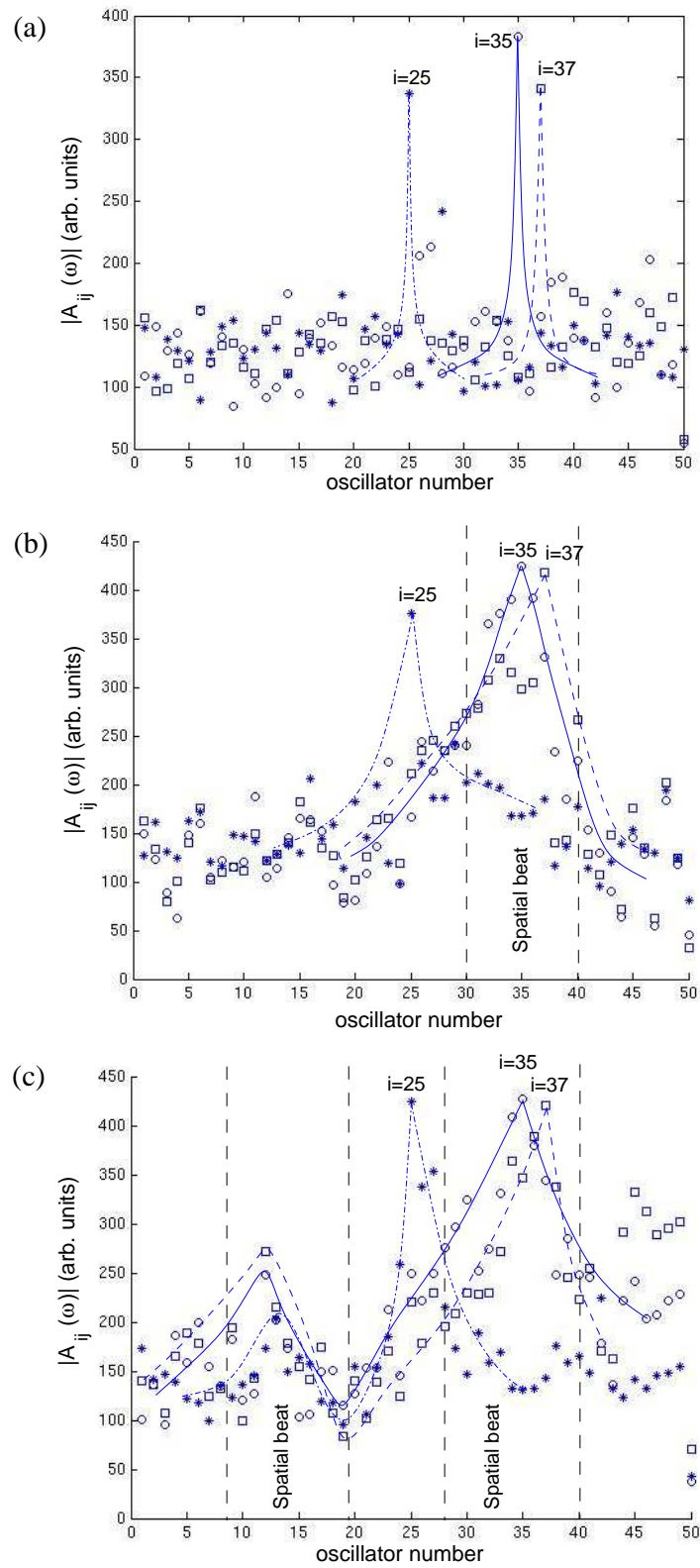


Figure 4.10: Antiphase cross-correlation vectors $\mathcal{A}_{ij}(\omega_z)$ ($j = 1, \dots, N$) for oscillators $i = 25, 30$ and 37 at: (a) $\Delta T_v = 28$ K; (b) $\Delta T_v = 31$ K; and (c) $\Delta T_v = 34.5$ K. Solid and dashed lines are a guide to the eye. Vertical dashed lines define the cluster domain.

the previous regime ST/ALT. In Fig. 4.10(b), it is shown that for a distant oscillator from the cluster, the antiphase cross-correlation decays with a steeper slope than for oscillators belonging to the cluster, as it is expected from a diffusive coupling of the type $\mathcal{A}_{ij}(\omega_z) \sim e^{-\beta x}$ (short interaction range). Meanwhile, for the remaining oscillators belonging to the cluster, the antiphase cross-correlation has a smoother decay. This fact should be interpreted as the consequence of a larger interaction range, therefore we observe from Fig. 4.10(b,c) that the convective envelopes involve at least 4 or 5 oscillators. If we evaluate the interaction range in the overall ascending sequence (in the ST/ZZ regime), we infer that clusters might be sustained by a stronger nonlinear coupling between oscillators that is responsible for a larger interaction range. At threshold, in Fig. 4.10(b), we observe how the stronger coupling becomes already evident. These last results might allow us to determine an effective nonlocal interaction range $\Delta n > 3$ oscillators from the antiphase matrix. Nevertheless, the topology (link matrix) provides more accuracy in determining Δn , as it will be shown in a later section, from the colliding positions between oscillators.

4.3. A discrete order parameter

In our 1D-array, a critical phase ϕ_i^z emerges at the threshold of the synchronization transition which allows to build the antiphase matrix $\mathcal{A}_{ij}(\omega_z)$. From this matrix, a new order parameter is defined $\mathcal{Z}(\omega_z)$ which quantifies the range of interaction between synchronized oscillators, or equivalently, the number of synchronized oscillators conforming a cluster. To quantify $\mathcal{Z}(\omega_z)$ a condition of synchronization must be imposed. The true spatial extension of a cluster domain can be calculated from $\mathcal{Z}(\omega_z) \times 6.25$ mm which corresponds to the length of the cluster. Under a symmetric and bidirectional coupling, $\mathcal{Z}(\omega_z)$ is computed along one direction testing each oscillator with regard to its neighbor.

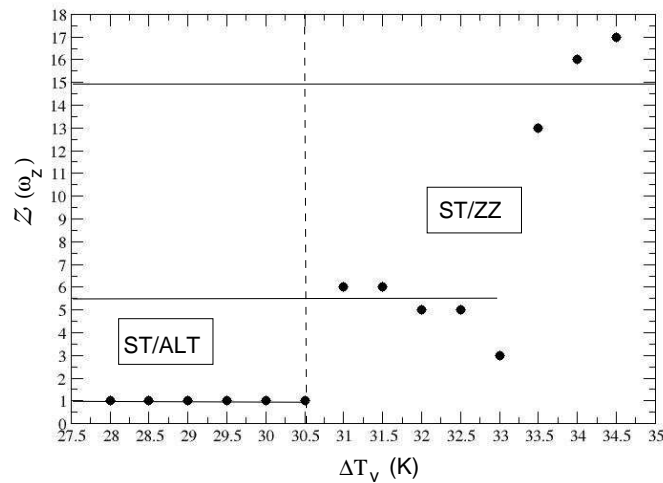


Figure 4.11: Order parameter values $\mathcal{Z}(\omega_z)$ for the ascending sequence. The vertical dashed line split two different regimes. Horizontal solid lines show average values of the number of oscillators involved in clusters.

The order parameter $\mathcal{Z}(\omega_z)$ is obtained as the maximum number of synchronized oscillators in the array. Firstly, it is necessary to compute on the array the local parameter $\mathcal{Z}_i(\omega_z)$, which gives the number of oscillators highly correlated to a given i -oscillator. A synchronization condition is applied to the ij -elements of the antiphase matrix $\mathcal{A}_{ij}(\omega_z)$ defining a threshold ϵ , in Fig. 4.7(a,b) $|\epsilon| = 200$, which is the sufficient condition to guarantee phase locking between neighboring oscillators along this sequence. Then,

$$\mathcal{Z}_i(\omega_z) = \sum_{j=i+1}^{\eta \leq N} f_{ij}, \text{ where } f_{ij} = \begin{cases} 1 & \mathcal{A}_{ij}(\omega_z) < \epsilon \\ 0 & \mathcal{A}_{ij}(\omega_z) > \epsilon \end{cases} \quad (4.2)$$

From the obtained results, we have noticed that values of the local parameter $\mathcal{Z}_i(\omega_z)$ for an oscillator belonging to the right-cluster evolve more smoothly than for an oscillator belonging to the left-cluster, this is in fact caused by turbulent critical amplitudes and because the spatial frequency splitting induces the formation of a third cluster. Therefore $\mathcal{Z}_i(\omega_z)$ depends on both the phase and the amplitude of the critical modes.

The number of synchronized oscillators is defined by $\mathcal{Z}_i(\omega_z) = \eta < N$ for $i = 1, \dots, N$ and agrees with the number of oscillators yielding high correlation time values τ_c . The global order parameter $\mathcal{Z}(\omega_z)$ is obtained as:

$$\mathcal{Z}(\omega_z) = \max_i \mathcal{Z}_i(\omega) \quad (4.3)$$

From Fig. 4.11, we observe that although the frequency is a monotonically increasing function with temperature $\omega_z(\Delta T_v)$, as we reported in Chapter 3, the global parameter $\mathcal{Z}(\omega_z)$ is not a continuous function of ΔT_v because from $\Delta T_v > 33$ K upwards, three clusters appear with closer fronts. In the ST/ALT pattern a maximum value of $\mathcal{Z}(\omega_z) = 1$ is translated into packages of 3 weakly coupled oscillators. Far from threshold, 15-17 oscillators are coupled whereas in between $31 \text{ K} < \Delta T_v < 33 \text{ K}$ the approximate number of synchronized oscillators is 5. At $\Delta T_v = 33 \text{ K}$, the order parameter and average correlation time are affected by a decreasing amplitude of the critical mode, like a spontaneous desynchronization process.

4.4. Topology from the rewiring connections

In this section we are going to deal with some topological aspects which are a consequence of the antiphase nature of oscillations. Such topological properties are obtained from the geometric loci that correspond to colliding oscillators. At each colliding position a couple of oscillators interact. We study only this kind of loci defined to have connectivity type I (see Fig. 4.12). The topology of contact loci is shown in the *link matrix* L_{ij} which is only nonzero at these contact loci. In Fig. 4.13(a,b) we show two link matrices at the extreme values of ΔT_v in this regime. The analysis of the topology by means of the link matrix provides the dynamics of the rewired connections along the sequence of measurements.

If we integrate L_{ij} over time for oscillators belonging to the cluster, and then apply running averages with a period (averaging time interval) equal to half the periodicity of the temporal beating ($t=62$ s), we obtain graphs similar to those in Fig. 4.14 where the values of the running averages correspond to the degree of linking in the cluster along time. We observe, as it was

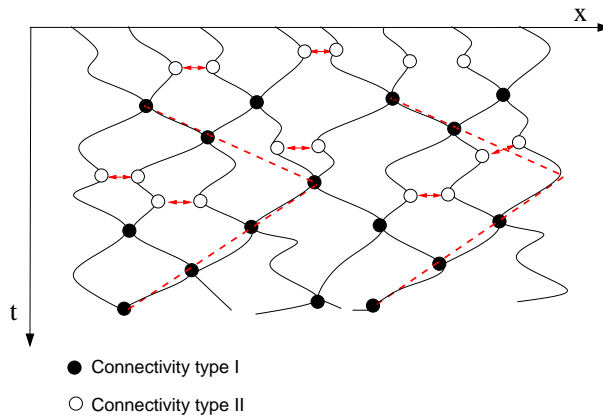


Figure 4.12: Sketch of the trajectories of a few oscillators inside a ZZ cluster. Black filled circles indicate the contact interaction loci (connectivity type I), empty circles indicate the minimum distance between attracting oscillators without collision (connectivity type II). Dashed lines are a guide to the eye showing the observed characteristic zig-zag (ZZ) pattern associated to temporal beats.

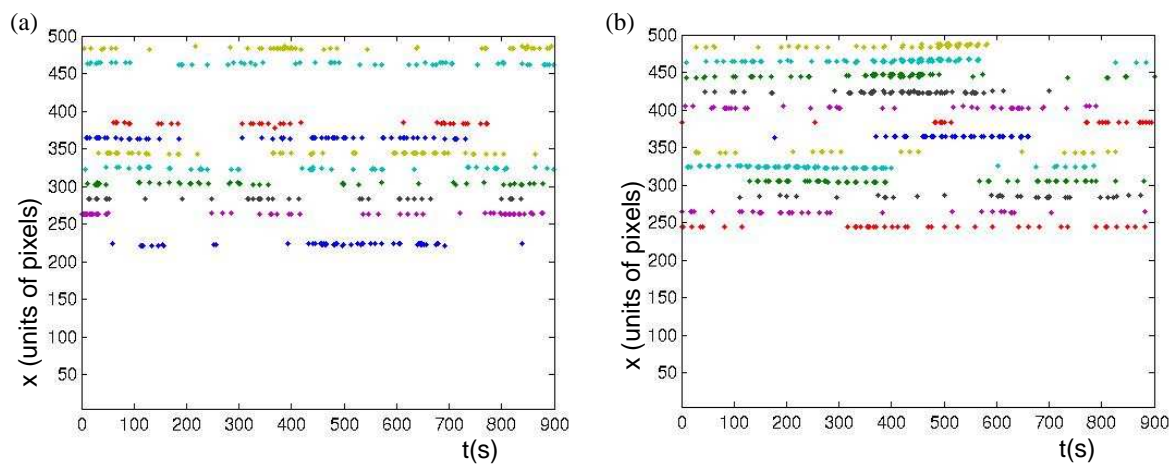


Figure 4.13: Link matrices L_{ij} generated by contact interactions between oscillators are shown in pictures at: (a) $\Delta T_v = \Delta T_{vc} = 31$ K; and (b) $\Delta T_v = 34$ K.

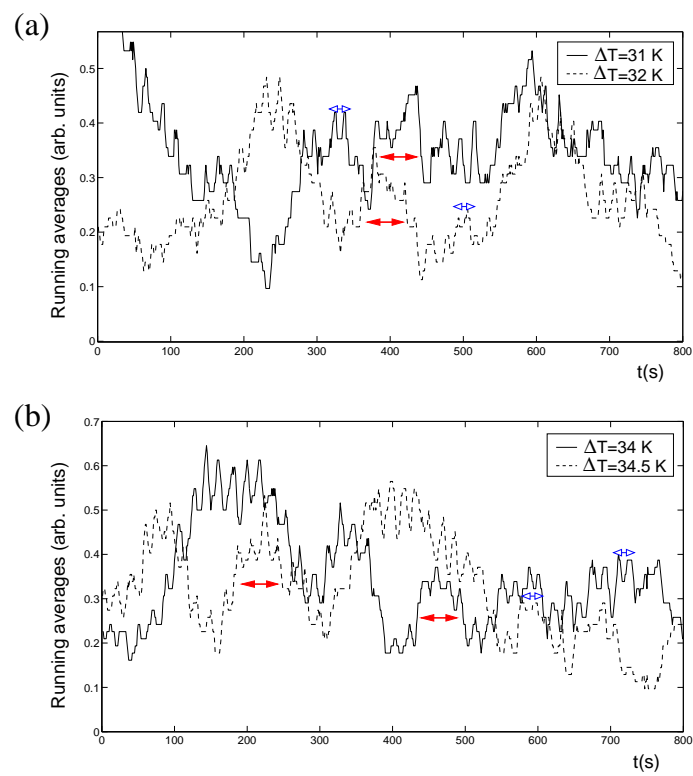


Figure 4.14: (a) Running averages over 62 seconds of the link matrix L_{ij} at $\Delta T_v = 31, 32$ K; (b) running averages over 62 seconds of the link matrix L_{ij} at $\Delta T_v = 34, 34.5$ K. Red and blue doubled arrows show the temporal beats (envelope wave) period and the internal wave (carrier wave) period respectively.

expected, that the characteristic time scales (the oscillators periodicity and the beats periodicity) are recovered. From these graphs we determine the times of maximum and minimum linking.

If we look for the effect of topology on dynamics, from the data of the running averages we determine times of minimum linking t_m and times of maximum linking t_M . Next, we go back to cross-correlations between oscillators and calculate the *cross-correlation N-vector* (cross-correlations between the N -oscillators) at time $t_{m,M}$:

$$\mathcal{C}_{ij}(\omega_z, \chi_l) = \langle \cos(\phi_i(t_{m,M})), \cos(\phi_j(t_{m,M})) \rangle \quad (4.4)$$

where χ_l is the oscillators lag with $\chi_l = 1, \dots, N$. Maximum values of $\mathcal{C}_{ij}(\omega_z, \chi_l)$ take place at values of the oscillators lag which represent the number of correlated or synchronized oscillators. At maximum linking, the cross-correlation vector $\mathcal{C}_{ij}(\omega_z, \chi_l)$ behaves as it is shown in Fig. 4.15(a). We study the envelope of $\mathcal{C}_{ij}(\omega_z, \chi_l)$ taking the absolute value: (i) at minimum linking it shows the maximum correlation at 4-5 oscillators [Fig. 4.15(b)] with low peaks centered on the clusters size (13-17 oscillators belonging to the clusters); (ii) at maximum linking it shows a maximum correlation at the cluster size (15-18 oscillators) [see Fig. 4.15(c)]. Certain graphs, like in Fig. 4.15(d), show the maximum correlation over roughly 4 oscillators.

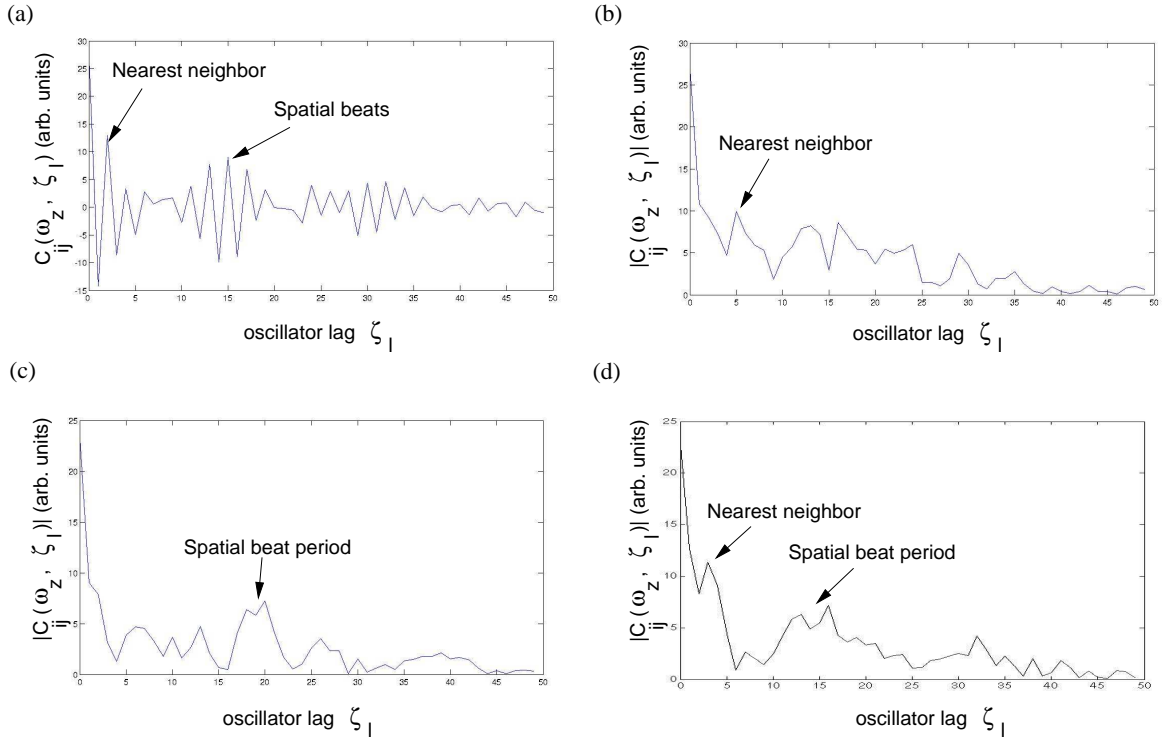


Figure 4.15: (a) Cross-correlation $\mathcal{C}_{ij}(\omega_z, \chi_l)$ at time of maximum linking $t_M = 404$ s for $\Delta T_v = 34.5$ K. Modulus of the cross-correlation $\mathcal{C}_{ij}(\omega_z, \chi_l)$: (b) at minimum $t_m = 100$ s for $\Delta T_v = 33.5$ K; (c) at maximum $t_M = 797$ s for $\Delta T_v = 34.5$ K; (d) at maximum $t_M = 61$ s for $\Delta T_v = 33.5$ K.

These results support the following conclusions:

1. For the phase synchronization transition in the ST/ZZ regime, the dynamics determine the rewiring of connections.

2. Nonlocal coupling goes beyond first neighbors ($\Delta n > 3$), differing from the kind of coupling that it was shown below the threshold of the ST/ZZ regime in Fig. 4.10(a) for $\Delta n = 3$. In the ST/ZZ regime, because the interaction range is larger we expect nonlinearly coupled groups of at least $\Delta n = 4 - 5$ oscillators.

4.4.1. Modelling a time-varying topology

We have shown that a dynamics of the rewiring of connections exits from the analysis of the time-dependent link matrix L_{ij} . This evolving topology of the network is related to the dynamics of beats in the phase synchronization regime ST/ZZ. In the framework of *Networks* for nonlocal coupling between oscillators sustaining attractive-repulsive interactions an affordable phase model might be the following:

$$\dot{\phi}_i = F_i(\phi_i^z, \phi_i^v, \dots, \phi_i^o) + \sum_{j=1}^N H_{ij}(t) \cdot \Gamma_{ij}(\phi_i - \phi_j) \quad (4.5)$$

where F_i is in charge of the dynamics of individual oscillators. The coupling function between oscillators is $\Gamma_{ij}(\phi_i - \phi_j)$ which comes from a slow perturbation (e.g. with $\Gamma_{ij}(\phi_i - \phi_j) \simeq \sin(\phi_i - \phi_j)$ [141]). The time-dependent connectivity function is the adjacency matrix $H_{ij}(t) = M_{ij} \cdot G_{ij}(t)$ which provides the linking between oscillators. From Δn (given by the analysis of the running averages over the link matrix integrated in time) we can obtain an adjacency matrix at zero time $M_{ij}(0)$ such that $M_{ij} = 1$ if $|i - j| \geq \Delta n$, and $M_{ij} = 0$ otherwise. The dynamics is introduced in the time-dependent connectivity matrix $G_{ij}(t)$ whose nonzero elements are extracted from the linking matrix. So, for a given asymptotic state L_{ij} might be mapped into $G_{ij}(t)$. Nevertheless, the coupling function in the ST/ZZ regime might have a more complex behavior as far as we get from the threshold, consequently it might also depend on the control parameter $\Gamma_{ij}(\phi_i - \phi_j, \Delta T_v)$. Furthermore, Γ_{ij} might include a desynchronization condition which might depend on the amplitudes of the critical modes $A_{z\pm}$ introducing a coupled amplitude equation.

4.5. Discussion and conclusions

The most striking feature of these results is that a dynamical system achieves a global bifurcation from a nonlocal coupling. Mean correlation time diverges for the whole oscillators array and not only for the oscillators belonging to the cluster. According to standard definition of synchronization, we may assert that a global synchronization transition has developed from a clustering synchronization process. On the other hand, nonlinearities sustain coherent patterns against developed turbulent states. As a matter of fact, nonlinearities might work as a feedback mechanism for dissipative systems, this means that without forcing oscillations would be damped; this forcing comes from the constantly supplied energy into the oscillators by heating ΔT_v .

Phase synchronization in our system concerning the increasing trend of the synchronization frequencies (also it is inferred from phase shifts between oscillators) shares with other numerical systems (simulations on nonlinear coupled oscillators) that, as we increase the control parameter, oscillators belonging to cluster, with higher frequencies of oscillation, drag the rest towards the same frequency of synchronization.

Another important point of discussion is that the increasing number of nonlinearities, from ST/ZZ to ST/DW, does not necessarily account for a really strong coupling. That is why weak coupling revealed by the cross-correlation techniques is valid along the sequence and it is responsible for the synchronization mechanisms. It is above the ST/DW instability that the system starts a desynchronization process which is supposed to happen when coupling is no longer weak.

A new order parameter $\mathcal{Z}(\omega_z)$ is obtained from the cross-correlations between the critical phases (ϕ_i^z) and it is of the order of the spreading size of the new synchronized phase. This order parameter is equivalent to the KM expression: $\sigma = N^{-1} \sum_{j=1}^N e^{i|\phi_j - \Phi|}$.

The diffusive coupling in the ensemble of N -hotspots or latent chaotic elements is local over the whole phase chaos scenario, further on the coupling becomes nonlocal. If the range of interaction had been supposed to be all-to-all, then, when the system had sustained a local perturbation we would have found an instantaneous propagation over the whole array which is not the case. In this sense, the globally coupled map (GCM) theory (nearby mean-field theory) is not suitable to explain the spatiotemporal chaos from weak coupling in our high-dimensional system. The range of interaction between oscillators is given by $\Delta n \approx 4-5$ which might be considered as a correlation length of the system ξ . There is a connection between the correlation length ξ of coexisting domains determined from the global analysis in Chapter 3 and a wider convective cell involving Δn oscillators obtained from a discretized study because we have found that $\xi \sim \Delta n \approx 30$ mm.

Although the supercritical bifurcation towards the ST/ZZ regime has been determined from the amplitude analysis of the critical modes, a phase description is suitable along this regime. But it might not necessarily hold for any regime far from the first instability because, according to the reported results here, there are couplings between the amplitude and the phase. We have shown that synchronization between oscillators is revealed from the critical mode ω_z satisfying a synchronization condition to belong to the cluster, but reasonably its amplitude might be sufficient to trigger synchronization. When this critical mode ω_z is missing the rewiring connections are produced by the unstable mode ω_v which might be leading the STC regime (or mixed ST/ALT pattern) from a diffusive and local coupling in the stationary cellular pattern (ST).

Chapter 5

Thermocapillary instabilities in a cylindrical cell

In this chapter we report the study of waves in a thin 2D-fluid layer with low viscosity ($\nu = 0.65$ cSt) and *intermediate* Prandtl number ($Pr = 10$). The experimental measurements were performed in February 2004 in the condensed matter physics laboratory at the research center of CEA-Saclay under the supervision of Nicolas Garnier, Arnaud Chiffaudel, François Daviaud and Javier Burguete. The fluid layer under study is contained in cylindrical cell where convection is reached by controlling the radial temperature gradient between the center which is an inner cylinder and the outer rim. We build the stability diagram and visit the dynamics of each regime for *deep* layers $d = [2.20, 5.55]$ mm. The work of R. Krishnamurti [142] for silicone oils in the route towards turbulence, show that for small Prandtl numbers ($Pr < 10$) several contiguous regimes converge inside a narrow region of the stability diagram, this fact sets a difference in comparison with the rectangular 1D-cell for $Pr = 75$.

One of the most distinguishing features of the reported 2D-dynamics is the appearance of hydrothermal waves following positive temperature gradient. This has already been shown by a previous experimental work developed with the same cell by Garnier [28, 63], but for thinner layers $d = [1.2, 1.9]$ mm. Negative temperature gradients were also explored for the same depths.

Particularly, in this chapter we analyze the transitions that take place when the inner cylinder is heated in order to find out parallelisms with the 1D-cell dynamics. We analyze quantitatively two subsequent bifurcations towards a traveling wave pattern (TW) and an alternating pattern (ALT). Besides, we report the phenomenology of the *flower-like pattern* (FL) which becomes unstable by breaking the continuous azimuthal symmetry, and the *hydrothermal wake-waves* (HWW) which emerge further from the FL pattern.

One of the most relevant aspects in a polar system is the different local curvature from inner to outer radial positions. This condition is closer to real systems like crystal growth, as well as melting and solidification processes of liquid metal experiments in cylindrical vessels, in contrast with experiments performed in rectangular cells for low Prandtl numbers. Concerning these applications, there is a brand-new interest in studying instabilities in cylindrical fluid layers in both experiments [143] and simulations [143–146].

5.1. Introduction

Thermocapillary convection in a cylindrical layer, for high depths, under a radial temperature gradient ($\vec{\nabla}_r T$) may be reached due to hydrothermal and Bénard-Marangoni mechanisms. Under these circumstances two kinds of wave-phenomena are observed: hydrothermal waves (HW) and thermal waves like traveling waves (TW) or alternating waves (ALT). Vertical interface displacements caused by surface waves have not been identified in this system.

In the cylindrical system of Fig. 5.1 there is a radial temperature gradient between the inner core (T_{int}^-) and the outer ring (T_{ext}^+) with $T_{ext}^+ > T_{int}^-$. Natural polar components of wave vectors $\vec{k} = (k_r, k_\theta)$ (\hat{r} and $\hat{\theta}$ represent the radial and the azimuthal directions) are associated to each fundamental mode and transformed, for convenience, into Cartesian components given at a distance $r = r_o$ from the border of the central core by: $\vec{k} = k_r \hat{r} + k_\theta(r_o) \hat{\theta}$. To extract the wave information (amplitudes, wave numbers and frequencies) we have developed demodulation techniques by means of 2D-FFT in order to analyze spatiotemporal diagrams and unrolled images from polar to Cartesian coordinates.

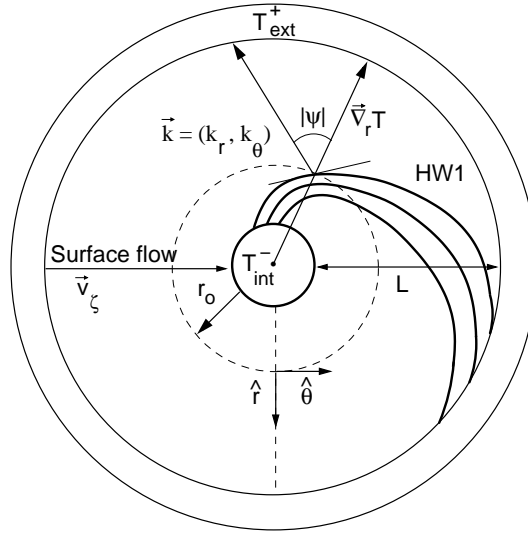


Figure 5.1: Sketch of the upper view of the cylindrical cell with a radial temperature gradient $T_{ext}^+ > T_{int}^-$. A spiral pattern with three arms (HW1) is sketched close and above the threshold, and relevant magnitudes: $\psi = (\vec{k}, \vec{\nabla}_r T)$ is the angle of propagation and \vec{v}_ζ is the downstream surface velocity. Polar coordinates $(\hat{r}, \hat{\theta})$ are defined at any radius $r = r_o$ from the border of the inner core.

In this chapter we present an overview of the dynamics for high depths $d = [2.20, 5.34]$ mm taking as the departing point previous results for depths $d = [1.2, 1.9]$ mm [28, 63]. We find previous experimental work in annular cells with radial thermal gradients [61], and with localized central heating over the free surface [147].

5.1.1. Hydrothermal waves in a cylindrical cell

Hydrothermal waves (HW) propagate following the direction of the positive temperature gradient, from T^- to T^+ . The direction of HW is defined by the angle ψ between the wave vector

\vec{k} and the radial temperature gradient direction $\vec{\nabla}_r T$. For small Prandtl numbers ($Pr < 1$) both vectors are perpendicular, $\psi \approx 90^\circ$, meanwhile for $Pr > 10$ both vectors are quasi-colinear (see instability mechanisms of hydrothermal waves in Chapter 1), $\psi \approx 0^\circ$, for intermediate values $0 < Pr < 10$ oblique waves are expected with $0^\circ < \psi < 90^\circ$. If we consider a cylindrical fluid layer subjected to a radial temperature gradient in the cell of Fig. 5.1 with $\vec{\nabla}_r T > 0$, heating the outer ring where $\Delta T_r = T_{ext} - T_{int}$, a basic flow appears like a flattened torus. The surface flow with velocity \vec{v}_ζ moves streamwise along L in the \hat{r} direction towards the inner core. In Fig. 5.1 we show three emerging waves, these hydrothermal waves are the kind of spiral waves that appear at the onset of HW1 instability. For very small radii the wave vector of HW1 is quasi-1D because it grows perpendicular to the inner core (radial wave vector), and immediately it achieves the maximum local curvature ($\Gamma_c = L/r$), while next to the outer ring, it generally becomes 2D (it reaches the outer ring tangentially). In polar coordinates the angle of propagation can be expressed as $\psi(r) = \tan^{-1}(k_\theta/rk_r)$. Therefore, ψ shows a dependence on the local curvature.

Simulations for a cylindrical cell experiment [148, 149] and experimental results [149] show that HW1 become first unstable for high curvatures, so they appear first near the cooler central wall and propagate towards the hotter outer wall invading the whole cell looking like Archimedean spirals ($r = a\theta$, for $a \in \mathcal{R}$). Spirals are very common in many reaction-diffusion processes in extended systems and natural processes, they appear from an oscillatory medium like the Belousov-Zhabotinsky reaction. HW1 according to theoretical work [149] are expected to appear with much higher thresholds for $\vec{\nabla}_r T < 0$ (heating the core). But the nature of spirals is different depending on whether hydrothermal waves emerge at the inner core propagating outwardly for $\Delta T_r > 0$, or emerge at the outer ring propagating inwardly for $\Delta T_r < 0$. This last kind of spiral waves are also called ‘‘antspirals’’ [100] and they will be shown in this chapter.

5.2. Experimental setup

The cylindrical cell is laterally bounded between two copper walls: an inner cylinder with radius 4 mm, and an outer ring with radius 67.5 mm (see sketch in Fig. 5.2). The distance between walls is $L = 63.5$ mm. The bottom plate is a flat mirror that can be considered as thermally conductive. The fluid surface is free although the cell is hermetically closed from above with a lens (L_1). Then, the temperature in the air layer is supposed to follow a convective profile of temperatures [150] and the Biot number will be finite¹. The temperature at the inner core and at the outer ring is controlled by two closed water circuits. The temperature inside the cell is controlled by a third bath at room temperature $T_a = 19.0 \pm 0.1$ °C. A translation stage (scroll mechanism) enables to move vertically the bottom plate with a precision of ± 0.1 mm in order to choose the depth d of the fluid layer.

To remove the meniscus effect which would interfere in the results obtained from the shadowgraphy image, the fluid level is kept approximately 0.05 mm above the surface of the inner cylinder. Because of the great volatility of the fluid, the depth of the fluid layer is controlled using a four-quadrant laser diode, the reflected laser beam is centered on the diode. The voltage differences trigger a motor device that controls the injection and suction of fluid. This device

¹The Biot number: $Bi = \frac{hd}{\kappa}$, where h is the unit thermal interfacial conductance, d is the fluid depth and κ is the thermal diffusivity, provides information of the heat flux at the interface.

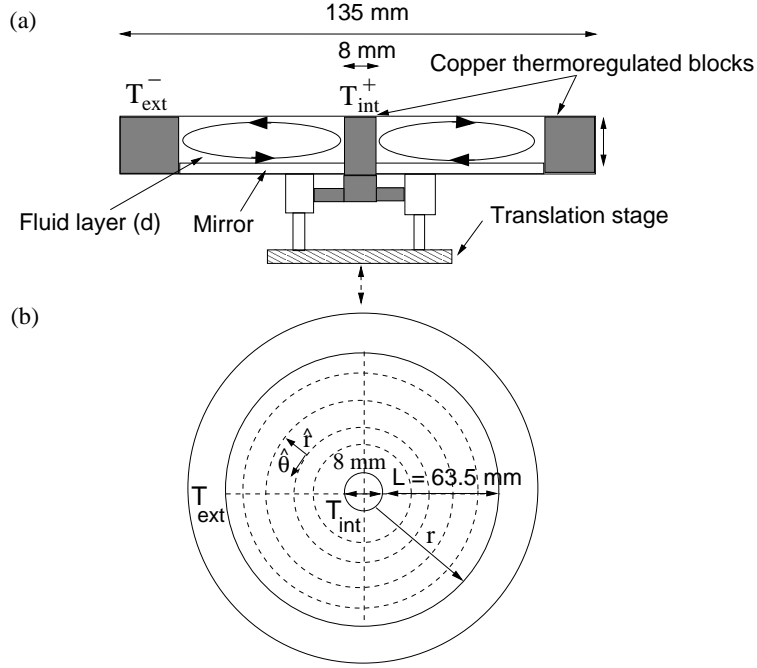


Figure 5.2: Experimental setup of the cylindrical cell: (a) cross-section; (b) top view with local unitary vectors $(\hat{r}, \hat{\theta})$. Dashed lines mark the position of the acquisition lines to record spatiotemporal diagrams along four perimeters. Also spatiotemporal diagrams along two diameter directions are recorded.

is connected to an outer fluid reserve and is very sensitive to fluid motions. This procedure is recorded along the measurements.

The equation of heat conduction in a fluid layer which is not in thermal equilibrium is given by the Fourier's law which states that the heat flux density \vec{q} is proportional to the temperature gradient: $\vec{q} = -\lambda \vec{\nabla} T$, where λ is the thermal conductivity of the fluid. The particular solution of thermal conduction in a finite fluid layer, with $T_{int} = 0$ K and $T_{ext} > 0$, is an analytical function of the radius [38] similar to a hyperbolic profile without taking into account the boundary conditions at the interface. This is similar to choosing zero vertical flux or $Bi = 0$. From numerical results it is found that the approximation $Bi \ll 1$ in the Newton's cooling law at the interface $\nabla_z T = -Bi(T - T_{air})$ is a good approximation for shallow layers [148]. In consequence, in the conductive regime a hyperbolic temperature profile is expected from theory, however experimental results on the radial temperature difference $(T(r) - T_{ext})$ (for the same cell [63] at $d = 1.2$ mm and $\Delta T_r = T_{ext} - T_{int} = 5, 10$ and 15 K measuring along the radius at different depths beneath the interface) are approximately constant along the radius with a small and sharp slope next to the central core. This is the convective temperature profile which fits better a logarithmic profile. This is mean to say that very close to the inner core there is the higher radial temperature difference, and that for small radii the temperature on the fluid bulk gets closer to the temperature of the outer ring T_{ext} .

5.2.1. The fluid

The fluid used is silicone oil 0.65 cSt, its physical properties are shown in Table 5.1. Because of its high volatility it is necessary to keep the cell closed but the air-fluid interface is free. Inside the cell the condensation is produced over a helicoidal copper rod (kept at room temperature 19°C) which is situated outside the outer ring and recovers the evaporated fluid. The corresponding Prandtl number is $Pr = 10.3$, therefore the temperature field is supposed to enslave the dynamics instead of the velocity field. The time required to achieve asymptotic states depends not only on the leading diffusive thermal temperature ($\tau_\kappa \approx 76.8 \text{ s} > \tau_\nu \approx 7.4 \text{ s}$ for $d = 2.20 \text{ mm}$) but on the thermal inertia of the involved materials (cooper, mirror and air). Asymptotic regimes are reached waiting over 30-60 minutes with steps of $|\Delta T_r| = 0.5 \text{ K}$.

Physical properties of the 0.65 cSt silicone oil	
Surface tension (25 °C)	$\sigma = 15.9 \text{ mNm}^{-1}$
Thermal conductivity	$\lambda = 0.10 \text{ Wm}^{-1}\text{K}^{-1}$
Thermal diffusivity ($\frac{\lambda}{\rho c_p}$)	$\kappa = 6.3 \cdot 10^{-8} \text{ m}^2 \text{ s}^{-1}$
Kinematic viscosity (25 °C)	$\nu = 0.65 \cdot 10^{-6} \text{ m}^2 \text{ s}^{-1}$
Density (25 °C)	$\rho = 760 \text{ kgm}^{-3}$
Refractive index (25 °C)	$n = 1.35$
Linear expansion coefficient	$\alpha = 0.00134 \text{ K}^{-1}$

Table 5.1: Physical properties of the 0.65 cSt silicone oil

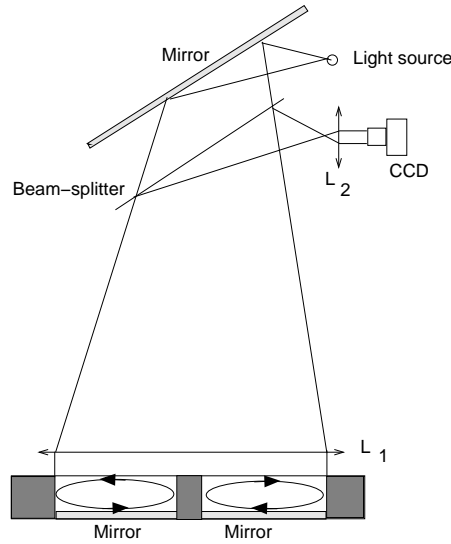


Figure 5.3: Sketch of the optical system to implement the shadowgraphy technique. $L_{1,2}$ are convergent lenses. The streamlines have been drawn for a negative temperature gradient ($T_{int}^+ > T_{ext}^-$).

This transparent silicone oil is chosen in order to visualize the convective patterns using the shadowgraphy technique. This technique allows us to observe the fluid bulk using a bottom mirrored surface in the cell and two convergent lenses L_1 and L_2 (see the sketch in Fig. 5.3). The

lens L_1 is also used as the upper plate to close the cell. Images are captured with a CCD camera (256 gray scale resolution) which was adjusted for each depth of the fluid layer.

5.3. Experimental techniques and data analysis

The control parameters are the depth of the fluid layer d and the radial temperature difference $\Delta T_r = T_{ext} - T_{int}$. Two cases are studied for each depth: $\Delta T_r > 0$ and $\Delta T_r < 0$.

If the geometric aspect ratio is simply defined as $\Gamma_g = 2\pi r/d$, it attributes an extended character preferably to the dynamics that generates waves propagating along the azimuthal direction with the highest values of the radius.

From the shadowgraphy images captured by the CCD camera we identify each pattern. For example, the aforementioned hydrothermal waves HW1 are shown in Fig. 5.4(a) and Fig. 5.5(a). Each shadowgraphy image can be unrolled transforming the polar system into a Cartesian one [see the corresponding unrolled images in Fig. 5.4(b) and Fig. 5.5(b)]. From the Cartesian system, the value of the angle $\psi = (\vec{k}, \vec{\nabla}_r T) = k_y/k_x$ can be expressed locally at $r = r_o$ as $\psi(r_o) = \tan^{-1}(k_\theta/r_o k_r)$ (in polar coordinates), ψ gives the direction of propagation of HW for a given radius r_o (see Fig. 5.1).

The meniscus effect round the inner cylinder is mainly a function of the temperature (T_{int}), in consequence the spatial calibration for a sequence of measurements must be tested each time (1 pixel ≈ 0.20 mm) from the shadowgraphy images.

Two kinds of shadowgraphy images are recorded: (1) by averaging images over more than 40 seconds (images are recorded at a minimum frequency of 5 Hz); (2) by subtracting two subsequent images differing in 1 second. The first kind of images provides information about stationary patterns [see Fig. 5.4(d)], meanwhile the second kind shows which patterns are oscillatory. Subtracted images allow us to identify hydrothermal waves traveling from the inner cold side to the outer ring [see Fig. 5.4(c)].

In the sketch of Fig. 5.2(b) spatiotemporal diagrams at 5 Hz are recorded over four selected perimeters [Fig. 5.6(a)] providing information of radial and spiral waves. In this way, by demodulation techniques from the 2D-Fourier spectra, we obtain their amplitudes, wave numbers and frequencies (k_θ, ω) [i.e. see the 2D-Fourier spectrum in Fig. 5.6(b) corresponding to the HW1 pattern of Fig. 5.6(a) with the presence of a source and a sink]. Spatiotemporal diagrams from the radii [Fig. 5.6(c)] provide information of corrotative rolls (concentric with the central core) or other waves like spirals involving components (k_r, ω) and their amplitudes [amplitude profile along a radii is shown in Fig. 5.6(d)]. Wave numbers obtained from spatiotemporal diagrams can always be checked out with the unrolled shadowgraphy images. From the information provided by the analysis we can characterize 2D-waves which are described by both components (k_r, k_θ) and 1D-waves which are described by one component for a given radius.

5.4. The stability diagram

The diversity of patterns which have been identified in this system allows to build a rich phase space. On the phase diagram in Fig. 5.7 we show previous results (dashed lines) for thin layers $d \leq 1.9$ mm [28], and new results (solid lines) for deep layers $d = [2.20, 5.55]$ mm. Each regime has

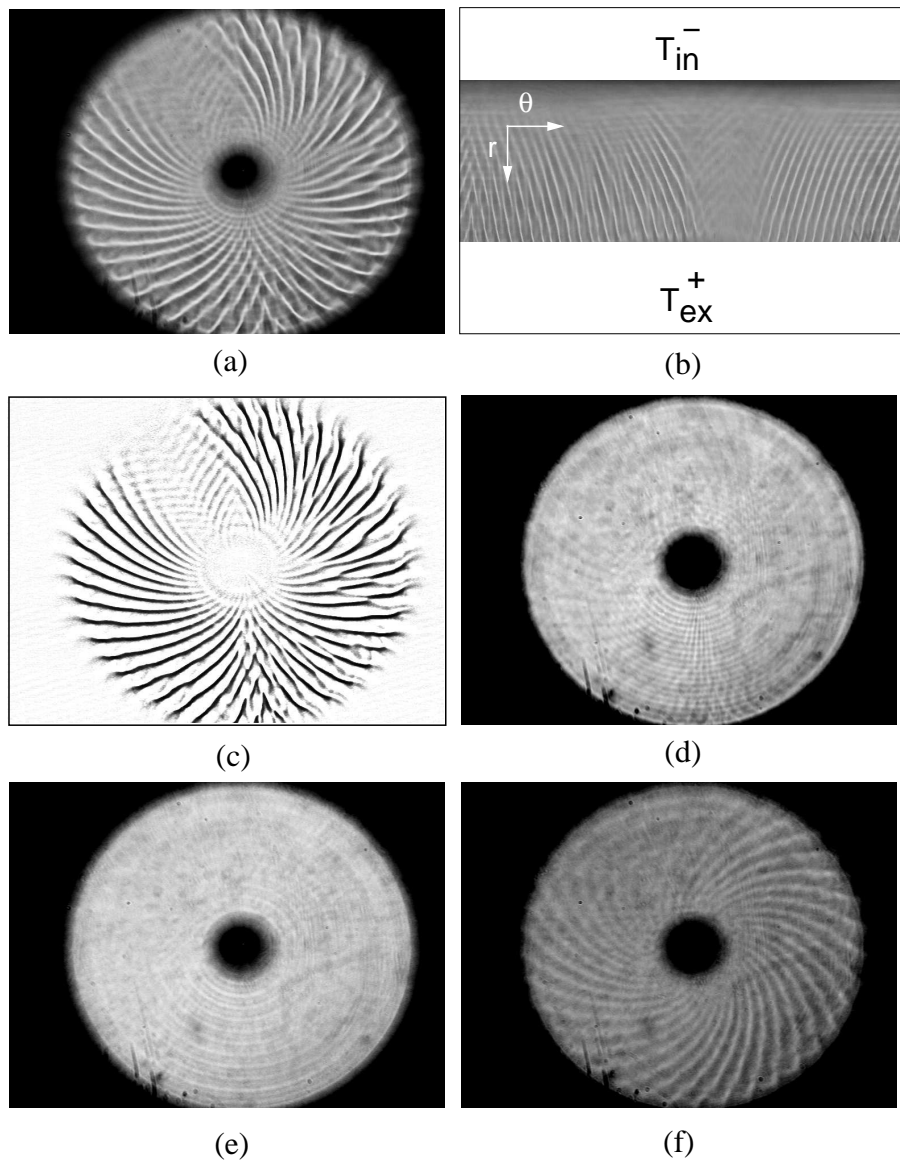


Figure 5.4: (a) Shadowgraphy image of the HW1 pattern at $d = 2.55$ mm and $\Delta T_r = 10$ K; (b) same unrolled image in Cartesian coordinates; (c) subtracted image; (d) average image. (e) Shadowgraphy image of the CR pattern at $d = 2.55$ mm, $\Delta T_r = 7.8$ K. (f) Close and above the threshold of the HW1 pattern at $d = 2.20$ mm, $\Delta T_r = 7.8$ K.

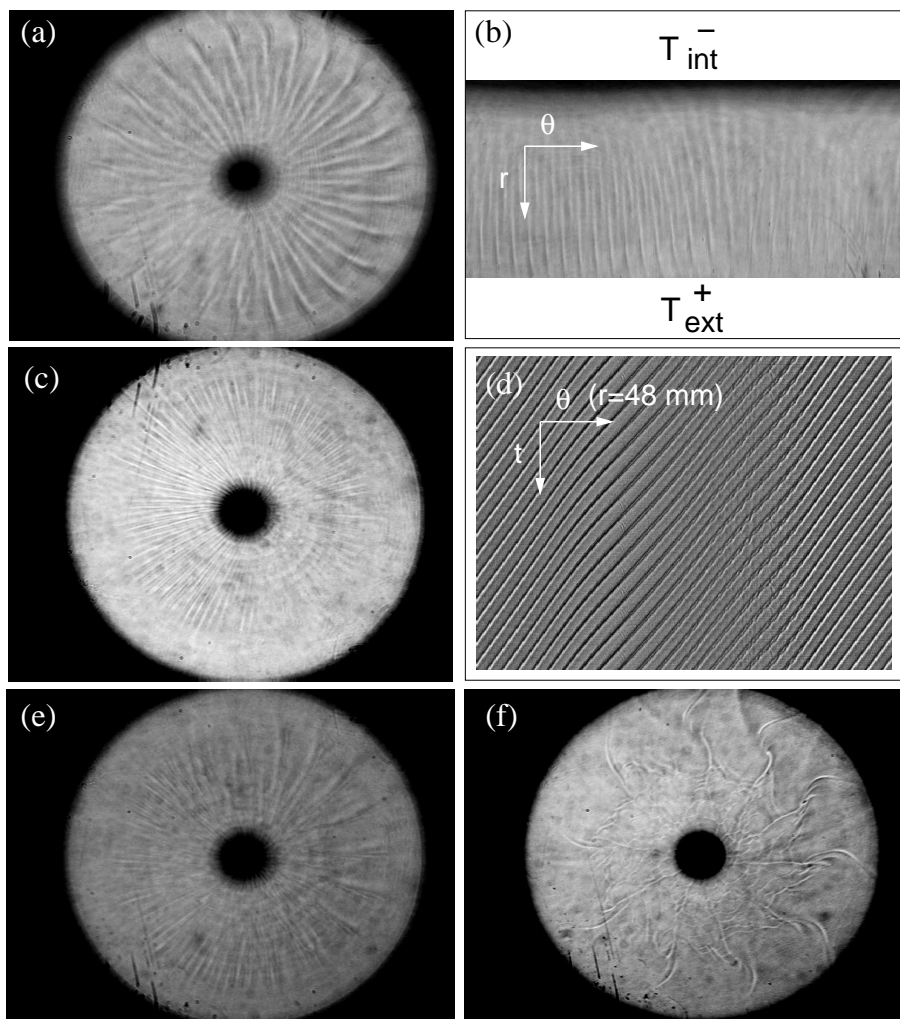


Figure 5.5: (a) Shadowgraphy image of the HW1 pattern at $d = 3.35$ mm, $\Delta T_r = 7$ K ; (b) same unrolled image in Cartesian coordinates; (c) multiradial pattern below the threshold of the HW1 waves at $d = 4.35$ mm, $\Delta T_r = 5.1$ K ; (d) perimeter spatio-temporal diagram at radius $r = 48$ mm from (a); (e) shadowgraphy image of the HW1 pattern at $d = 4.35$ mm, $\Delta T_r = 5.6$ K; (f) shadowgraphy image of the HW1 pattern at $d = 5.35$ mm, $\Delta T_r = 12.5$ K.

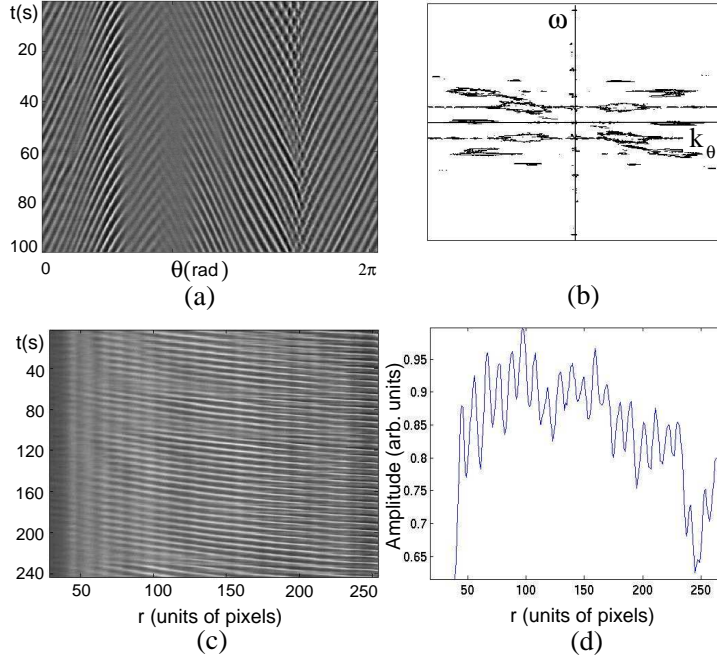


Figure 5.6: At $d = 2.55$ mm and $\Delta T_r = 10$ K: (a) spatiotemporal diagram along the perimeter for radius $r = 24$ mm; (b) Fourier spectrum of (a); (c) spatiotemporal diagram along a column (radius); (d) amplitude profile of (c), the modulation corresponds to corrotative rolls.

been identified from the shadowgraphy images at the asymptotic regimes. Thresholds represented by solid symbols have been localized by modifying ΔT_r with small steps of $|\Delta T_r| = 0.1$ K.

For every $\Delta T_r \neq 0$ the basic flow (BF) settles down similar to a flattened torus where the direction of propagation of the surface flow $\vec{v}_\zeta = v_\zeta \hat{r}$ (in the streamwise direction) depends on the temperature gradient direction. For $\Delta T_r > 0$ downstream goes from T_{ext} towards T_{int} and for $\Delta T_r < 0$ in the inverted direction.

From the stability diagram in Fig. 5.7 and for $d = [2.20, 5.55]$ mm we distinguish the following instabilities:

- A *primary instability* towards **stationary corrotative rolls (CR)** observed for $\Delta T_r > 0$ and $\Delta T_r < 0$. This pattern overlaps the basic flow in the form of stationary concentric rolls [i.e. for $\Delta T_r < 0$ see Fig. 5.8(a)] and thus, it has a continuous rotational symmetry. For the explored depths CR correspond to stationary waves. At $d = 2.55$ mm and $\Delta T_r = 10$ K we obtain $k \approx 2 \text{ mm}^{-1}$ ($\lambda \approx 3$ mm) [see the shadowgraphy image Fig. 5.4(e) or from the amplitude profile in Fig. 5.6(d)]. The average shadowgraphy images of the HW1 pattern confirms the presence of the CR pattern [see Fig. 5.4(d)]. Under certain conditions the CR pattern have appeared like vacillating concentric rolls keeping their stationary positions [see Fig. 5.4(e)], this oscillatory behavior has not been found numerically but it was already observed experimentally in 1974 [151]. For $\Delta T_r < 0$ they are also present, for example in Fig. 5.8(a), with a doubled wave length. Numerical studies [148] at $\Delta T_r < 0$ verify the presence of the CR pattern for small depths from a primary instability developed from a linear flow profile, whereas for higher depths the basic flow pattern corresponds to that of a

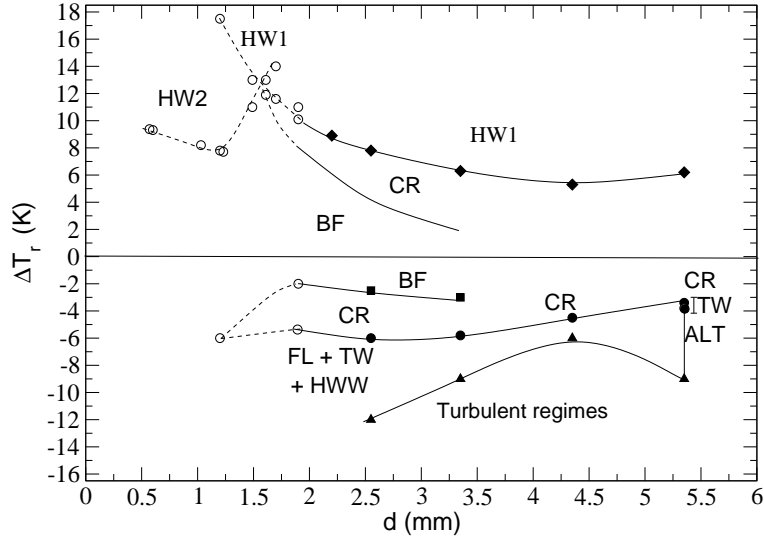


Figure 5.7: Stability diagram of the cylindrical cell. Dashed lines correspond to previous results studied by Garnier [28] for $d \leq 1.9$ mm. Solid lines and the concerned regimes correspond to the new reported results in this chapter for $d = [2.20, 5.55]$ mm. BF (basic flow), CR (corrotative rolls), HW1 (1D-hydrothermal waves), HW2 (2D-hydrothermal waves), FL (flower-like pattern), TW (1D-traveling waves or radial waves), ALT (1D-alternating waves), HWW (wake-waves).

return flow without the presence of CR.

- Propagative patterns appear from corrotative rolls (CR), these subsequent *secondary instabilities* are of the oscillatory type. We have distinguished the following:

- **1D-hydrothermal waves (HW1)** for $\Delta T_r > 0$. For the explored depths ($d \geq 2.20$ mm) the HW1 pattern becomes always unstable from CR. These wave-pattern (HW1) is similar to Archimedian spirals [i.e. see the shadowgraphy images in Fig. 5.4(a,f)]. We notice how the center behaves as a nucleus emitting spiral waves that end up at the outer ring, they travel from the cold inner core dying at the hot outer ring. The HW1 pattern, in the range $d = [2.20, 3.35]$ mm, belongs to the classical 1D-hydrothermal waves predicted by Smith and Davis [58, 66]. Regarding the angle of propagation, at $d = 2.20$ mm, we have measured from the perimeter diagrams (at $r = 24$ mm) $\psi \approx 57^\circ$. This value keeps constant along the radius until $r = 48$ mm. Also from the shadowgraphy image in Fig. 5.4(a) (at $r = 2.2$ mm) $\psi \approx 57^\circ$. Close to the outer ring ψ diminishes. From the ascending and descending sequences of measurements, this instability appears to be supercritical in all the explored range (quantitative results for small depths are found in Ref. [28]). From the shadowgraphy images at the threshold of HW1 the spiral waves appear preferably on one half of the cell, sources or sinks have been observed above the threshold [Fig. 5.4(a-c)]. From Fig. 5.6(a) at $r = 24$ mm, applying demodulation techniques, we obtain for the left-right ($v\pm$) traveling waves [see Fig. 5.6(b)] the following results: $k_\theta(v-) = 2.22 \pm 0.05 \text{ mm}^{-1}$, $\omega(v-) = 1.323 \pm 0.009 \text{ s}^{-1}$, $k_\theta(v+) = 2.07 \pm 0.02 \text{ mm}^{-1}$, $\omega(v+) = 1.143 \pm 0.004 \text{ s}^{-1}$.

At $d = 3.35$ mm, [Fig. 5.5(a)] alternated arms of the Archimedian spiral emerge closer

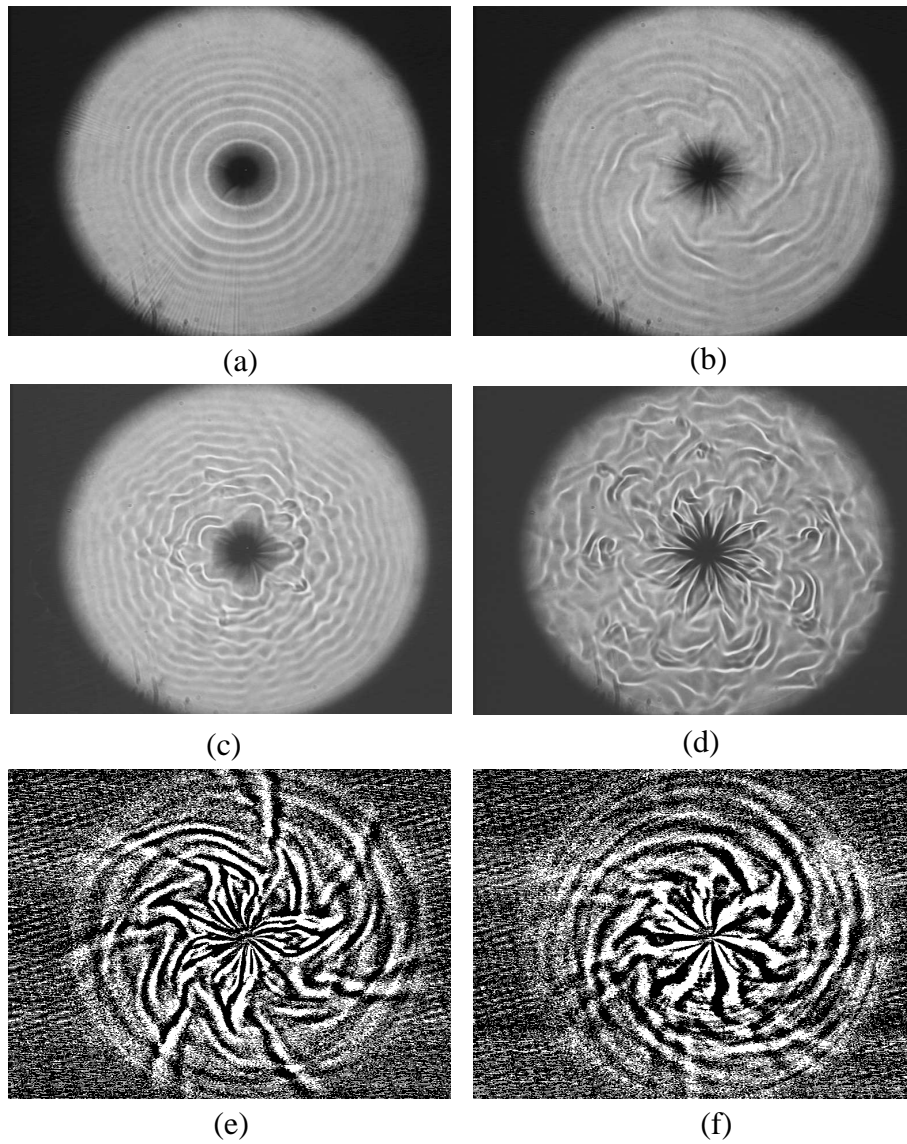


Figure 5.8: Shadowgraphy images for different patterns at: (a) $d = 2.20$ mm, $\Delta T_r = -6.4$ K ; (b) $d = 3.30$ mm, $\Delta T_r = -7$ K ; (c) $d = 2.56$ mm, $\Delta T_r = -8$ K ; (d) $d = 3.35$ mm, $\Delta T_r = -15$ K. Subtracted images: (e) $d = 4.35$ mm, $\Delta T_r = -5.5$ K ; (f) $d = 4.35$ mm, $\Delta T_r = -6.5$ K.

to the center with higher k_θ than the same HW1 pattern at smaller depths. From Fig. 5.5(b) the angle of propagation is $\psi \approx 90^\circ$. If we analyze the perimeter diagrams at radius $r = 48$ mm [Fig. 5.5(d)] we get a frequency for the longer arms of $\omega \approx 0.13$ s^{-1} . For deep layers ($d > 4.35$ mm), close and below the threshold of the HW1 pattern, a multiradial pattern appears with $\lambda \sim d$ [Fig. 5.5(c)]. Besides, for $d > 4.35$ mm hydrothermal waves show quite a different pattern as it is shown in Fig. 5.5(e), with a larger azimuthal modulation (smaller k_θ). As we increase the control parameter ΔT_r above the multiradial pattern a central pattern of hexagonal cells is observed (BM convection, because of the radius of the central heater beneath the mirror is wider than the inner cylinder), further on hydrothermal waves emerge with a more complex geometry [Fig. 5.5(e,f)].

For $\Delta T_r < 0$ hydrothermal waves (not one-dimensional) are observed under the form of wake-waves (HWW) in the flower-like regime which will be explained below.

- **Radial waves or traveling waves (TW)** for $\Delta T_r < 0$. Radial waves (along radii) have not been found to be stationary for neither of the studied regimes. In Fig. 5.9(a) (at $d = 5.35$ mm, for $\Delta T_r < 0$) we observe the presence of four radii, this pattern corresponds to a quasi 1D-dynamics. These radii appear because of the splitting of the concentric fluid flow (CR) into four counter-rotating rolls of wave length $\lambda \approx 8$ mm. These rolls begin to propagate as a TW pattern with frequency $\omega \approx 0.33$ s^{-1} ($T = 19$ s). For a higher control parameter ΔT_r they begin to alternate, this is defined as an alternating pattern, ALT, with a doubled wave length. The TW pattern becomes unstable through the presence of a source and a sink [Fig. 5.9(b)] towards the ALT pattern consisting of two counter-propagative waves [see Fig. 5.9(d)]. In the next section we show that this instability happens to be “weakly subcritical”.

In the shadowgraphy image of Fig. 5.9(a) we find out a thermal azimuthal wave that propagates outwardly and whose profile is similar to the stationary flower-like pattern which is explained in the next item.

- **Flower-like patterns (FL)** for $\Delta T_r < 0$ [Fig. 5.8(d-f)]. These patterns are characterized by the presence of waves with an azimuthal modulation around the inner core and become unstable always from the CR pattern (see the stability diagram in Fig. 5.7). The FL pattern coexist with radial waves (TW) and corrotative rolls (CR), we might consider that the FL pattern is similar to a kind of “thermal flowers”². At the threshold of this instability a doubling of the wave length of the basic pattern CR is produced, this doubling had not been observed for thinner layers ($d \leq 1.9$ mm) before. FL patterns coexist with TW except for the regime represented by the shadowgraphy image in Fig. 5.8(c) where there are two counter-propagative waves similar to a superimposed ALT pattern, this FL pattern bifurcates locally before spreading along the azimuthal direction. Far from the threshold, the complexity of the FL pattern is the result of strong nonlinear interactions between radial waves (TW) and corrotative rolls (CR), apart from the effect of small aspect ratios involved near the inner core. When we get far from the threshold (decreasing ΔT_r) the FL pattern rotates (clockwise or counter-

²In literature both definitions, flowers and petals, differ only from the fact that petals belonging to flower-like patterns are detached.

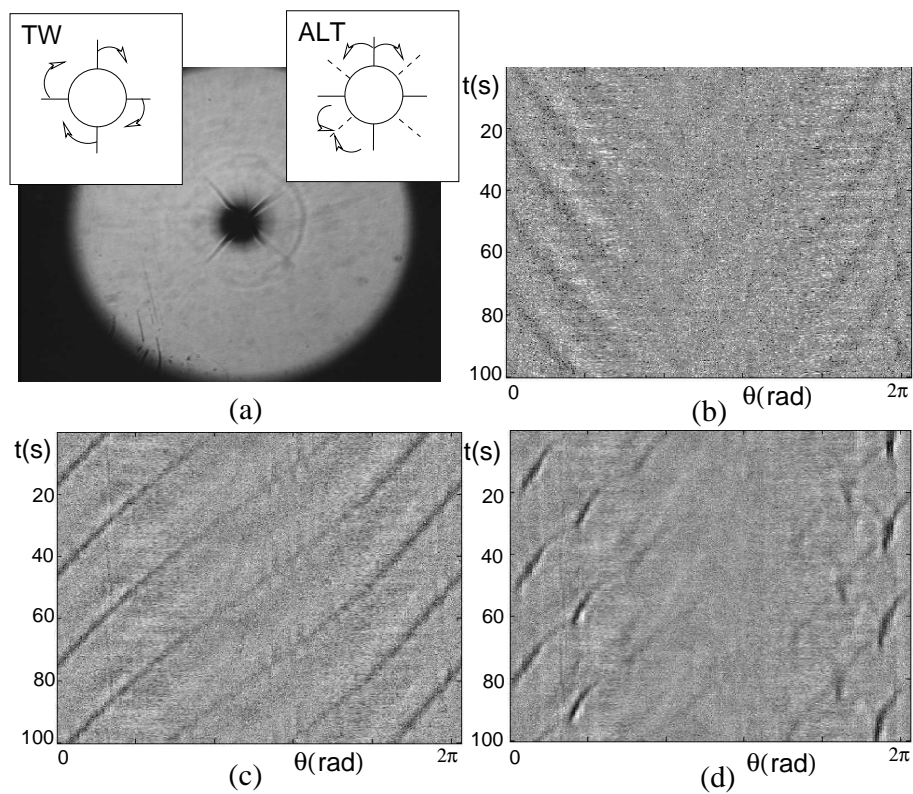


Figure 5.9: (a) Shadowgraphy image of the TW pattern at $d = 5.35$ mm. Corrotative rolls (CR) are also present but their intensity profile is smooth in this sequence. Inserted sketches represent the dynamics of the traveling and alternating waves. Perimeter spatiotemporal diagrams for radius $r = 5$ mm at: (b) $\Delta T_r = -3.3$ K, a TW pattern with 1D-defects close and above the threshold; (c) $\Delta T_r = -3.7$ K, a left-TW pattern; (d) $\Delta T_r = -4.0$ K, an ALT pattern.

clockwise) with a higher frequency than the TW pattern found for higher depths, like in Fig. 5.8(e) with $\omega \approx 0.52 \text{ s}^{-1}$ ($T = 12 \text{ s}$). The further the system is from the threshold petals turn with a higher frequency. Under these conditions, radial waves convert into wake-waves HWW far from the center [see images in Fig. 5.8(b,e,f)]. Because wake-waves happen to move towards the heating source (the inner core), they might be considered to be hydrothermal waves, not of the type HW1 because of the presence of the FL pattern.

A supercritical bifurcation towards the FL pattern has been quantified for small depths with constant frequency [28]. Experimental work on flower-like patterns is found in other systems [57, 147, 152, 153]. Specifically, Ref. [153] studies the commensurate and incommensurate rotational angles. In our experiment, the number of petals increases from five to eight [see Fig. 5.8(b),(c)] as we decrease depth (from $d = 4.35$ to 2.20 mm). The qualitative characterization of the bifurcation towards the FL pattern for the explored depths $d = [2.20, 4.35] \text{ mm}$ shows at threshold a central circular front which becomes irregular in a small region as we increase smoothly $|\Delta T_r|$. The sequences of shadowgraphy images reveal that the inner corrotative roll bifurcates supercritically towards the FL pattern. Radial waves provide an earlier stage of spatial differentiation of each petal before spinning, in the sense that the emergent mechanisms of convection for radial waves generate spatial inhomogeneities which act as the starting “seed” of a petal growth process.

- *Turbulent patterns* for $\Delta T_r < 0$ [Fig. 5.8(d)] and $\Delta T_r > 0$. This is the ubiquitous turbulent regime present in many open flow experiments as well as in nature, where spatiotemporal correlation lengths decay. Turbulence for $\Delta T_r < 0$ is achieved more quickly than for $\Delta T_r > 0$, this is probably due to the role of the HWW generated at the outer ring and traveling inward. Also for $\Delta T_r < 0$ the FL pattern becomes turbulent easily as the depth is increased until $d \approx 4.50 \text{ mm}$ (see the stability diagram Fig. 5.7). We have not observed any coherent pattern in this turbulent regime except for small vortices in previous stages [see Fig. 5.8(d)].

It is worthwhile to mention that 2D-hydrothermal waves (HW2) have only been observed for small depths and for $\Delta T_r > 0$ [28] (see Fig. 5.7). In this pattern ψ goes from 0° close to the threshold to 45° further on. These waves become unstable first near the central core and as ΔT_r increases they invade the whole cell. Close and above the threshold they propagate like concentric waves, and as they invade the whole system their wave-front becomes irregular.

5.4.1. Secondary instability to the ALT pattern

For $\Delta T_r < 0$, when the inner core is heated, the basic flow corresponds to that of a flattened torus which ascends at the center with an outward movement along the free surface in the stream-wise direction (\hat{r}) descending at the outer ring. According to the dynamics at high depths ($d \geq 4 \text{ mm}$) in the 1D-cell ($Pr = 75$) we look for similar patterns in the 2D-cell ($Pr = 10$), although in this case: (i) this dynamics is restricted to a narrower range $|\Delta T_r| = [3.0, 4.0] \text{ K}$ at $d = 5.35 \text{ mm}$; (ii) the TW pattern emerges from a CR pattern of the kind observed for $\Delta T_r > 0$ (without doubling of the wave length); (iii) the ALT pattern triggers the strong resonant stationary mode

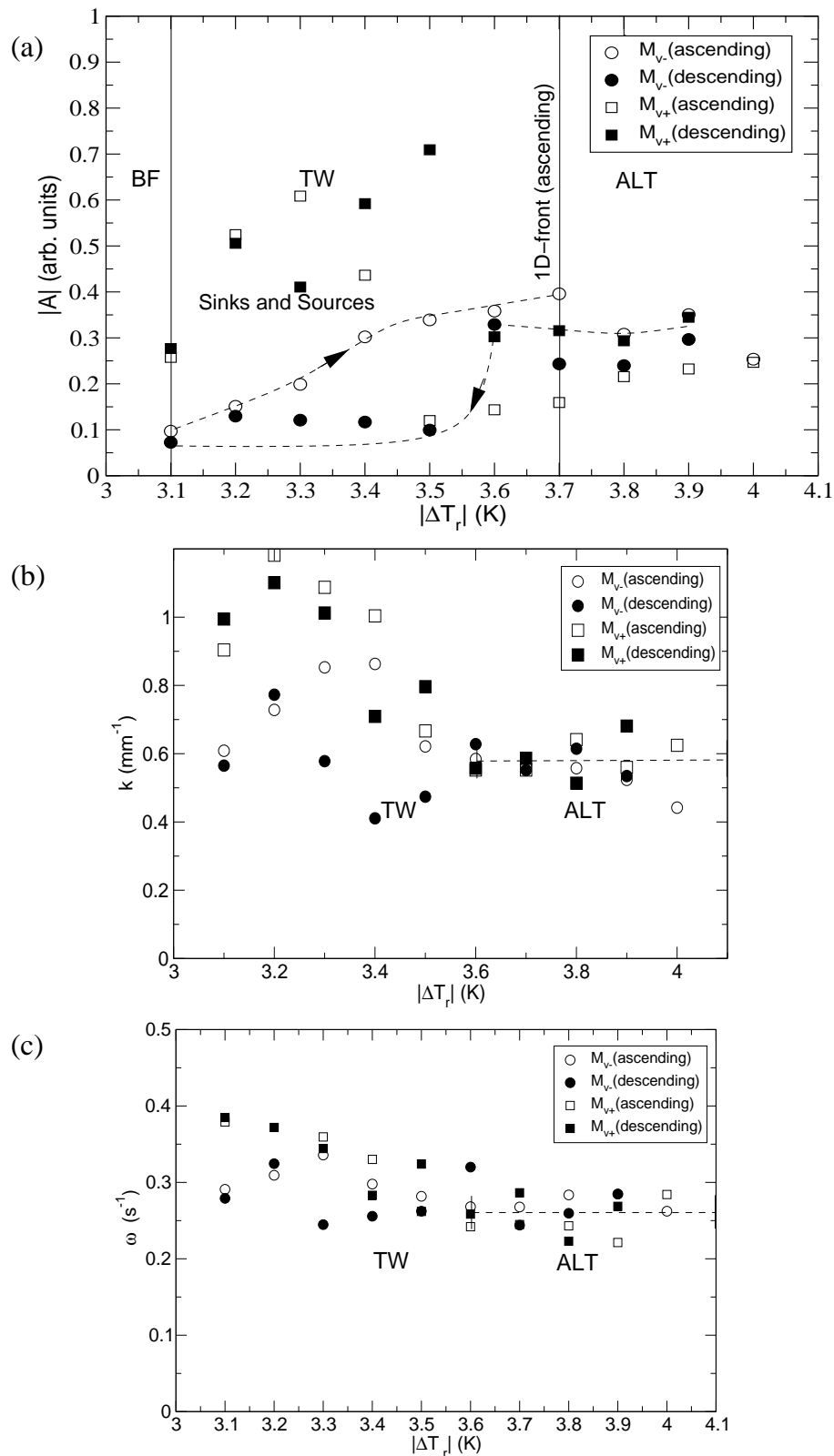


Figure 5.10: For an ascending and a descending sequences of measurements: (a) evolution of the modulus of the amplitude of the critical modes (dashed lines are a guide to the eye); (b) evolution of the wave numbers; (c) evolution of the frequencies. Dashed segments indicate the selected range in the ALT pattern to obtain average values of the propagative modes $M_{v\pm}$. Vertical lines split different regimes. Sinks and sources are present in the TW regime. A 1D-front connects the TW and the ALT patterns in the ascending sequence close to the threshold.

characteristic of the 1D-cell far from the threshold. There is a previous work [147], with a different cylindrical cell but with the same fluid, where similar patterns were described although the critical behavior had not been characterized then.

In the present work we study quantitatively the instability towards the ALT pattern from the previous TW pattern. Firstly, the bifurcation from the CR pattern (with continuous rotational symmetry) towards traveling waves TW is represented in the Fourier spectra by one fundamental mode M_{v+} or M_{v-} . Secondly, the subsequent bifurcation towards alternating waves ALT with two counter-propagative waves is represented by the fundamental modes $M_{v\pm}$. One of the main differences in comparison with the experimental results observed in the 1D-cell is the presence of sources and sinks (1D-defects) in the asymptotic regimes. In order to check hysteresis we have chosen, in the ascending and descending sequences, the modulus of the amplitude of the critical modes as a suitable control parameter [Fig. 5.10(a)].

The following results have been quantified for a radius $r = 5$ mm and with step of $|\Delta T_r| = 0.1$ K waiting for the asymptotic regime to be reached. The presence of sources and sinks is the cause for enlargement of the peaks in the Fourier spectra along the sequence of measurements. That is why there is a dispersion of data ($|A|$, k and ω) for this kind of patterns [see data in Fig. 5.10(a,b,c) outside the dashed segment representing the ALT pattern]. From these results, we get the average values over the range $|\Delta T_r| = [3.6, 4.0]$ K which correspond to the ALT pattern: $\langle k_{\pm v} \rangle \approx 0.56 \text{ mm}^{-1}$ ($\langle \lambda_{\pm v} \rangle \approx 11.22 \text{ mm}$) and $\langle \omega_{\pm v} \rangle \approx 0.27 \text{ s}^{-1}$ ($\langle T_{\pm v} \rangle \approx 23 \text{ s}$).

From Fig. 5.10(a) in the ascending sequence we obtain the threshold to the left-TW pattern at $\Delta T_r = -3.1$ K, and to the ALT pattern at $\Delta T_r = -3.7$ K, with the presence of a 1D-front between the TW domain and the ALT domain. At the threshold of the TW pattern the amplitudes of the critical modes in the ascending and descending sequences differ in $A_{v+} = 4A_{v-}$, this bifurcation to the TW pattern is expected to be supercritical from the CR pattern. As we increase $|\Delta T_r|$ finally a homogeneous left-TW pattern is achieved throughout the presence of a source and a sink along an interval of 0.4 K. The descending results in Fig. 5.10(a) show a transition from the ALT pattern to the right-TW pattern with threshold at $\Delta T_r = -3.5$ K. The stronger nonlinear ALT regime keeps approximately constant amplitudes, wave numbers and frequencies. From the coexistence of patterns (TW and ALT) and a weak hysteresis behavior we could end up, at first sight with a “weak subcritical” dynamics, this topic will be discussed in the following section.

A nonzero group velocity means that the convective threshold follows $\varepsilon_{conv} = \varepsilon_{abs} - \mathcal{O}(L^{-2})$ although this expression comes from a the linear theory with zero curvature systems [127]. The effect of periodic boundary condition at $r = 0$ (with a maximum curvature $\Gamma_c = L/r$) should play an important role in determining effective threshold positions. This fact could probably be the reason why, in the instability towards the ALT pattern, thresholds of the ascending and descending sequences differ in 0.2 K [3.7 K-3.5 K from Fig. 5.10(a)] for both modes $M_{v\pm}$. A hysteresis cycle in the bifurcation to ALT is expected from the observed jump of the ascending amplitude M_{v+} and descending amplitudes of $M_{v\pm}$ in Fig. 5.10(a). Furthermore, $v_g \neq 0$ is the most probable cause for a nonzero front velocity according to the small slope of 1D-fronts observed in the spatiotemporal diagrams. Unfortunately, because we have not recorded any transient regime, we are not able to determine the group velocity.

5.5. Discussion and conclusions

Looking upon the stability diagram in Fig. 5.7 a comparison between themocapillary effects for thin layers and thermogravitatory effects for deep layers is unavoidable. Both effects are equally important when the dynamic Bond number ($Bo_D \propto d^2$) is $Bo_D = 1$ at $d = 2.83$ mm. For the explored depths the corresponding Bond numbers go from $Bo_D = 3.56$ ($d=5.34$ mm) to $Bo_D = 0.60$ ($d=2.20$ mm). For the primary instability and according to numerical results [148] when $Bo_D < 1$ the radial thermal gradient is supposed to drive the dynamics of corrotative rolls, meanwhile when $Bo_D > 1$ the vertical gradients are responsible for the homogeneous basic flow. In this study, corrotative rolls (CR) fit a linear flow meanwhile the homogeneous pattern or basic flow (BF) fits a return flow.

Concerning the dynamics for $\Delta T_r < 0$, as we “move” in the stability diagram for $Bo_D < 1$, decreasing d until $d = 1.9$ mm, the bounded region of the FL pattern becomes wider, always from the doubled wave length CR pattern, as well as turbulence is achieved further away as we increase $|\Delta T_r|$. On the opposite side, for $Bo_D \approx 4$, the strong thermogravitatory effects allow the TW pattern to bifurcate supercritically from the CR pattern (without wave length doubling) which has a continuous rotational symmetry. In the 1D-cell supercriticality of the TW pattern from a basic homogeneous flow is produced at $Bo_D = 2.4$. The threshold shift in the transition from TW to ALT (direct and reverse bifurcations) probably comes from the advective nature of the critical modes $M_{v\pm}$, this transition and the previous one are convective and global because the critical modes grow over the whole system. Owing to this fact, only the jump of the modulus of amplitudes rests as a valid condition for defining a weak subcritical transition from TW to ALT apart from the existence of 1D-fronts.

Still for $\Delta T_r < 0$ and depth in between $1.9 \text{ mm} < d < 4.35$ mm, the instability towards thermal azimuthal waves, or the FL pattern, is probably generated by the high radial temperature gradient next to the inner core. For higher depths ($d = 5.35$ mm) the convective uprising flow at $r = 0$ descends at approximately $r = 1/4L$ with an almost circular front. This pattern will become turbulent as $|\Delta T_r|$ is increased without any flower-like pattern instability. For smaller depths, as ΔT_r is increased the circular front bifurcates through a modulated pattern of petals with an azimuthal wave number component k_θ which goes from 1.3 to 2 mm^{-1} as depth is increased. Beyond the threshold of the FL pattern, when radial waves turn into wake-waves, the wave vector \vec{k} of wake-waves aims towards the center (from T_{ext}^- to T_{int}^+), this is why wake-waves (HWW) are considered as hydrothermal waves [Fig. 5.5(f)]. However, in contrast to HW1, HWW are generated at the outer region and propagate inwardly [see Fig. 5.8(b)], hence they are antispirals like water funnels act as sinks, whereas HW1 act as sources. Upon the stability diagram we have shown that hydrothermal waves are sources for $\Delta T_r > 0$ and sinks for $\Delta T_r < 0$. Further beyond the HWW regime, a turbulent pattern invades the whole cell. In this 2D-turbulent regime, we have not found any proper order parameter.

In the case of $\Delta T_r > 0$, HW1 extends over a great region on the stability diagram before the system achieves turbulent regimes for high $|\Delta T_r|$. When $Bo_D > 1$ two different convection mechanisms modify the dynamics of hydrothermal waves: (i) Near the central core a quasi-hexagonal pattern appears, similar to BM hexagonal cells because the critical vertical temperature gradients is homogeneously spread near the center and it is still more important than the radial temperature gradient. In permanent regimes, this “hexagonal pattern” is confined close to the

center, then the remaining radial thermal gradient enables propagative waves only in the outer region. In this situation the cylindrical dynamics in the outer region fits the conditions of an annular system (with large inner radius), traveling waves in this outer region with larger wave length are supposed to follow convective mechanisms similar to HW1. (ii) A multiradial pattern extends over the whole cylinder similar to a multicellular pattern of counter-rotating rolls like the primary instability in the 1D-cell. We show another interesting fact, hydrothermal waves emerge for both positive and negative values of $|\Delta T_r|$. For $\Delta T_r > 0$ and for deep layers, because of the increasing effect of vertical temperature gradients, the threshold of the HW1 pattern is lower and the angle of propagation ψ tends to 90° (for $Bo_D < 1$, $\psi \approx 60^\circ$). For $\Delta T_r < 0$, hydrothermal waves appear as wake-waves, the HWW pattern, further away from the FL threshold and for $d \leq 4.35$ mm. These results, regarding the HW1 instability, agree with the stability analysis by Garnier and Normand [149] that shows the effect of curvature in the dynamics using a local Grashof number $Gr = \alpha g(T_{ext} - T_{int})d^3\Gamma_c^{-1}/\nu^2$. For $\Delta T_r > 0$ hydrothermal waves appear in the region with the largest curvature (Γ_c) and its threshold is higher for $\Delta T_r < 0$.

It should be stressed that for deep layers, the complexity of patterns for $\Delta T_r < 0$, either emerging close to the inner core (i.e. FL patterns for $\Delta T_r < 0$) or in the outer region (i.e. the HWW pattern $\Delta T_r > 0$), are specially developed from the characteristic temperature profile in the bulk (the sharpest lateral temperature gradient is bounded in a central region very close to the inner plot fitting a logarithmic profile) and the vertical heat flux across the air-fluid. A strong heat flux at the interface coming from the bottom towards the air is expected. Owing to this fact, theoretically it might be considered to take $Bi \neq 0$ concerning the logarithmic thermal profile, and the conductive bottom of the cell (according to the reported BM hexagonal cells). For deep layers, the vertical temperature gradient is supposed to play an important role (high Biot numbers might be considered in models). Besides, this vertical temperature gradient might convert the linear flow, which is characteristic of shallow layers, into a return flow according to numerical results [148]. Another convincing fact that supports the importance of the vertical temperature gradient are patterns appearing in the “extended system” (along the perimeter): (i) the multiradial pattern [see Fig. 5.5(c)], and (ii) the instabilities towards the TW and the ALT pattern. All of them also appear in the 1D-cell by varying the vertical temperature difference.

2D-defects like sources or sinks break the azimuthal invariance of the system. They have been observed in HW1 for ($\Delta T_r > 0$). 1D-defects (a source and a sink) in the TW patterns and 1D-fronts are observed between the TW and ALT patterns. In the 1D-cell sources and sinks appeared only in transient regimes, in the asymptotic regimes only 1D-fronts were observed for a similar transition.

Conclusions and Outlook

Conclusions

From the experimental results shown in this work about a **1D** (the rectangular cell with localized heating) and a **2D** (the cylindrical cell with lateral heating) **thermoconvective experiments**, we may highlight that there is an outstanding *universality* in patterns which arise from **secondary instabilities** independently of the responsible physical mechanisms at the onset of these instabilities and independently of the geometry. Patterns in both convective experiments, the 1D-cell and 2D-cell, are generated from localized heating sources (along a central line in 1D-cell and along a wall in 2D-cell), and this particularity brings us the opportunity to understand *growth processes* in nature (real 3D systems) as instabilities, where the source of energy is also localized generating synchronized oscillatory phenomena.

Patterns, in both experiments, are the result of nonlinear couplings between the amplitudes and the phases of the critical modes. This information is obtained from the **global analysis** which is applied to the entire information given by the spatiotemporal diagrams. We have shown that, in general, the modulus of the critical amplitudes is a suitable order parameter when we try to determine the nature of an instability quantitatively close to the threshold.

If we compare results between the 1D-experiment and the 2D-experiment we find that depending on the depth of the fluid layer the **basic patterns** can be: (i) a *homogeneous pattern* for deep layers: two counterrotative rolls ascending at the heating line in the 1D-cell (primary convection PC), and a flattened torus in the 2D-cell (basic flow BF); (ii) a *stationary cellular pattern* for shallow and intermediate layers: the array of hotspots (ST) in the 1D-cell and the corrotative or concentric rolls (CR) in the 2D-cell. From theoretical predictions [60] and numerical simulations [148], homogeneous basic patterns correspond to a return flow (where buoyancy effects are important) while stationary cellular patterns correspond to a linear flow (where the traction due to surface tension gradients is important).

From these basic patterns both systems reach the subsequent instabilities by increasing the control parameter until **turbulence**, or disorder, is developed. Turbulence is achieved before in the 2D-cell ($Pr \approx 10$) because of (i) the smaller Prandtl number (instabilities are much more closer or may overlap according to Krishnamurti [142]), and (ii) the local curvature effects ($\Gamma_c = L/r$) which impose different phase velocities ($v_\phi = \omega/k$) depending on the radius. We have observed in the 2D-cell that turbulence is *well-developed* (there is no characteristic spatial scale) while in the 1D-cell ($Pr \approx 75$) turbulence belongs to the kind of *weak-turbulence* where certain symmetries are still conserved. It is characterized by drifting lattice-patterns where defects (phase singularities or dislocations) appear stochastically.

Except for the instability mechanisms of hydrothermal waves which appear in the 2D-cell for small and intermediate layers, we consider that for deep layers the **vertical temperature difference** yields similar patterns in both cells. This is the case of the traveling wave (TW), the alternating (ALT) and the cellular patterns (ST in the 1D-cell and multiradial in the 2D-cell) observed in both experiments.

For **deep layers**, both fluid layers, the cylindrical and the rectangular one, bifurcate *supercritically* towards the TW pattern from a homogeneous pattern with continuous translation symmetry in the direction parallel to the heating line. And beyond bifurcate *subcritically* towards the ALT pattern because of (i) the discontinuous jump of the amplitude of the traveling modes; and (ii) the presence of 1D-fronts. However, in the 2D-cell, the ALT pattern is the result of two counterpropagative modes whose nonlinear coupling does not cause the strong presence of the stationary mode at the threshold like in the resonant triad of the same pattern in the 1D-cell.

Hydrothermal waves have only been observed in the 2D-cell for intermediate and shallow layers where the convection mechanisms due to surface tensions are stronger, for both $\Delta T_r > 0$ and $\Delta T_r < 0$. For $\Delta T_r > 0$, hydrothermal waves are *outward spirals* (one-dimensional, HW1) acting as sources, whereas for $\Delta T_r < 0$ they are *inward spirals* (wake-waves, HWW) acting as sinks.

It is very compelling to contrast the different **physical aspect ratios** in the 2D-cell depending on whether patterns emerge at the inner (flower-like (FL), HW1, TW and ALT patterns with $\Gamma = 2\pi r_{int}/\lambda$), or at the outer boundary wall (hydrothermal wake-waves (HWW) with $\Gamma = 2\pi r_{ext}/\lambda$), or along the streamwise direction with $\vec{k} \parallel \hat{r}$ (corrotational rolls with $\Gamma = (r_{ext} - r_{int})/\lambda$). The pattern exhibiting the higher complexity, because different physical aspect ratios are involved, has been observed for $\Delta T_r < 0$ and it is the FL pattern which appears from a wave length doubling of the corrotational rolls and at the same time coexists with radial waves (TW) and for higher temperatures with wake-waves (HWW).

From now onward, we restrict the conclusions to the **1D-experimental results**. As we move along the stability diagram (ΔT_v vs d) decreasing depth we are able to cross a codimension-2 point from the supercritical instability towards TW (deep layers) towards the subcritical instabilities for intermediate and shallow layers. **Subcriticality** is present in oscillatory instabilities which arise from a basic stationary cellular pattern (ST) for intermediate and shallow layers. This ST pattern might become unstable because of a critical traveling mode (the TW pattern) or because of two critical counter-oscillatory waves which trigger the resonant triad (the ALT pattern). According to the theoretical predictions by Coulet and Ioss [16] (developed from symmetry arguments at the threshold of secondary instabilities from stationary cellular patterns) a doubling of the wave length ($q = 1/2$) is expected like in the ALT pattern, but for the TW pattern it is found that $q = 2/3$. This difference could be the result of other 2D or even 3D instability mechanisms which might have an important role in the experiment, or because subcritical arguments should be included in a new theory.

Stationary or fluctuating 1D-fronts in bistable regimes arise at subcritical instabilities from the basic ST pattern. Stationary 1D-fronts between modulated patterns have null propagation velocities. A suitable explanation is found by considering reaction-diffusion systems where there are two extremely different diffusivities, the thermal diffusivity κ and the vorticity diffusivity ν . If $\nu \gg \kappa$, then it is theoretically [46, 47] obtained that $v_p \approx \sqrt{\kappa} \approx 0$. 1D-fronts are stationary except for the mixed pattern (for shallow layers) when the alternating pattern (ALT)

spreads inhomogeneously in the form of irregular (spatiotemporal) patches which coexist with the basic cellular pattern (ST).

From the **discrete analysis** in the 1D-array of 75-convective oscillators, which decodes individual phases of each oscillator, we infer that new patterns arise from phase synchronization processes between the convective oscillators. In this discrete analysis we are able to define a new order parameter obtained from the **antiphase matrix** which allows to quantify the dynamics far from the threshold of the ST/ZZ instability. Nevertheless, phase synchronization is not a sufficient condition because a minimal amplitude of the fundamental modes is required to trigger the synchronization instability.

From the discrete analysis we also obtain the *diffusive coupling range* between neighboring oscillators, which is found to reach 4-5 oscillators. Therefore, we show that the coupling is *nonlocal* (further than first neighbors) and that from a **nonlocal coupling** a **global phase synchronization regime** can be achieved because of the diverging correlation times of the entire 1D-array of coupled oscillators.

Spatially extended systems, counter-intuitively may develop **coherent patterns** (the ST/ZZ regime) above **spatiotemporal chaotic regimes** (mixed ST/ALT pattern). These coherent domains in ZZ are robust and bounded by well-defined stationary 1D-fronts, they represent the final stage of a *clustering process*. The continuous growth of the amplitude evolution of the critical modes inside these coherent domains allows us to classify the nature of this instability as **supercritical**. Meanwhile, in the spatiotemporal chaotic regime, the amplitude of the oscillatory modes inside the irregular domains remains constant.

The existence of **localized domains** in the beating regimes (ST/ZZ and ST/DW) approaches, in extended 1D systems of size L_x , the statistical model of spatiotemporal chaos developed by Hohenberg and Shraiman [6]. This theoretical model refers to systems where the scales of energy supply and dissipation are of the same order (in our case of the order of the depth of the fluid layer d), and besides the system size satisfies that $L_x \gg d$. Under these conditions, at $d = 3$ mm our system exhibits two spatiotemporal coherent domains of width $L_c < L_x$. $L_c > \xi$, where ξ has been defined as a correlation length of the system and has been measured as an attenuation length of the new ST/ZZ pattern inside the surrounding pattern ST ($\langle \xi \rangle \approx 30$ mm, so $\xi \ll L_x$). In this context, the domains of width L_c are *correlated surfaces in space and time*.

The **supercritical instability** of the critical modes $M_{\pm z}$ is in agreement with the synchronization phase theory with weak coupling [105] where the order parameter is defined as $\sigma = \frac{1}{N} \sum_{j=1}^N e^{i|\phi_j - \Phi|}$, where Φ is the cluster phase (phase of synchronization) and ϕ_j is the critical phase of each oscillator. This critical phase can be slightly shifted from Φ , it fulfils: $|\phi_j - \Phi| \leq \Delta$. This is the *synchronization condition* dependent on the detuning Δ . In our 1D-cell experiment, the threshold ε_c and maximum detuning of synchronization Δ are given by the explored dynamics whereas in numerical simulations are driven by the selected values of the equation parameters.

Spatiotemporal phase synchronization transitions towards the spatiotemporal beating regime (ST/ZZ) arise from the spatiotemporal splitting of the traveling modes. These transitions enable us to study the dynamics of the 1D-array through out this regime and the subsequent one (ST/DW) where the spatial splitting fades away. Thus, a phase description is suitable even far from the threshold where nonlinear couplings become stronger, meanwhile the amplitudes of the critical modes show a turbulent behavior.

Concerning **coherent phenomena** in experimental extended systems, we should emphasize

the dynamical features which are also shared with other systems in the **route to weak turbulence**: (i) the existence of critical domains with saturated widths (stationary clusters in the ST/ZZ regime of size L_c); (ii) the existence of a cascade of bifurcations towards a spatiotemporal beating regime (ST/ZZ) where the fundamental traveling modes split in both space and time; and (iii) the existence of localized patterns which are strongly nonlinear (ST/DW) characterized by the presence of defects.

Outlook

The perspectives of this work have four main directions: (i) *experimental research* on hydrodynamic instabilities developed in extended systems which are subjected to other different external fields like the magnetic field; (ii) *theoretical widening* of phase synchronization transitions; (iii) *developing numerical simulations* for high-dimensional complex systems; (iv) *applications of developed analytical and theoretical methodologies* for the clustering processes exhibited by the 1D array of 75-convective oscillators into complex 2D and 3D-systems belonging to other disciplines.

Research in **nonlinear waves** like spirals in hydrothermal waves deserves still more experimental effort, as a matter of fact this dynamics is present in many other systems like in 2D-RB convection [102], 2D chemical reaction-diffusion systems [100] and looks for being understood further beyond, for example in scroll rings in 3D, recent works are found experimentally [154] and theoretically [155]. From another point of view, understanding the instability mechanisms in nonlinear waves like “thermal flowers” in the FL pattern might help to understand growth processes in many physical (propagating interfaces in crystal growth) and biological (morphogenesis from bud to bloom) systems.

The **Kuramoto model** and analogous theories try to explain synchronization from global coupling of an ensemble of oscillators with distribution of frequencies without paying attention on the topology dynamics, thus this theoretical approaches might explain $\Phi(T)$ but not $\Phi(X, T)$ from the oscillators phases $\phi_i(x, t)$. In this sense, we carry out the analysis of the link matrix L_{ij} which takes into account the effect of topology (collisions between oscillators) into dynamics. This fact might be considered in theoretical research, in this sense the information obtained from the link matrix might be introduced in models like a time-dependent weighting function.

Nonlocal coupling could explain similar clustering transitions in other systems, for example in biology (from bacteria colonies to the beats of pacemakers cells in the heart), in chemistry (spirals in reaction-diffusion systems), in neurobiology (epileptic activity of neurons) and in physics (coupled arrays of superconductors and semiconductor lasers). Coupling between oscillators may evolve from local [91] to nonlocal [103, 139, 140, 156], or even to global coupling [157], in contrast with earlier theoretical work which was mostly focused on global interactions [108, 158]. Results on phase synchronization phenomena towards a global spatiotemporal synchronized pattern by computing phase mismatches from the cross-correlation matrix, is a new challenge that needs to be included as a suitable analytical tool in the study of clusters. Besides, it enables us to explore weak turbulent regimes finding out the critical modes which might be slightly shifted from the previous existing ones. Regarding a spatially extended array of nonlinearly coupled oscillators, which might suffer damping processes and reactivation of their previous oscillatory state, directed percolation and spatiotemporal intermittency adjust the model of nonlocal cou-

pling between nearby oscillators and involve many natural processes (from hydrodynamics and transport phenomena in porous media to immunological systems [159]).

However, when the same techniques are applied to the **spatiotemporal chaotic regime** (STC), we meet two controversial points that have to be taken into account: (1) the effect of noise because the oscillators do not have definite frequencies; (2) collapsing and fluctuating fronts of cluster domains, synchronized in ϕ^v , provide small spatiotemporal correlations which play against cross-correlation techniques.

The suddenly diverging behavior of the invasion rate might provide an experimental useful clue in order to understand similar dynamics in the so-called “**chimera states**” proposed in 2003 by Tanaka, Shima and Kuramoto [139, 140]. This state arises from nonlocal coupling and could explain many processes which are not already understood neither under the perspective of global nor local coupling. Until the present moment, the closest approach to our 1D-dynamics is the theoretical work developed in 2006 by Abrams and Strogatz [103] for a ring of nonlinear coupled oscillators.

Bibliography

- [1] P. Curie. *J. Phys. Théorique et Appliquée 3^{me} série* **3**, (1894), p. 393.
- [2] H. Bénard. *Les tourbillons cellulaires dans une nappe liquide transportent de la chaleur par convection en regime permanent*. *An. Chim. Phys.* **7 (23)**, (1900), p. 62.
- [3] Y. Pomeau. *Front motion, metastability and subcritical bifurcations in hydrodynamics*. *Physica* **23D**, (1986), pp. 3–11.
- [4] P. Ehrenfest. *Proc. Acad. of Sci. Amsterdam* **36**, (1933), p. 153.
- [5] A. T. Winfree. *Biological rhythms and the behavior of populations of coupled oscillators*. *J. Theoret. Biol.* **16**, (1967), pp. 15–42.
- [6] P. C. Hohenberg, B. I. Shraiman. *Chaotic behavior of an extended system*. *Physica D* **37**, (1989), pp. 109–115.
- [7] S. H. He, H. B. Huang, X. Zhang, Z. X. Liu, D. S. Xu, C. K. Shen. *Chaotic synchronization in large map networks*. *Phys. Rev. E* **74**, (2006), p. 057203.
- [8] J. Gómez-Gardeñes, Y. Moreno, A. Arenas. *Paths to synchronization on complex networks*. *Phys. Rev. Lett.* **98**, (2007), p. 034101.
- [9] A. C. Martí, C. Masoller. *Synchronization of globally coupled non-identical maps with inhomogeneous delayed interactions*. *Physica A* **342**, (2004), pp. 344–350.
- [10] M. A. Miranda, J. Burguete. *Subcritical instabilities in a convective fluid layer under a quasi-one-dimensional heating*. *Phys. Rev. E* **78**, (2008), p. 046305.
- [11] M. A. Miranda, J. Burguete. *Experimentally observed route to spatiotemporal chaos in an extended one-dimensional array of convective oscillators*. *Phys. Rev. E* **79**, (2009), p. 046201.
- [12] M. A. Miranda, J. Burguete. *Spatiotemporal phase synchronization in a large array of convective oscillators*. To be published in *Int. J. Bifurcation and Chaos* .
- [13] H. B. Callen. *Thermodynamics*. Wiley, New York (1960).
- [14] A. LaPorta, K. D. Eaton, C. M. Surko. *Transition between curved and angular textures in binary fluid convection*. *Phys. Rev. E* **53**, (1996), p. 570.
- [15] M. Heutmaker, P. Fraenkel, J. Gollub. *Convection patterns: time evolution of the wave-vector field*. *Phys. Rev. Lett.* **54**, (1985), pp. 1369–1372.

- [16] P. Couillet, G. Iooss. *Instabilities of one-dimensional cellular patterns*. Phys. Rev. Lett. **64**, (1990), p. 866.
- [17] R. E. Goldstein, G. H. Gunaratne, L. Gil, P. Couillet. *Hydrodynamic and interfacial patterns with broken space-time symmetry*. Phys. Rev. A **43**, (1991), pp. 6700–6721.
- [18] L. Gil. *Instabilities of one-dimensional cellular patterns: Far from the secondary threshold*. Europhys. Lett. **48**, (1999), pp. 156–162.
- [19] L. Gil. *Secondary instability of one-dimensional cellular patterns: a gap soliton, black soliton and breather analogy*. Physica D **147**, (2002), pp. 300–310.
- [20] W. Schöpf, L. Kramer. *Small-amplitude periodic and chaotic solutions of the complex Ginzburg-Landau equation for a subcritical bifurcation*. Phys. Rev. Lett. **66**, (1991), pp. 2316–2319.
- [21] R. J. Deissler, H. R. Brand. *Periodic, quasiperiodic and chaotic localized solutions of the quintic complex Ginzburg-Landau equation*. Phys. Rev. Lett. **72**, (1994), pp. 478–481.
- [22] R. J. Deissler, H. R. Brand. *Effect of nonlinear gradient terms on breathing localized solutions in the quintic complex Ginzburg-Landau equation*. Phys. Rev. Lett. **81**, (1998), pp. 3856–3859.
- [23] C. Misbah, A. Valance. *Secondary instabilities in the stabilized Kuramoto-Sivashinsky equation*. Phys. Rev. E **49**, (1994), pp. 166–183.
- [24] P. Brunet. *Stabilized Kuramoto-Sivashinsky equation: A useful model for secondary instabilities and related dynamics of experimental one-dimensional cellular flows*. Phys. Rev. E **76**, (2007), p. 017204.
- [25] L. Landau, E. Lifchitz. *Física estadística tomo 5*. Reverté (1969).
- [26] K. Huang. *Statistical mechanics*. John Wiley & Sons, New York, 2nd edn. (1987).
- [27] D. I. Uzunov. *Theory of critical phenomena*. World Scientific (1993).
- [28] N. Garnier. *Ondes non-linéaires à une et deux dimensions dans une mince couche de fluide*. Ph.D. thesis, CEA, Saclay (2000).
- [29] J. Burguete, N. Mukolobwicz, F. Daviaud, N. Garnier, A. Chiffaudel. *Bouyant-thermocapillary instabilities in extended liquid layers subjected to a horizontal temperature gradient*. Phys. Fluids **13**, (2001), pp. 2773–2787.
- [30] A. Yethiraj, J. Bechhoefer. *Two experimental tests of the Halperin-Lubensky-Ma effect at the nematic-smectic-A phase transition*. Phys. Rev. Lett. **84**, (2000), pp. 3642–3645.
- [31] P. Bot, O. Cadot, I. Mutabazi. *Secondary instability mode of a roll pattern and transition to spatiotemporal chaos in the Taylor-Dean system*. Phys. Rev. E **58**, (1998), pp. 3089–3097.
- [32] A. L. Porta, C. Surko. *Phase defects as a measure of disorder in traveling-wave convection*. Phys. Rev. Lett. **77**, (1996), p. 5916.

- [33] A. L. Porta, C. Surko. *Reflection of nonlinear waves from a domain boundary*. Phys. Rev. Lett. **77**, (1996), pp. 2678–2681.
- [34] A. Kudrolli, J. P. Gollub. *Localized spatiotemporal chaos in surface waves*. Phys. Rev. E **54**, (1996), p. R1052.
- [35] M. G. Clerc, T. Nagaya, A. Petrossian, S. Residori, C. S. Riera. *First-order Fréedericksz transition and front propagation in a liquid crystal light valve with feedback*. Eur.Phys.J. D **28**, (2004), pp. 435–445.
- [36] V. V. Barelko, I. I. Kurochka, A. G. Merzhanov, K. G. Shkadinskii. *Investigation of traveling waves on catalytic wires*. Chem. Eng. Sci. **33**, (1978), pp. 805–811.
- [37] D. Bensimon, B. I. Shraiman, V. Croquette. *Nonadiabatic effects in convection*. Phys. Rev. A **38**, (1988), pp. 5461–5464.
- [38] L. Landau, E. Lifchitz. *Fluid Mechanics*. Pergamon Press (1987).
- [39] R. Fisher. *The wave of advance of advantageous genes*. Ann. Eugenics **7**, (1937), pp. 335–369.
- [40] M. G. Clerc, S. Residori, C. S. Riera. *First-order Fréedericksz transition in the presence of light-driven feedback in nematic liquid crystals*. Phys. Rev. E **63**, (2001), pp. 060701–1. Rapid communications.
- [41] M. G. Clerc, C. Falcón, E. Tirapegui. *Front propagation sustained by additive noise*. Phys. Rev. E **74**, (2006), p. 011303(15).
- [42] M. G. Clerc, D. Escaff, R. Rojas. *Depinning dynamics of interface connecting stripe pattern and uniform state*. nlin/0610027 v1 .
- [43] S. Residori, A. Petrossian, T. Nagaya, C. S. Riera, M. G. Clerc. *Fronts and localized structures in liquid-crystal-light-valve with optical feedback*. Physica D **199**, (2004), pp. 149–165.
- [44] G. Küppers, D. Lorz. *Transition from laminar convection to thermal turbulence in a rotating fluid layer*. J. Fluid Mechanics **35**, (1969), p. 609.
- [45] B. A. Malomed, A. A. Nepomnyashchy, M. I. Tribelsky. *Domain boundaries in convection patterns*. Phys. Review A **42**, (1990), pp. 7244–7263.
- [46] L. Kramer, G. Gottwald, V. I. Krinsky, A. P. et al. *Persistence of zero velocity fronts in reaction diffusion systems*. Chaos **10**, (2000), pp. 731–737.
- [47] J. A. Sepulchre, V. I. Krinsky. *Bistable reaction-diffusion systems can have robust zero-velocity fronts*. Chaos **10**(4), (2000), pp. 826–833.
- [48] M. C. Cross, P. C. Hohenberg. *Pattern formation outside of equilibrium*. Reviews of Modern Physics **65**, (1993), pp. 851–1112.
- [49] W. van Saarloos. *Front propagation into unstable states*. Phys. Rep. **386**, (2003), pp. 29–222.

- [50] F. Daviaud, J. Lega, P. Bergé, P. Couillet, M. Dubois. *Spatio-temporal intermittency in a 1D convective pattern*. Physica D **55**, (1992), pp. 287–308.
- [51] S. Bottin, F. Daviaud, P. Manneville, O. Dauchot. *Discontinuous transition to spatiotemporal intermittency in plane Couette flow*. Europhys. Lett. **43**, (1998), pp. 171–176.
- [52] D. Coles. *In Mécanique de la Turbulence*. CNRS Paris (1962).
- [53] E. Buckingham. *The principle of similitude*. Nature **96**, (1915), pp. 396–397.
- [54] S. Succi, I. V. Karlin, H. Chen. *Colloquium: Role of the H theorem in lattice Boltzmann hydrodynamic simulations*. Rev. of Modern Physics **74**, (2002), pp. 1203–1220.
- [55] D. Schwabe, F. Preisser, A. Scharmann. *Instabile Marangonikonvektion unter mikrogravitation*. Z. Flugwiss. Weltraumforsch **6**, (1982), p. 309.
- [56] D. Schwabe. *Hydrodynamic instabilities under microgravity in a differentially heated long liquid bridge with aspect ratio near the Rayleigh-limit: experimental results*. Advances in space research **36**, (2005), pp. 36–42.
- [57] D. Schwabe. *Convective instabilities in complex systems with partly free surface*. J. Phys.: conf. ser. **64**, (2007), p. 012001.
- [58] M. K. Smith, S. H. Davis. *Instabilities of dynamic thermocapillary liquid layers. Part 1. Convective instabilities*. J. Fluid Mech. **132**, (1983), pp. 119–162.
- [59] J. J. Xu, S. H. Davis. *Convective thermocapillary instabilities in liquid bridges*. Phys. Fluids **27**, (1983), pp. 1102–1107.
- [60] M. K. Smith. *Instability mechanisms in dynamic thermocapillary liquid layers*. Phys. Fluids **29(10)**, (1986), pp. 3182–3186.
- [61] N. Mukolobwicz, F. Daviaud, A. Chiffaudel. *Supercritical Eckhaus instability for surface-tension-driven hydrothermal waves*. Phys. Rev. Lett. **80**, (1998), pp. 4661–4664.
- [62] N. Garnier, A. Chiffaudel. *Nonlinear transition to global mode for traveling-wave instability in a finite box*. Phys. Rev. Lett. **86**, (2001), pp. 75–78.
- [63] N. Garnier, A. Chiffaudel. *Two dimensional hydrothermal waves in an extended cylindrical vessel*. Eur. Phys. J. B **19**, (2001), pp. 87–95.
- [64] M. A. Pelacho, A. Garcimartín, J. Burguete. *Local Marangoni number at the onset of hydrothermal waves*. Phys. Rev. E **62**, (2000), pp. 477–483.
- [65] J. Priede, G. Gerbeth. *Convective, absolute, and global instabilities of thermocapillary-bouyancy convection in extended layers*. Phys. Rev. E **56**, (1997), pp. 4187–4199.
- [66] S. H. Davis. *Thermocapillary instabilities*. Ann. Rev. Fluid Mech. **19**, (1987), pp. 403–435.
- [67] L. Pan, J. R. deBruyn. *Spatially uniform traveling cellular patterns at a driven interface*. Phys. Rev. E **49**, (1994), pp. 483–493.

- [68] F. Giorgiutti, A. Bleton, L. Limat, J. E. Wesfreid. *Dynamics of a one-dimensional array of liquid columns*. Phys. Rev. Lett. **74**, (1995), p. 538.
- [69] P. Brunet, J.-M. Flesselles, L. Limat. *Parity breaking in a one-dimensional pattern: A quantitative study with controlled wavelength*. Europhys. Lett. **56(2)**, (2001), pp. 221–227.
- [70] P. Brunet, L. Limat. *Defects and spatiotemporal disorder in a pattern of falling liquid columns*. Phys. Rev. E **70**, (2004), p. 046207.
- [71] C. Counillon, L. Daudet, T. Podgorski, L. Limat. *Dynamics of a liquid column array under periodic boundary conditions*. Phys. Rev. Lett. **80**, (1998), p. 2117.
- [72] A. J. Simon, J. Bechhoefer, A. Libchaber. *Solitary modes and the Eckhaus instability in directional solidification*. Phys. Rev. Lett. **61**, (1988), p. 2574.
- [73] L. Bellon, L. Fourtune, V. T. Minassian, M. Rabaud. *Wave-number selection and parity-breaking bifurcation in directional viscous fingering*. Phys. Rev. E **58**, (1998), p. 565.
- [74] L. Pastur, M. Henriot, R. Ribotta. *Transition to spatiotemporal chaos in the fronts dynamics of a subcritical state*. Phys. Rev. Lett. **86**, (2001), pp. 228–231.
- [75] A. Joets, R. Ribotta. *Localisation and defects in propagative ordered structures*. J. Phys. Colloques (France) **50**, (1989), pp. 171–180.
- [76] J. Burguete, H. Chaté, F. Daviaud, N. Mukolobwicz. *Bekki-Nozaki amplitude holes in hydrothermal nonlinear waves*. Phys. Rev. Lett. **82**, (1999), pp. 3252–3255.
- [77] N. Garnier, A. Chiffaudel, F. Daviaud. *Nonlinear dynamics of waves and modulated waves in 1D thermocapillary flows. ii. Convective/absolute transitions*. Physica D **174**, (2003), pp. 30–55.
- [78] M. A. Pelacho, J. Burguete. *Temperature oscillations of hydrothermal waves in thermocapillary-buoyancy*. Phys. Rev. E **59**, (1999), pp. 835–840.
- [79] J. Burguete, D. Maza, H. L. Mancini. *One-dimensional dynamics in locally heated liquid layers*. Physica D **174**, (2003), pp. 56–70.
- [80] J. Burguete, H. L. Mancini, C. Pérez-García. *Dynamics of a secondary instability in Bénard-Marangoni convection with unidimensional heating*. Europhys. Lett. **23**, (1993), pp. 401–407.
- [81] D. Maza, J. Burguete, H. L. Mancini. *Experimental results on defects in one-dimensional heating patterns*. Int. J. Bifurcation and Chaos **4(5)**, (1994), pp. 1353–1356.
- [82] R. Álvarez, M. van Hecke, W. van Saarloos. *Sources and sinks separating domains of left- and right-traveling waves: Experiment versus amplitude equations*. Phys. Rev. E **56**, (1997), p. R1306.
- [83] E. Ringuet, C. Rozé, G. Gouesbet. *Experimental observation of type-II intermittency in a hydrodynamic system*. Phys. Rev. E **47**, (1993), p. 1405.

- [84] E. Ringuet, S. Meunier-Guttin-Cluzel, C. Rozé, G. Gouesbet. *Experimental study of nonlinear coupling between two oscillators in one-dimensional Marangoni convection*. Int. Comm. Heat Mass Transfer **26**, (1999), pp. 477–486.
- [85] G. Gouesbet, C. Rozé, S. Meunier-Guttin-Cluzel. *Instabilities by local heating below an interface*. J. Non-Equilib. Thermodyn. **25** (3/4), (2000), pp. 337–379.
- [86] L. Pastur, M. T. Westra, D. Snouck, W. van de Water, M. van Hecke et al. *Sources and holes in a one-dimensional traveling wave convection experiment*. Phys. Rev. E **67**, (2003), p. 036305.
- [87] S. Rajesh, S. Sinha, S. Sinha. *Synchronization in coupled cells with activator-inhibitor pathways*. Phys. Rev. E **75**, (2007), p. 011906.
- [88] K. J. Lee, R. E. Goldstein, E. C. Cox. *Resetting wave forms in dictyostelium territories*. Phys. Rev. Lett. **87**, (2001), p. 068101.
- [89] V. K. Vanag, L. Yang, M. Dolnik, A. M. Zhabotinsky, I. R. Epstein. *Oscillatory cluster patterns in a homogeneous chemical system with global feedback*. Nature **406**, (2000), pp. 389–391.
- [90] H. Fukuda, H. Morimura, S. Kai. *Global synchronization in two-dimensional lattices of discrete Belusov-Zhabotinsky oscillators*. Physica D **205**, (2005), pp. 80–86.
- [91] M. Falcke, H. Engel. *Cluster formation, standing waves, and stripe patterns in oscillatory active media with local and global coupling*. Phys. Rev. E **52**, (1995), pp. 763–771.
- [92] G. Kozyreff, A. G. Vladimirov, P. Mandel. *Global coupling with time delay in an array of semiconductor lasers*. Phys. Rev. Lett. **85**, (2000), pp. 3809–3812.
- [93] L. Fabiny, K. Wiesenfeld. *Clustering behaviour of oscillator arrays*. Phys. Rev. A **43**, (1991), pp. 2640–2648.
- [94] S. Viatchenko-Karpinski, B. K. Fleischmann, Q. Liu, H. Sauer, O. Gryshchenko, G. J. Ji, J. Hescheler. *Intracellular Ca²⁺ oscillations drive spontaneous contractions in cardiomyocytes during early development*. Proc. Natl. Acad. Sci. USA **96**, (1999), pp. 8259–8264.
- [95] M. P. K. Jampa, A. R. Sonaware, P. M. Gade, S. Sinha. *Synchronization in a network of model neurons*. Phys. Rev. E **75**, (2007), p. 026215.
- [96] B. Blasius, A. Huppert, L. Stone. *Complex dynamis and phase synchronization in spatially extended ecological systems*. Nature **399**, (1999), p. 354.
- [97] D. J. Earn, S. A. Levin. *Global asymptotic coherence in discrete dynamical systems*. PNAS **103**, (2006), pp. 3968–3971.
- [98] S. Chandrasekhar. *Hydrodynamic and hydromagnetic stability*. Dover (1981).
- [99] A. de la Torre, J. Burguete. *Slow dynamics in a turbulent von Kármán swirling flow*. Phys. Rev. Lett. **99**, (2007), p. 054101.

- [100] V. K. Vanag, I. R. Epstein. *Inwardly rotating spiral waves in a reaction-diffusion system*. Science **294**, (2001), pp. 835–837.
- [101] I. Z. Kiss, Y. Zhai, J. L. Hudson. *Emerging coherence in a population of chemical oscillators*. Science **296**, (2002), p. 1676.
- [102] B. B. Plapp, D. A. Egolf, E. Bodenschatz, W. Pesch. *Dynamics and selection of giant spirals in Rayleigh-Bénard convection*. Phys. Rev. Lett. **81**, (1998), p. 5334.
- [103] D. M. Abrams, S. H. Strogatz. *Chimera states in a ring of nonlocally coupled oscillators*. Int. J. Bifurcation and Chaos **16(1)**, (2006), pp. 21–37.
- [104] S. Rajesh, S. Sinha. *Measuring collective behavior of multicellular ensembles: role of space-time scales*. J. Biosci **33(2)**, (2008), pp. 289–301.
- [105] Y. Kuramoto. *Chemical oscillations, waves and turbulence*. Dover (2003).
- [106] G. V. Osipov, M. M. Sushchik. *Synchronized clusters and multistability in arrays of oscillators with different natural frequencies*. Phys. Rev. E **58(6)**, (1998), pp. 7198–7207.
- [107] G. V. Osipov, J. Kurths, C. Zhou. *Synchronization in oscillatory networks*. Springer-Verlag, Berlin (2007).
- [108] D. Golomb, D. Hansel, B. Shraiman, H. Sompolinsky. *Clustering in globally coupled phase oscillators*. Phys. Rev. A **45**, (1992), pp. 3516–3530.
- [109] M. Timme. *Does dynamics reflect topology in directed networks*. Europhys. Lett. **76(3)**, (2006), pp. 367–373.
- [110] M. Timme. *Revealing network connectivity from response dynamics*. Phys. Rev. Lett. **98**, (2007), p. 224101.
- [111] J. Burguete. *Inestabilidades convectivas producidas por un calentamiento localizado*. Ph.D. thesis, Universidad de Navarra, Pamplona (1995).
- [112] P. Kolodner, H. Williams. *Nonlinear Evolution of Spatio-Temporal Structures in Dissipative Continuous Systems*. Plenum Press, New York (1990).
- [113] G. Bruhat. *Optique*. Masson, 6th edn. (1965).
- [114] G. Ahlers, D. Cannell, V. Steinberg. *Time dependence of flow patterns near the convective threshold in a cylindrical container*. Phys. Rev. Lett. **54**, (1985), p. 1373.
- [115] P. Kolodner, R. Walden, A. Passner, C. Surko. *Rayleigh-Bénard convection in an intermediate-aspect-ratio rectangular container*. J. Fluid Mech. **163**, (1986), pp. 195–226.
- [116] A. Joets, R. Ribotta. *Hydrodynamic transitions to chaos in the convection of an anisotropic fluid*. J. Phys. **47**, (1986), pp. 595–606.
- [117] A. Joets, R. Ribotta. *Caustics and symmetries in optical imaging. The example of convective flow visualization*. J. Phys. I France **4**, (1994), pp. 1013–1026.
- [118] R. Hamming. *Digital filters*. Dover Publications, 3rd edn. (1998).

- [119] A. V. Oppenheim, R. W. Schaffer. *Discrete-time signal processing*. Prentice Hall, New Jersey (1999).
- [120] Y. Tu, M. C. Cross. *Chaotic domain structure in rotating convection*. Phys. Rev. Lett. **69**, (1992), pp. 2515–2518.
- [121] S. Bottin. *Structures cohérentes et transition vers la turbulence par intermittence spatio-temporelle dans l'écoulement de Couette plan*. Ph.D. thesis, Université de Paris XI, Orsay (1998).
- [122] B. Marts, K. Martinez, A. L. Lin. *Front dynamics in an oscillatory bistable Belousov-Zhabotinsky chemical reaction*. Phys. Rev. E **70**, (2004), p. 056223.
- [123] R. Ribotta. *Critical behavior of the penetration length of a vortex into a subcritical region*. Phys. Rev. Lett. **42**, (1979), p. 1212.
- [124] R. Krishnamurti. *On the transition to turbulent convection. Part 1. The transition from two- to three-dimensional flow*. J. Fluid Mech. **42**, (1970), pp. 295–307.
- [125] L. Brillouin. *Wave propagation in periodic structures: electric filters and crystal lattices*. McGraw-Hill, New York, 1st ed., 2nd imp. edn. (1946).
- [126] J. E. Sipe, H. G. Winful. *Nonlinear Schrödinger solitons in a periodic structure*. Optic Lett. **13**, (1988), pp. 132–133.
- [127] S. M. Tobias, M. R. E. Proctor, E. Knobloch. *Convective and absolute instabilities of fluid flows in finite geometry*. Physica D **113**, (1998), pp. 43–72.
- [128] P. Kolodner. *Observations of the Eckhaus instability in one-dimensional traveling-wave convection*. Phys. Rev. A **46**, (1992), p. 1739.
- [129] S. Mao, J. de Bruyn, Z. Daya, S. Morris. *Boundary-induced wave number selection in a 1D pattern-forming system*. Phys. Rev. E **54**, (1996), p. R1048.
- [130] A. M. Mancho, H. Herrero, J. Burguete. *Primary instabilities in convective cells due to nonuniform heating*. Phys. Rev. E **56**, (1997), pp. 2916–2923.
- [131] K. Kaneko, I. Tsuda. *Complex systems: chaos and beyond*. Springer (2000).
- [132] H. Chaté, P. Manneville. *Structure of clusters generated by spatio-temporal intermittency and directed percolation in two space dimensions*. Phys. Rev. A **38**, (1988), pp. 4351 – 4354.
- [133] T. M. Janaki, S. Sinha, N. Gupte. *Evidence for directed percolation universality at the onset of spatiotemporal intermittency in coupled circle maps*. Phys. Rev. E **67**, (2003), p. 056218.
- [134] D. L. Mills, S. E. Trullinger. *Gap solitons in nonlinear periodic structures*. Phys. Rev. B **36**, (1987), pp. 947–952.
- [135] J. Lega. *Defauts topologiques associés a la brisure de l'invariance de translation dans le temps*. Ph.D. thesis, Université de Nice (1989).

- [136] P. Coulet, R. E. Goldstein, G. H. Gunaratne. *Parity-breaking transitions of modulated patterns in hydrodynamics systems*. Phys. Rev. Lett. **63**, (1989), pp. 1954–1957.
- [137] H. Daido, K. Nakanishi. *Aging and clustering in globally coupled oscillators*. Phys. Rev. E **75**, (2007), p. 056206.
- [138] D. M. Abrams, S. H. Strogatz. *Chimera states for coupled oscillators*. Phys. Rev. Lett. **93**, (2004), p. 174102.
- [139] D. Tanaka, Y. Kuramoto. *Complex Ginzburg-Landau equation with nonlocal coupling*. Phys. Rev. E **68**, (2003), p. 026219.
- [140] S. Shima, Y. Kuramoto. *Rotating spiral wave with phase-randomized core in nonlocally coupled oscillators*. Phys. Rev. E **69**, (2004), p. 036213.
- [141] Y. Kuramoto. *Proc. Int. Symp. on mathematical problems in theoretical physics*, vol. 30. Springer, New York (1975).
- [142] R. Krishnamurti. *On the transition to turbulent convection. Part 2. The transition to time-dependent flow*. J. Fluid Mech. **42**, (1970), pp. 309–320.
- [143] S. Wakitani. *Experiments on instabilities of thermocapillary convection in shallow annular liquid layers*. Journal of Physics: Conference Series **64**, (2007), p. 012006.
- [144] W. Shi, N. Imaishi. *Hydrothermal waves in differentially heated shallow annular pools of silicone oil*. Journal of crystal growth **290**, (2006), pp. 280–291.
- [145] W. Shi, M. K. Ermakov, N. Imaishi. *Effect of pool rotation on thermocapillary convection in shallow annular pool of silicone oil*. Journal of crystal growth **294**, (2006), pp. 174–485.
- [146] Y. R. Li, L. Peng, S. Y. Wu, N. Imaishi, D. L. Zeng. *Thermocapillary-bouyancy flow of silicon melt in a shallow annular pool*. Cryst. Res. Technol. **39**, (2004), pp. 1055–1062.
- [147] E. Favre, L. Blumenfeld, F. Daviaud. *Instabilities of a liquid layer locally heated on its free surface*. Phys. Fluids **9(5)**, (1997), p. 1473.
- [148] S. Hoyas, A. M. Mancho, H. Herrero, N. Garnier, A. Chiffaudel. *Bénard-Marangoni convection in a differentially heated cylindrical cavity*. Phys. Fluids **17**, (2005), p. 054104.
- [149] N. Garnier, C. Normand. *Effects of curvature on hydrothermal waves instability of radial thermocapillary flows*. Comptes-rendus de l'Académie des Sciences **20012(8)**, (2001), pp. 1227–1233.
- [150] B. Echebarria. *Inestabilidades termocapilares en una capa de fluido*. Ph.D. thesis, Universidad de Navarra, Pamplona (1998).
- [151] E. L. Koschmieder. *Bénard convection*. Adv. Chem. Phys. **26**, (1974), pp. 177–212.
- [152] F. T. Arecchi, S. Boccaletti, S. Ducci, E. Pampaloni, P. L. Ramazza, S. Residori. *The liquid crystal light valve with optical feedback: a case study in pattern formation*. J. Nonlin. Opt. Phys. & Materials (JNOPM) **9**, (2000), pp. 183–204.

- [153] T. Nagaya, T. Yamamoto, T. Asahara, S. Nara, S. Residori. *Nonlinear dynamics of the petal-like patterns in a liquid crystal valve with rotational optical feedback*. J. Opt. Soc. Am. B **25**, (2008), pp. 74–82.
- [154] T. Bánsági, O. Steinbock. *Three-dimensional spiral waves in an excitable reaction system: initiation and dynamics of scroll rings and scroll ring pairs*. Chaos **18**, (2008), pp. 026102–1,8.
- [155] B. Echebarria, V. Hakim, H. Henry. *Non-equilibrium ribbon model of scroll waves with twist*. Phys. Rev. Lett. **96**, (2006), p. 9831.
- [156] H. Nakao. *Anomalous spatio-temporal chaos in a two-dimensional system of non-locally coupled oscillators*. Chaos **9(4)**, (1999), pp. 902–909.
- [157] C. Zhou, J. Kurths. *Dynamical weights and enhanced synchronization in adaptive complex networks*. Phys. Rev. Lett. **96**, (2006), p. 164102.
- [158] H. Daido. *Onset of cooperative entrainment in limit-cycle oscillators with uniform all-to-all interactions: bifurcation of the order function*. Physica D **91**, (1996), pp. 24–66.
- [159] M. Sashimi. *Applications of percolation theory*. Taylor & Francis (1994).

Summary

This experimental work contributes to widen the understanding of the dynamics of spatially extended and dissipative systems. By means of two different convective systems (1D and 2D) we explore the dynamics by modifying localized temperature gradients and characterize quantitatively the nature of the instabilities the systems go through. The 1D-system is a rectangular fluid layer opened to the atmosphere and subjected to a quasi-1D heating from below and along a central line in the largest direction. The 2D-system is a cylindrical fluid layer subjected to a radial temperature gradient between an inner core and the external rim. In both systems, instabilities depend on the depth of the fluid layer and are driven by vertical temperature gradients in the 1D-system and by radial and vertical temperature gradients in the 2D-system. From the primary instability, these systems undergo a cascade of secondary bifurcations towards turbulent or disordered regimes. Instabilities from the homogeneous pattern (with continuous translation symmetry in the direction parallel to the heating line) are found to be supercritical in both systems. The 1D-system, from a stationary cellular pattern (ST) with wave number q , bifurcates subcritically towards a mixed pattern where irregular time-dependent clusters (ALT), with a doubled wave length $q/2$, coexist with ST; and towards traveling waves (TW) with $2q/3$. We particularly focus on the spatiotemporal beating regime (ST/ZZ) characterized by the presence of stationary clusters which emerge from a spatiotemporal splitting of the critical modes. Close to the threshold, a global analysis of the convective field allows us to discover the supercritical nature of this instability. Far from the threshold, a discrete analysis over 50 convective oscillators shows that a global phase synchronization transition has been produced from a nonlocal coupling.

Resumen

Este trabajo experimental contribuye a ampliar el conocimiento de la dinámica de sistemas espacialmente extensos y disipativos. Mediante dos sistemas convectivos diferentes (1D y 2D) exploramos la dinámica modificando gradientes de temperatura localizados y caracterizamos cuantitativamente la naturaleza de las bifurcaciones que el sistema atraviesa. El sistema 1D es una capa de fluido rectangular abierta a la atmósfera y sometida por debajo a un calentamiento cuasi unidimensional a lo largo de una línea central en la mayor dirección. El sistema 2D es una capa de fluido cilíndrica sometida a un gradiente de temperaturas radial entre el núcleo central y el anillo exterior. En ambos experimentos, las inestabilidades dependen del espesor de la capa de fluido y están gobernadas por el gradiente de temperaturas vertical en el sistema 1D y por los gradientes de temperaturas radial y vertical en el sistema 2D. Desde la inestabilidad primaria, estos sistemas sufren una cascada de bifurcaciones secundarias hacia regímenes turbulentos o desordenados. Las inestabilidades desde un patrón homogéneo (con simetría continua de traslación en la dirección paralela a la línea de calentamiento) han resultado ser supercríticas, en ambos sistemas. El sistema 1D, desde un patrón celular estacionario (ST) con número de onda q , bifurca subcríticamente hacia un patrón mixto donde clusters irregulares dependientes del tiempo (ALT), con una longitud de onda doble $2q$, coexisten con ST; y hacia ondas viajeras (TW) con $2q/3$. Nos centramos particularmente en el régimen de batidos espacio-temporales (ST/ZZ) caracterizado por la presencia de clusters estacionarios que aparecen por un desdoblamiento espacio-temporal de los modos críticos. Cerca del umbral, un análisis global del campo convectivo nos permite descubrir la naturaleza supercrítica de esta inestabilidad. Lejos del umbral, un análisis discreto sobre 50 osciladores convectivos demuestra que se ha producido una transición global de sincronización de fase desde un acople no local.

